國立交通大學

光電工程研究所

博 士 論 文

具超薄氧化層之記憶體與光伏元件

Memory And Photovoltaic Devices

With Ultrathin Oxide Layers

研 究 生：張 資 岳

指導教授：李 柏 璁 博士

中 華 民 國 九 十 九 年 十 月

具超薄氧化層之記憶體與光伏元件

Memory And Photovoltaic Devices With Ultrathin Oxide Layers

研 究 生：張資岳　　Student : Tzu-Yueh Chang

指導教授：李柏璁 博士　　Advisor : Dr. Po-Tsung Lee

國 立 交 通 大 學

光 電 工 程 研 究 所

博 士 論 文

A Dissertation

Submitted to Institute of Electro-Optical Engineering

College of Electrical Engineering

National Chiao Tung University

in partial Fulfillment of the Requirements

for the Degree of

Doctor of Philosophy

in

Electro-Optical Engineering

October 2010

Hsinchu, Taiwan, Republic of China

中 華 民 國 九 十 九 年 十 月

具超薄氧化層之記憶體與光伏元件

學　　生：張 資 岳

指導教授：李 柏 璁 博士

國立交通大學光電工程研究所 博士班

摘　要

在這本篇論文中，我們研究三個具超薄氧化層綠色電子元件，即兩個有機雙穩態元件與一個金氧半太陽能電池。超薄氧化層除了可以幫助實現有機雙穩態的電阻態切換與了解相對應的切換機制之外，也可以降低金半太陽能電池的逆向飽和電流而提升元件的開路電壓。

首先，我們研究具 n-type Si/Alq_3/Al 結構的有機雙穩態元件特性。該元件的雙穩態特性是主要來自 Alq_3/Al 界面的缺陷態。值得一提的是我們可以藉由調控 Alq_3 薄膜沉積鍍率去調整該元件的電性。為了瞭解這些現象，我們利用高解析電子能譜儀分析 Alq_3 薄膜與 Alq_3/Al 介面的化學組成，以及透過原子力顯微鏡與薄膜低掠角繞射解析 Alq_3 薄膜與 Alq_3/Al 介面的特性。

然後，我們研究另一種結構的有機雙穩態元件(p^+-Si/Alq_3/nanostructured MoO_x/Alq_3/Al)特性。該元件的雙穩態特性是來自嵌入於 Alq_3 薄膜內的 MoO_x 似奈米團簇對載子捕抓與釋放之現象。當 MoO_x 似奈米團簇捕抓載子後(高導電態)，所形成的空間

電荷會主導元件內載子的傳輸機制。我們也探討該元件的雙穩態滯留時間與寫入-讀取-抹除-讀取之特性。

最後，我們提出一個有效提升開路電壓的疊合式金氧半太陽能電池結構，而該疊合式金氧半太陽能電池是由一個 n 型金氧半太陽能電池與一個 p 型金氧半太陽能電池所構成。在 AM1.5 模擬太陽光照射下，該太陽能電池的開路電壓可達 0.71V。該開路電壓高於目前已發表的 n 型或 p 型金氧半太陽能電池之開路電壓。在此，我們成功地證明利用疊合式金氧半太陽能電池結構提升太陽能電池的開路電壓之可行性。該疊合式金氧半太陽能電池結構將在未來光伏元件應用於水裂解氫能中扮演重要的角色。

Memory And Photovoltaic Devices With Ultrathin Oxide Layers

Student: Tzu-Yueh Chang

Advisor: Dr. Po-Tsung Lee

Department of Photonics and Institute of Electro-Optical Engineering
National Chiao Tung University

Abstract

In this dissertation, we study three green devices using ultrathin oxide layers: two organic bistable devices (OBDs) and one metal-insulator-semiconductor (MIS) solar cell. The ultrathin oxide layers not only can help realize the resistance switching of the OBDs and recognize the corresponding mechanisms, but also can reduce the reversed saturation current of metal-semiconductor solar cells and thus can ameliorate the open-circuit voltage (V_{oc}) of the solar cells.

First of all, the properties of an OBD using an n-type Si/Alq_3/Al structure are investigated. The bistable effect of the OBD is primarily caused by the interface defects at the Alq_3/Al interface. It is worthy to mention that the electrical properties of the OBD can be modified and controlled by utilizing the appropriate deposition rate of the Alq_3 thin film. To

understand these phenomena, we use high resolution X-ray photoelectron spectroscopy to analyze the chemical composition of the Alq_3/Al interface and Alq_3 thin films, and atomic force microscopy and grazing incident X-ray diffraction to characterize the properties of Alq_3 thin films.

Furthermore, the electrical properties of an OBD with a p^+-Si/Alq_3/nanostructured MoO_x/Alq_3/Al structure are also investigated. The bistable switching of the OBD attributes to the charge trapping/erasing in the MoO_x nanoclusterlike layer interposed between the Alq_3 thin films. After charges are trapped in the MoO_x nanoclusterlike layer (the high conductance state), the carrier transportation of the OBD will be dominated by a space-charge field which results from trapped charges. Both the retention measurement and write-read-erase-read cycles of the OBD are also provided.

Finally, a stacking MIS solar cell structure, which integrates an n-type MIS solar cell with a p-type MIS one, is proposed to effectively enlarge V_{oc}. The measured V_{oc} is up to 0.71V under simulated air mass (AM) 1.5 illumination (100 mW/cm^2). This V_{oc} is larger than those of the n-type or p-type MIS solar cells published. Here we successfully demonstrate the feasibility of the V_{oc} enhancement of MIS solar cells by using a stacking structure. The stacking MIS solar cell will play an important role in photovoltaic application for hydrogen generation.

Acknowledgement

一路走來，有歡笑、淚水與辛酸，但不論我悲歡喜樂，父母親總是在身旁鼓勵著我，使我不斷地向前邁進，如今我完成博士學業，最想跟我的父母親說:「爸、媽辛苦了!感謝你們!」。

從碩士班一直到博士班，我皆在李柏璁教授實驗室做研究，李柏璁教授提供我多面向的研究發展，也開啟我對於研究的思維，還有傳授寶貴的經驗，這些皆對於我的研究有著莫大的助益；在我研究遇到瓶頸時，李柏璁教授總是盡全力地協助我，因而今天才有這本論文的呈現，在此，感謝李柏璁教授多年來的指導與教誨，學生永遠銘記在心。此外，還要感謝許多在我人生與學業上給予協助的老師們，因為有您們，我才能夠成長更快、更茁壯。

在這幾年中，實驗室每年除了訓練有素的研究生畢業也有新的成員加入，因此結認識許多學長、同學與學弟妹。感謝與我一起奮鬥的學弟妹們：思元、明璽、欣育、怡先、光揚、又瑋、鈞隆、宜恒、書維、文齡與品睿等，能與你們一起打拼是我的榮幸，而實驗室的其他成員：贊文、士強、吉東、紘鈞、國輝、鴻祺、書志、峻豪、豐懋、明峯、俊德、佳禾、嘉銘、仲銓、孟穎、宜育、均融、和璁、韋德、逸華、青樺、佳揚、品佐、君源、雋威、立勛、紹平等，雖然我們研究主題差很多，但是我從你們身上學到很多寶貴的經驗，謝謝你們。

在我求學過程中，家裡姐姐們常常給予我適時的幫助與鼓勵，有妳們的關懷，我才能更放心的在交大求學，感謝妳們。最後，感謝我可愛的女朋友:亭均，妳在這漫長的時間裡，陪伴著我度過每一天，當我感到心情低落與迷網時，妳總是試圖讓我展開笑顏與回復信心，有妳真好。

讀博士班雖然辛苦，但這是一種磨練，而當我遇見困難時，承蒙許多人的幫忙與照顧，我才能順利走完攻讀博士之路；古人云:「施比受更有福!」，希望未來我是最有福的人。

2010/10/27 于 新竹 國立交通大學 交映樓401室

Table of Contents

Figure Captions

Chapter 1

Chapter 2

Chapter 3

Chapter 4

Chapter 5

Table Captions

Chapter 2

Chapter 5

Chapter 1

Introduction

1.1 Green Technology

Green technology has been largely developed recently for tackling environment and energy issues (such as the green house effect [1], [2]) which we are suffering. Green technology is the technology which uses less energy and generates less pollution. For example, we can modify our fabrication processes to be the clean, low-pollutant, and low-power ones (the environment-friendly processes).

Organic electronics (such as organic memory, and organic light emitting diodes) is one of main streams of green technology because of low temperature fabrication, low fabrication cost, light weight, and high mechanical flexibility. Due to growing demand in nonvolatile, rewritable memory of information technology in our daily life, organic resistive memory (ORM) has been paid much attention. It not only greatly reduces the fabrication processes and cost of conventional memory, but also is promising to solve the bottleneck of the scaling technology of the conventional semiconductor industry. Nevertheless, not enough efforts have been made to well response debates (such as the electrical performance, and the resistance switching mechanisms) yet.

Another main stream is green energy because of sustainable energy resources. It includes solar photovoltaics, solar thermal, wind power, biomass, water power, and geothermal. Solar photovoltaics, converting solar energy into electricity using solar cells, have much more potential in green energy because of less limitation factors such as assembly locations. However, many issues, such as the performance of solar cells, still have to be much

more concerned.

Nanotechnology has been widely investigated for decades and has become a mature technology nowadays. Applying nanotechnology in ORM and solar cells has potential to make both exhibit superior performance and to help us deal with the difficulties of both. It is also possible to help us realize more green devices, and thus, more green technology.

1.2 Organic Resistive Memory

With advancing progress in science and technology, the demands for more accurate simulations in research and for consumer electronic devices are increasing dramatically. Along with this trend, a tremendous demand for increased capacity of memory devices is also evident. In order to satisfy this current demand, the capacity of conventional memory devices (such as dynamic random access memory, and flash memory) has been augmented by scaling technology. [3] However, scaling technology will reach its physical limit in the near future. To overcome the scaling limit, various new memory devices such as single electron memory [4], spin memory [5], phase-change memory, [6] and ORM [7] have been investigated. ORM has attracted considerable attention due to superior characteristics: simple structures (e.g., electrode/organic material(s)/electrode), high-density integration (Fig 1.1), fast-writing/ erasing-operation speeds, and low-power consumption.

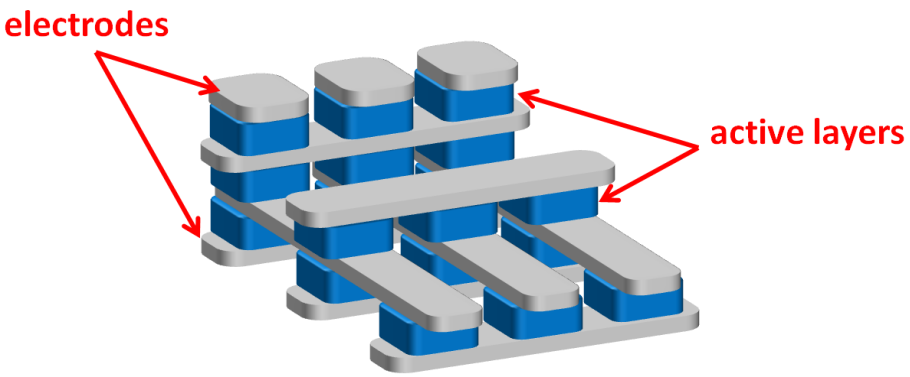

Fig. 1.1 The illustration of the three dimension (3D) stacking of ORM.

ORM is a memory device which has not less than two conductivities at the same applied voltage. For an organic bistable device (OBD), ORM with two conductivities, with a normally OFF/ON state, it holds at a low/high conductance state at the beginning when a writing bias is applied to it. It will change to a high/low conductance state as the bias passes a threshold voltage (or a set/reset voltage). When applied a reading bias, the device still holds at the high/low conductance state. It is obvious that this device exhibits two obviously different currents at the same applied voltage. In addition, the device can be switched back to the low/high conductance state again after an erasing bias (or a reset/set voltage) is applied to it. According to the electrical properties of OBDs have been published, the current-voltage (I-V) curves of OBDs can be roughly grouped into 4 types: symmetric S-shaped, asymmetric S-shaped, N-shaped, and O-shaped, as shown in Fig. 1.2. [8]

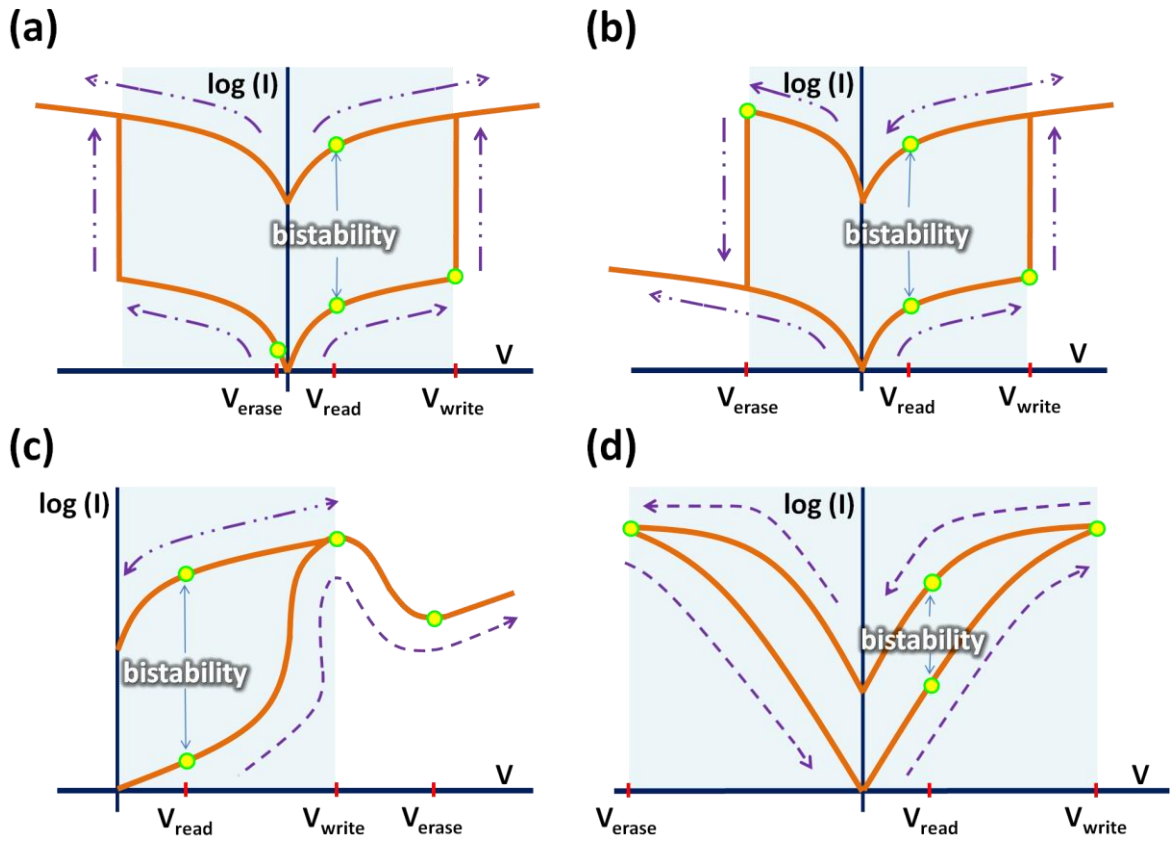

Fig. 1.2 4 types of I-V curves of OBDs. (a) Symmetric S-shaped. (b) Asymmetric S-shaped. (c) N-shaped. (d) O-shape. [8]

The resistance switching of insulating materials which is responsible to an applied bias above a certain threshold voltage (forming or electroforming) has been investigated since T. W. Hickmoot reported the resistance switching of Al_2O_3 in 1962. [9] Then, the resistance switching of insulating materials are also found in SiO, [10] ZnS, [11] and TiO [12] and polymeric insulators [13]. The resistance switching has attributed to the injection of metal ions from the electrodes (resulting in impurity bands in the insulators) [10], conducting filamentary pathways forming (from electrolytic processes [14], or the metallic electrodes [15]), carbonaceous material (from the insulator itself or sources introducing during fabrication [16]), and tunneling between metal particles/clusters produced during the electroforming process [17]. Although a number of published papers elucidate their results using the filamentary formation, the causes of the resistance switching have not been clearly understood so far.

The first report on the resistance switching of organic devices, which was found in the glow-discharge-deposited poly(divinylbenzene) interposed between lead electrodes, was at 1968. [18], [19] Then the resistance switching were also observed in other glow-discharge polymers: styrene, [20], [21] acetylene, [21] benzene, [21] and aniline, [21] and in small organic molecules: tetracene [22], [23] and perylene [23]. Although investigation on the resistance switching had proceeded in past decades, the apparent progression was made after Ma et el. proposed a three-layer structure (organic/metal-nanocluster/organic) deposited between two Al electrodes. The organic layers are 2-amino-4,5-imidazoledicarbonitrile (AIDCN), and the metal-nanocluster layer (discontinuous metal nanoclusters) is introduced by evaporating a thin metal layer in the presence of oxygen or AIDCN. [24]-[27]

Up to now, the resistance switching has been demonstrated by numerous organic materials which can be classified into five categories: small molecules, polymers, donor-acceptor complexes, mobile-ion and electrochemical systems, and nano-particle (NP) blends. [28]

For small molecules, anthracene, [29] 9,10-bis-(9,9-diphenyl-9*H*-fluoren-2-yl) anthracene (DPFA), [30] pentacene, [31] aluminum tris(8-hydroxyquinolate) (Alq_3), [32]-[35] *N*,*N*'-di(naphthalene-1-yl)-*N*,*N*'-diphenyl-benzidine (NPB), [34] AIDCN, [36] molecules with various acceptor groups for tuning ON/OFF ratios (such as 2,3-dichloro -5-6-dicyano-1,4-benzo-quinone (DDQ)), [37], [38] and squarylium dye Langmuir–Blodgett films [39] have been used as the active layers of ORM.

The active layers of ORM using polymers include insulators (like poly(butylmethacrylate) (PBMA), [40] poly(ethylmethacrylate) (PEMA), [40] poly(methylmethacrylate) (PMMA), [40] polystyrene (PS), [35], [40], [41] and poly(vinylcarbazole) (PVK) [42]), conjugated polymers (like poly [3-(6-methoxyhexyl) thiopene] (P6OMe), [43], [44] poly[2-methoxy-5-(3',7'-dimethyloctyloxy)-1,4-phenylene vinylene] (OC_1OC_{10}), [35] polyspirofluorene, [35] and poly[2-methoxy-5-(2'-ethyl-hexyloxy)-1,4-phenylene vinylene] (MEH-PPV) [45]), copolymers (like poly(methylmethacrylate-co-9-anthracenyl-methylmethacrylate) (MDCPAC) [46]), and small molecule/polymer multilayer structures using electrostatic self-assembly methods (like nickel phthalocyanine/poly(allylamine hydrochloride), [47] and Rose Bengal/poly(allylamine hydrochloride) [48], [49]).

The resistance switching of donor-acceptor complexes (DA complexes) results from charge-transfer induced by an applied electrical field. Potember et al. report the earliest resistance switching on Cu-tetracyanoquinodimethane (Cu-TCNQ). [50] TCNQ is the organic electron acceptor, and Cu can transfer electrons to TCNQ to from CuTCNQ (a charge transfer complex) when an electrical field is applied to the Cu-TCNQ thin film. Moreover, the resistance switching of organic-organic DA complexes (such as 2,6-bis(2,2-biscyanovinyl) pyridine (BDCP) and decacyclene (DC), [51] PVK and rare earth complexes (Sm^{3+}, Gd^{3+}, or Eu^{3+}), [52] and poly(3-hexyl thiophene) (P3HT) and functionalized carbon nanotube (CNT) [53]), of DA complexes in a host polymer matrix (such as 6,6-phenyl-C61-butyric acid methyl ester (PCBM) and tetrathiafulvalene (TTF) in the PS host matrix [54]), and of DA

copolymers (such as a copolymer of europium vinylbenzoate complex (EuVB) and PVK, [55] a copolymer of 9,9-dihexyl-9*H*-fluorene-2,7-bis(trimethyleneboronate), 2,7-dibromo-9,9-di-hexyl-9*H*-fluorene, and 5,5'-bis(5-(4-bromo-3,5-bis(2-ethylhexyloxy)phenyl)-1,3,4-oxadia-zol-2-yl)-2,2'-bipyri-dine, [56] and a copolymer of EuVB and polyfluorene (PF) [57]) have been demonstrated as well.

In mobile-ion and electrochemical systems, ions in organic materials can be highly mobile. The external applied electrical fields can electro-deposite/de-solute the ions to generate/destroy the conducting paths (e.g., Cu ions coupling with Alq_3, AIDCN, and 2,9,16,23-tetra-*tert*-butyl-29*H*,31*H*-phthalocyanine (ZnPc) [58]), can dissociate salts into ions to displace and/or accumulate (e.g., NaCl in polyphenylacetylene, [59] and sexithiophene-poly(ethylene oxide) (6T-PEO) adjacent with a poly(ethylenedioxythio -phene):poly(styrenesulfonate) (PEDOT:PSS) with a NaCl layer [60]), and can electrochemically oxidize/reduce the polymers with ions (e.g., a MEH-PPV/$RbAg_4I_5$ bilayer structure [61]), and then the resistance switching occur.

Nanostructured materials (such as metal NPs) have attracted much attention in ORM because the corresponding devices can exhibit better performance such as high ON/OFF ratios. The proposed nanostructured materials include Al discontinue nanoclusters, [24]-[27], [62], [63] Au NP blends (such as Au capped with triphenylphosphine (Au-TPP), [62] Au capped with dodecanethiol (Au-DT), [64]-[66] and Au capped with naphthalenethiol (Au-NT) [65], [67]), nanostructured Ag (such as Ag-ultrafine-particle–toluylene 2,4-dicarbamidonitrite (Ag-UFP-TDCN), [68] Ag NPs in a plasma polymer film, [69] Ag islands in *N*,*N'*-diphenyl-*N*,*N'*-bis(3-methylphenyl)-1,1'-biphenyl-4,4'-diamine (TPD), [79] and a fine Ag layer in a polyfluorene (PF) film with cyano side groups [71]), Pt NPs (such as Pt NPs into tobacco mosaic virus [72]), and other nanostructured materials (such as ZnO NPs, [73] MoO_x NPs, [74] MoO_x nanoclusters, [75] Cr NPs, [62] Mg NPs, [62] and CuPc NPs [62]).

Even though many research papers on the mechanism of the resistance switching of

ORM have been published, the physics responsible to the resistivity switching is not clearly known and largely debated. However, the primary proposed mechanisms include filamentary conduction, [33], [58] nanoparticle/nanocluster charging (charge trapping), [66], [75] charge transfer, [50], [64] and the conformation effects. [76], [77]

Filamentary conduction is a phenomenon that the current of a high conductance state is highly localized to a small fraction of the device area. When the devices are under electrical stress (or current stress), local fusing, the migration of electrode materials, or the alignment of NPs can form conductive filaments through the films, and thus the devices become at a high conductance state. These filaments can be ruptured by larger electrical stress (or current stress), and consequently the devices are switched back into a low conductivity state, as shown in Fig. 1.3.

Take a Cu-induced OBD (Cu (anode)/buffer layer/organic layer/Cu (cathode)) [58] as an illustration. Under a positive bias, Cu atoms close to the anode/buffer layer interface become ionized, and ionized Cu can drift into the organic layer and then towards the cathode. After they reach the cathode, Cu filaments are established within the organic layer, and therefore the organic layer is metalized (the high conductance state). When the applied bias exceeds a critical voltage which can break the Cu filaments via burning, the OBD change to the low conductance state again.

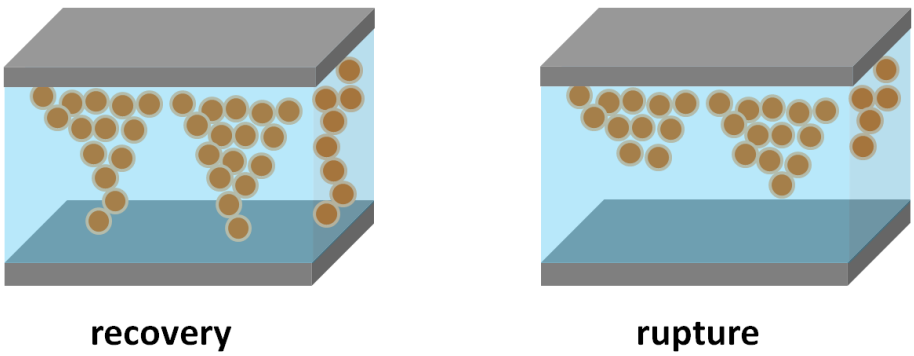

Fig. 1.3 The illustration of filamentary conduction.

Moreover, filamentary conduction possess two features: (a) the current of the high conductance state will exhibit ohmic relation in I-V curves and will increase with decreasing temperature, and (b) the current of the high conductance state is independent on (or insensitive to) the device area in that the dimension of filaments is much smaller the device area.

Nanoparticles/nanoclusters can trap transporting carriers, and/or donate electrons or accept electrons under an (large enough) external electrical field. After them are charged to some extent, ORM will alter the pristine conductance state into another one as a result of trap-free, or a change in material properties (such as the electronic structure). Take a blended thin film which composes of Au-DT NPs in the PS [66] as an instance. The Au-DT NPs act as trap sites in the PS because the work function of the Au-DT NPs is around 5.1 eV lower than the lowest occupied molecular orbital of PS. When the film is applied a bias, its conductance is low initially due to charge trapping. However, as soon as the bias is larger than a voltage which the traps are completely filled, its conductance is largely enhanced, and the carrier transport mechanism is dominated by space charge limit current (SCLC), [78] as shown in Fig. 1.4. It should be noted that not only SCLC but also Poole–Frenkel emission, [79] Fowler–Nordheim [80] and direct tunneling [81] probably involve the carrier transport mechanism of the ORM using nanoparticles/nanoclusters.

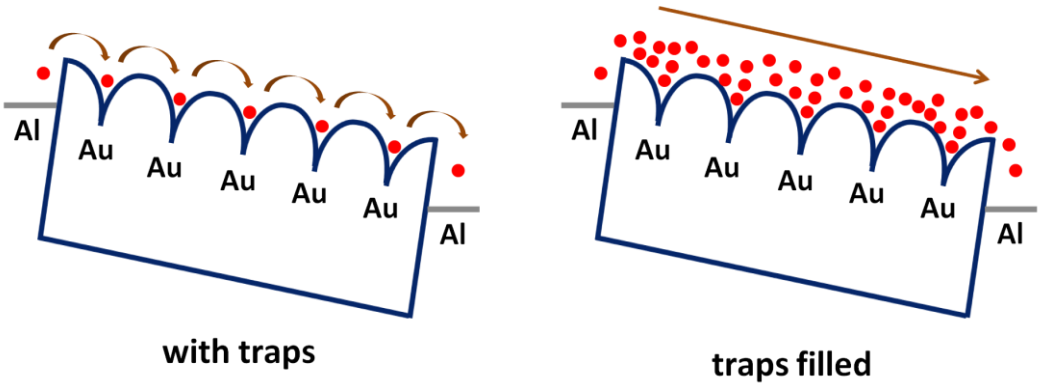

Fig. 1.4 The illustration of nanoparticle/nanocluster charging. [66]

A charge transfer effect is that a DA complex transits to an excited state in which a fraction of electronic charges is transferred between the donor to acceptor moieties. The resulting electrostatic force can either enhances or diminishes an external voltage applied to the devices. As a result, the devices can switch into a high or low conductance state. For example, a blended thin film consists of 8-hydroxyquinoline (8HQ) (electron donor), Au-DT NPs (electron acceptor), and PS (matrix). [64] Under an electric field, the carrier concentration of the blended thin film is quite low. However, as long as the electrical field increases to a certain value, electrons on the highest occupied molecular orbital (HOMO) of 8HQ can acquire enough energy to tunnel through DT into the Au NPs, as shown in Fig. 1.5. Therefore, the HOMO of 8HQ is partially filled, and the blended thin film is polarized. Then, the carrier concentration of the blended thin film is increased.

A conformation is defined as a possible shape of macromolecules corresponding to changes in their environment or other factors. A transition between the conformations is called a conformational change. A macromolecular conformational change may be induced by many factors such as electrical stress. Each conformation has its electrical conductance so the devices using macromolecules can alter their conductance under electrical stress. Take the catenane, [76] as shown in Fig. 1.6, for example. The catenane composes of a tetracationic cyclophane with two bipyridinium units, interlocked a crown ether with a tetrathiafulvalene

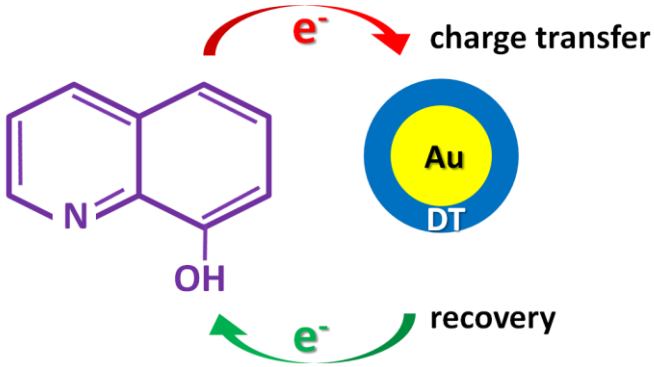

Fig. 1.5 The charge transfer between an Au NP and 8HQ. [64]

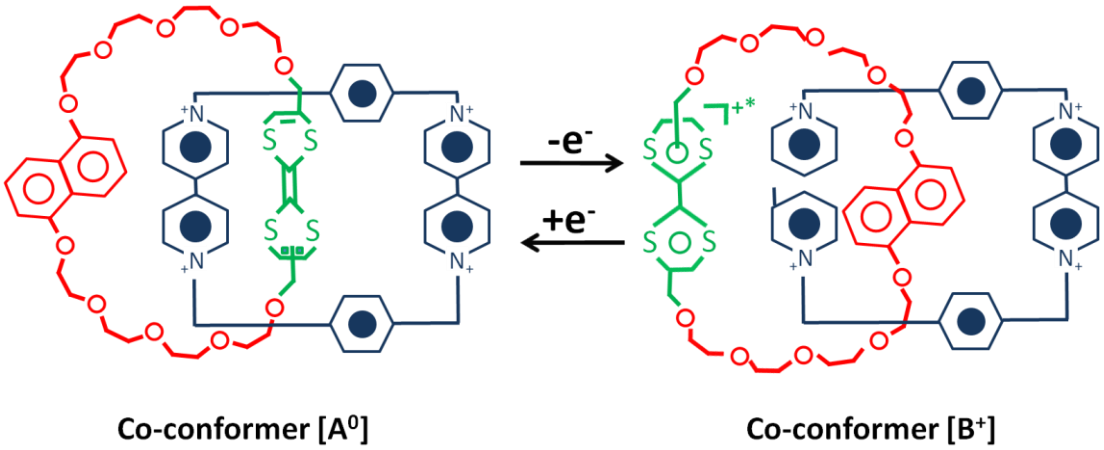

Fig. 1.6 The conformational change of the catenane. [76]

(TTF) unit and a 1,5-dioxynaphthalene ring system. The ground state of the catenane ("co-conformer" [A^0]) has the TTF unit inside the cyclophane. After oxidation, the TTF unit is positively charged, and the Coulombic repulsion between TTF^+ and the tetracationic cyclophane makes the crown ether circumrotate and then "co-conformer" [B^+] is formed, which will reduce back to [B^0] when the bias is returned to 0 V. The "co-conformer" [B^0] can give larger output current than the "co-conformer" [A^0]. The bistablity builds the basis of this device.

ORM is an emerging memory device and has many potential advantages. However, the electrical performance of ORM demonstrated so far cannot fit the requirements of next generation memory devices as well as the switching mechanisms are debated. For matching the requirements, improving the performance of ORM and making the responsible mechanisms clear are two key challenges of ORM. In addition, exploring emerging ORM based on nanomaterials, nanostructures, and/or low-cost fabrication techniques for the next generation green devices is always there.

1.3 Solar Cells

Solar cells are apparatus which can convert light energy into electrical energy. When

sunlight illuminates into solar cells, photons larger than the bandgap of the active layer(s) are absorbed and then excited electron-hole pairs are generated. Before they relax to the ground state, the excited electron-hole pairs will be separated by a built-in asymmetry in the solar cells, and then the separated carriers are collected by electrodes. Finally, a potential difference (a photovoltage) between the electrodes which can drive electrons through external loads is generated.

The first report on the photovoltaic effect is that Edmud Bequerel observed an electric current generated by an Ag coated Pt electrode in the electrolyte under light illumination in 1839. In the following year, many kinds of solar cells were created (such as thin film Schottky barrier devices). With the development of silicon based solid state electronics in 1950s, the first pn junction silicon solar cell was made by D. M. Chapin, C. S. Full, and G. L. Pearson in 1954. [82] Its conversion efficiency is up to 6%. However, silicon solar cells were not widely applied in daily life for power generation at that time because of the high production cost, but in space. In addition, other type pn junction solar cells such as cadmium sulphide were also created in 1954, and many simulation works on solar cells using gallium arsenide, indium phosphide, and cadmium telluride were revealed as well. A big progress in solar cells occurred at the energy crisis in 1970s due to the huge amount of funding for research and development of alternative energy resources. As a result, new approaches for producing solar cells (such as photoelectrochemical junctions [83]) and cheap materials (such as polycrystalline silicon, [84] and amorphous silicon [85]), and for improving the performance of solar cells (such as multiple bandgap structures [86]) were intensively proposed. After the 1990s, not only the fabrication technologies of solar cells have been well developed, but the awareness on the sustainable energy resources and environment protection has been growing, and thus solar cells have been gradually expending into the electricity market. In order to accelerate the popularity of solar cells, high efficiency, low cost solar cells, and their applications (such as building integrated photovoltaic applications [87]) have greatly been

concerned.

The current density-voltage (J-V) curve of a solar cell under illumination can be expressed by

$$J(V) = J_{sc} - J_o\left(e^{\frac{qV}{nk_BT}} - 1\right) \tag{1.1}$$

where J_{sc}, J_o, q, n, k_B, and T are short-circuit current density, reversed saturation current density, elementary charge, diode factor, Boltzmann constant, and temperature. The n is typically between 1 and 2. n approaches 1 as the diffusion current density of minority carriers dominates the carrier transportation mechanism. n approaches 2 as the recombination current density in the space charge region does. When two terminals of the solar cell are open-circuit (J=0), which the dark current density cancels out the J_{sc}, the potential difference between the two terminals is the open-circuit voltage (V_{oc}), as expressed in Eq. (1.2).

$$V_{oc} = \frac{nk_BT}{q}\ln\left(\frac{J_{sc}}{J_o} + 1\right) \tag{1.2}$$

Afterwards, when the solar cell connects with a load(s), the delivered power density is given by Eq. (1.3).

$$P = JV \tag{1.3}$$

The maximum delivered power density (P_{max}) locates at some voltage (V_m) and a corresponding current density (J_m) in the J-V curve. The ratio of V_mV_m to $V_{oc}J_{sc}$ is defined as the filling factor, as given in Eq. (1.4).

$$FF = \frac{V_mJ_m}{V_{oc}J_{sc}} \tag{1.4}$$

The conversion efficiency of the solar cell (η) is the maximum delivered power as a fraction of incident power density (P_i), as expressed in Eq. (1.5).

$$\eta = \frac{P_{max}}{P_i} = \frac{V_mJ_m}{P_i} = FF\frac{V_{oc}J_{sc}}{P_i} \tag{1.5}$$

The J_{sc}, V_{oc}, FF, and η (P_{max}/P_i) of the solar cell , as shown in Fig. 1.7 are critical parameters

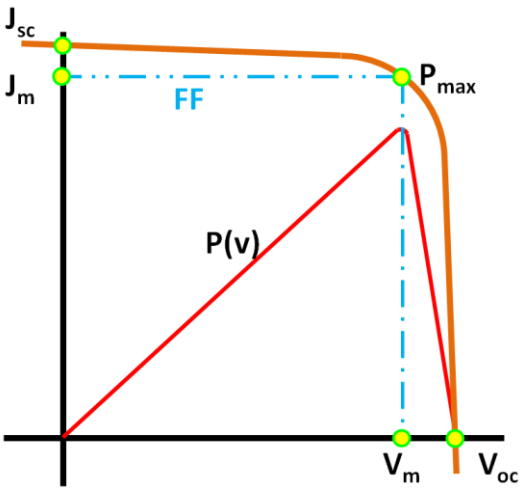

Fig. 1.7 The illustration of the main parameters of solar cells.

for describing its performance under a specific condition (e.g., the standard test condition: at 25℃, air mass 1.5 illumination (100 mW/cm^2)).

A real solar cell always contains nonideal factors (e.g., parasitic resistance, and surface recombination) to dissipate its delivered power density. Take the parasitic resistance of the solar cell as an example. It comprises series resistance (R_s) and shunt resistance (R_{sh}), which are illustrated by Fig. 1.8 and which the corresponding J-V curve is expressed by Eq. (1.6). R_s results from the resistance of materials and the contact resistance in the interfaces (such as the metal-semiconductor contact). R_{sh} is introduced by leakage current paths (such as surface defects, and worse edge isolation). R_s makes influences on the J_{sc} but less on V_{oc}. However,

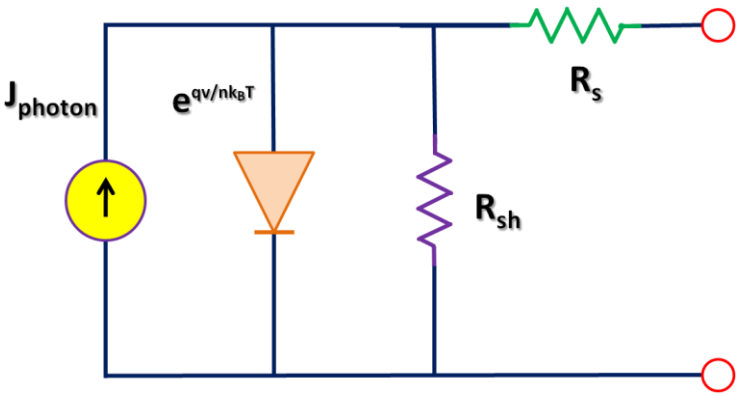

Fig. 1.8 The equivalent circuit of solar cells.

R_{sh} behaves in opposite trend. Moreover, large R_s and small R_{sh} reduce the FF, and thus the potency of the solar cell. It suggests that an efficient solar cell ought to be with R_s as small and with R_{sh} as large as possible.

$$J(V) = J_{sc} - J_o\left(e^{\frac{q(V+JR_S)}{nk_BT}} - 1\right) - \frac{(V+JR_S)}{R_{sh}} \quad (1.6)$$

Current photovoltaic technologies can be categorized into three main groups: the silicon type, the compound type, and the new materials, as shown in Fig. 1.9. The silicon type includes bulk crystalline Si (single crystalline, [82], [84], [88]-[90] multicrystalline, [84], [91]-[94] and hetero-junction with intrinsic thin-layer [95], [96]), and Si thin films (single crystalline, [97], [98] multicrystalline, [99], [100] amorphous, [85], [101], [102] and multijunctions [103], [104]). Si is a chief material in solar cells due to its earth-abundance, non-toxicity, and stable oxide compounds, and to the well-developed Si based industry, although Si is an indirect bandgap material. In this type of solar cells, single crystalline Si gives the highest efficiency up to present. However, the production cost is also the most expensive. For reducing the cost, other Si based solar cells have been interested. Take amorphous Si thin film solar cells as an example, the absorption properties of amorphous Si thin films are superior to those of bulk Si, and consequently, material usage is largely reduced, which shifts to cut down the cost. The compound type comprises bulk crystalline III-V compounds (single junction, [105] and multijunction [86], [106-[108]), III-V compound thin films, [109], [110] II-VI compound thin films (such as CdTe), [111]-[114] and I-III-VI_2 compound thin films (such as $Cu(In_xGa_{1-x})Se_2$ [115]-[118]). In all kinds of solar cells, single crystalline III-V compound solar cells are the champion cells nowadays (η with up to 40%). [107], [108] Comparing with crystalline Si ones, the cells consume less materials and assembly areas under the same output power. However, they are much more costly. With regards to II-VI and I-III-VI_2 compound thin film solar cells, they have potential to compete with Si based photovoltaics as a result of their natures: direct bandgap materials (high

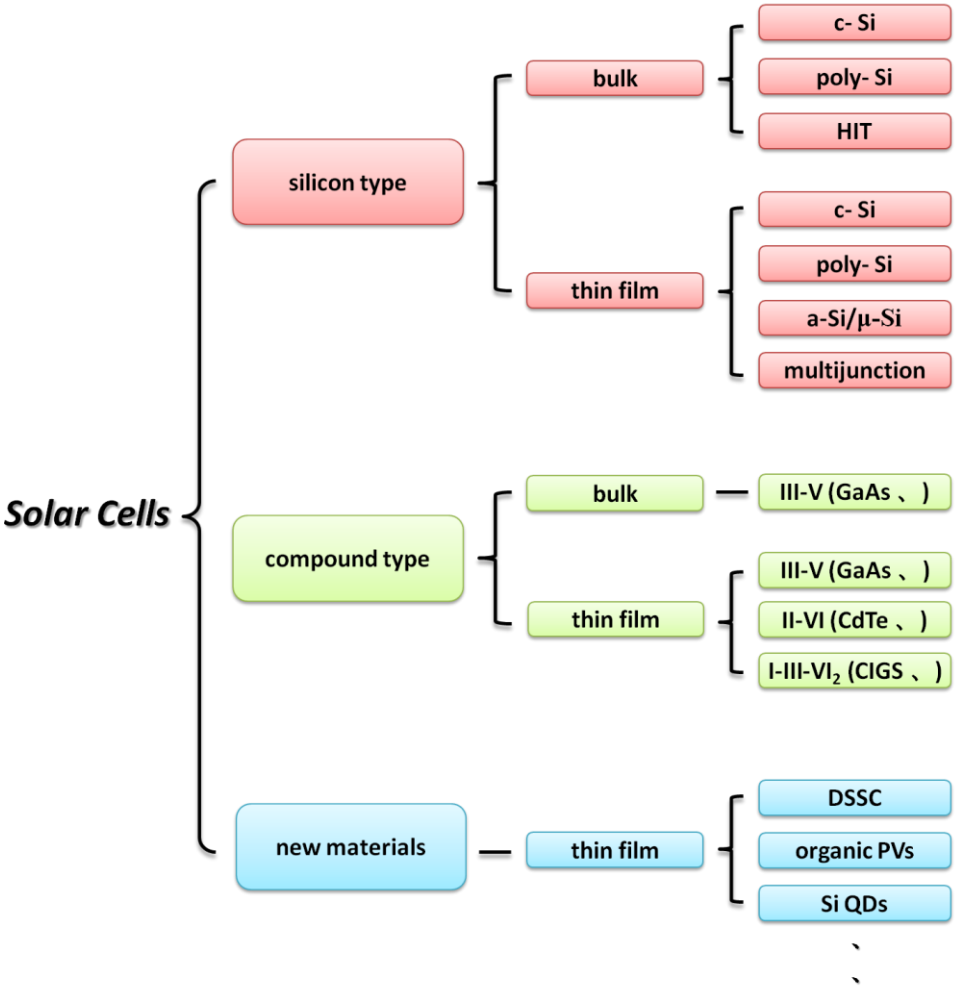

Fig. 1.9 The family of solar cells.

absorption coefficients), and flexibility in bandgap engineering. The new materials cover dye-sensitized solar cells (DSSC, thin film), [119]-[122] organic photovoltaics (OPVs, thin film), [123]-[127] and ultra high efficiency photovoltaics (such as quantum dots, [128] hot carriers, [129], multiband, [130], [131] and multiple excitation [131]). Both DSSC and OPVs are made of low-cost materials which can change their bandgaps by molecular engineering, and do not require elaborate apparatus for manufacturing; accordingly, are potentially lucrative for photovoltaic applications. Unfortunately, further investigation and improvement on their efficiency, stability, and strength are necessary for paving their roads on the photovoltaic market. In the case of ultra high efficiency photovoltaics, they attend to tackle power losses of solar cells (such as the thermalization loss [132]) for achieving over 31%

efficiency (the efficiency limit of single junction solar cells [133]). Even if it is still early days, they manifest to have enormous potential in photovoltaic technology, possibly permitting more than two times obtainable cell energy conversion efficiency.

To take the place of nonsustainable energies (like fossil fuels, and uranium) in the near future, decreasing the capitalized cost of power converted by photovoltaics is our key challenges. Mass production, efficiency improvement (such as by new structure designs, new materials, and nanotechnologies), and novel photovoltaics (such as hot carrier cells) are much beneficial for lowering the cost. For example, uplifting 1% of the energy conversion efficiency of bulk single crystalline Si solar cells can cut down about 7% of the cost. [132] In addition, extending the applications of photovoltaics (such as BIPV and solar hydrogen) can also accelerate efficiently the popularization and developing of photovoltaics.

1.4 Nano Films

Nanotechnology is an applied science which studies the structures sized between 1 nm to 100 nm in at least one dimension. The corresponding thin films are nano films, which include films composed of nanocrystallites, [134], [135] composite films which nanocrystallites embedded in a film(s), [136], [137] 1 to 100 nm thick films, [138], [139] or multilayer films which 1 to 100 nm thick films stack in pairs. [140], [141] Because of their nature (the dimension of nanocrystalites, the thickness of films, surface roughness, and the structures of multilayers), numerous distinct physical or chemical properties of nano films [134]-[152] from bulk materials have been observed in mechanics, electronics, optics, and other research fields. For example, two ferromagnetic layers are separated by a very thin nonferromagnetic layer (e.g., Fe/Cr/Fe). The electrical resistance (magnetoresistance) of the structure is determined by the magnetization of the adjacent ferromagnetic layers (parallel or antiparallel alignment). It is interesting that the deviation of the magnetoresistance of the structure is extremely larger than that of conventional magnetic metals and alloys (giant

magnetoresistance). [142] Following is the brief introduction of part characteristics of nano films in electronics and optics.

In electronics, nano films can manipulate the behaviors of charge carriers. Four cases are given below.

(a) For crystallized particles or thin films, surface states which result from the broken periodic lattices at their surfaces can gradually change the pristine transportation behaviors of carriers when their dimension is decreasing, especially close to the range of the wavelength of electrons. For instance, the surface states can increase the charge storage time of a Si nanocrystal thin film. [144]

(b) A nano film(s) interposed between (composite) thin films can be trap states to catch carriers, and thus modulate the features of the (composite) thin films or corresponding devices. For example, a SiN_x nano film, inserted between two SiO_2 thin films, can act as the charge trapping centers of memory devices due to the energy barriers between SiN_x and SiO_2. [140]

(c) A particle with kinetic energy lower than the potential barrier of a thin film cannot penetrate the barrier until the thickness of the thin film is thin enough (e.g., SiO_2 < 2nm), vastly different from the prediction of the classical physics. [135], [145]

(d) As the dimension of thin films is close to the Bhor radii of materials, continue energy states in the conduction band and valence band become discrete energy states. Then electrons can be largely injected into the thin films only if the Fermi level of the electrodes aligns with the discrete energy levels (Column blockade). [146], [147]

In optics, nano films can help mold the flow of light. Two examples are presented as follows.

(a) When electromagnetic (EM) waves pass through metal NP thin films, electrons on the metal NPs will oscillate with the EM waves, and then surface plasma is generated. As long as the frequency of EM waves are close to the resonance frequency of the metal NPs, localized surface plasma oscillation cause extensive light absorption. [148], [149]

(b) As the dimension of thin films shrink to make discrete energy states generate instead of continue energy states in the conduction band and valence band, we can observe blue shifts in the photoluminescence spectrum and absorption spectrum because of the enlargement of effective bandgaps. [137], [150]

Even though the dimension of nano films is far from that of bulk materials, nano films for some specific functions which are not provided by bulk materials can be easily fabricated using physical (such as sputtering) or chemical (such as synthesis) methods nowadays. For example, a nano film (or a nanostructured layer) can be the trapping layer of ORM for realizing the resistance switching. [75] Due to their promising characteristics, we can anticipate that applying nano films in ORM and solar cells will accelerate the progress of both, which in turn promote that of the green technology.

1.5 The Motivation And Structure of This Dissertation

Nano films have been widely applied in the numerous research fields because of their potential properties. In this dissertation, we use three kinds of ultrathin oxide layers (oxide nano films) to realize two OBDs and one solar cell for giving alternative solutions to the physical limit in the future scaling technology and for extending the functions of solar cells, respectively.

In the beginning, we fabricate and analyze an OBD with an n-Si/Alq_3/Al structure, which an ultrathin Al-O compound layer forms unintentionally at the Alq_3/Al interface. According to published results, the properties of interface oxide layers between the organic

layer and the electrode make influences on the characteristics of OBDs. In order to understand the effect of the ultrathin Al-O compound layer on our OBD, we investigate the characteristics of OBDs with the same structure made at different Alq_3 deposition rates.

Moreover, we study an OBD using a nanostructured MoO_x layer interposed by two Alq_3 layers. The nanostructured MoO_x layer can be trap sites to produce the resistance switching of the OBD under electrical stress due to the energy barrier between MoO_x and Alq_3. In organic electronics, MoO_x has been extensively used to improve their performance. It suggests that the OBD can be easily integrated with other organic electronics.

In addition to the two OBDs, ultrathin oxide layers also play an important role on the photovoltaic features of Schottky solar cells. Inserting ultrathin oxide layers in the Schottky solar cells, metal-insulator-semiconductor (MIS) solar cells, can provide larger V_{oc} under sunlight. MIS solar cells with high V_{oc} appear a promising application, converting solar energy for hydrogen production, and can reduce the contact loss of photovoltaic modules. However, the V_{oc} of MIS solar cells is not larger than the dissociating potential of water (1.23 V). A stacking MIS solar cell is proposed to further enhance V_{oc}, and has potential to provide a V_{oc} beyond 1.23 V.

This dissertation comprises six chapters. Chapter 1 gives the background and motivation of the studies. Then, the fabrication and characterization methods of samples are presented in Chapter 2. The following two chapters pay attention to the characteristics of an OBD with an interfacial oxide layer, and then involve the electrical features of an OBD with a nanostructured oxide layer. Materials in the Chapter 5 demonstrate a high V_{oc} stacking MIS solar cell for a future photovoltaic application in water splitting. Finally, the conclusions and future works of this dissertation are summarized in Chapter 6.

Chapter 2

Fabrication And Characterization Methods

2.1 The Fabrication of Organic Bistable Devices With Interfacial Oxide Layers

The OBDs consists of an Alq_3 thin film interposed between n-Si and an Al electrode, as shown in Fig. 2.1. The fabrication procedures of the OBDs are described as follows and are illustrated in Fig. 2.2. First, 1 Ω-cm resistivity n-type silicon substrates were clean through the standard RCA cleaning process, as shown in Fig. 2.3. Then, 150-nm-thick Alq_3 thin films were deposited on the cleaned substrates kept at room temperature by thermal evaporation in a vacuum below 3 x 10^{-6} Torr. Finally, 80-nm-thick Al top-electrodes were deposited on the Alq_3 thin films through shadow masks. The area of each Al electrode is 0.64 mm^2. The deposition rates of the Alq_3 thin films are 0.05 nm/s, 0.15 nm/s, 0.2 nm/s, and 0.3 nm/s. The

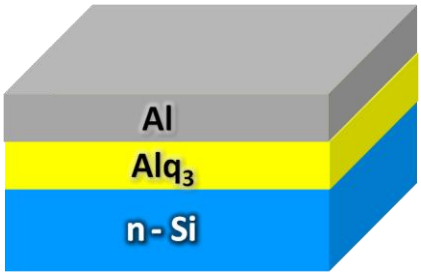

Fig. 2.1 The structure of OBDs with interfacial oxide layers

Fig. 2.2 The fabrication flow of OBDs with interfacial oxide layers.

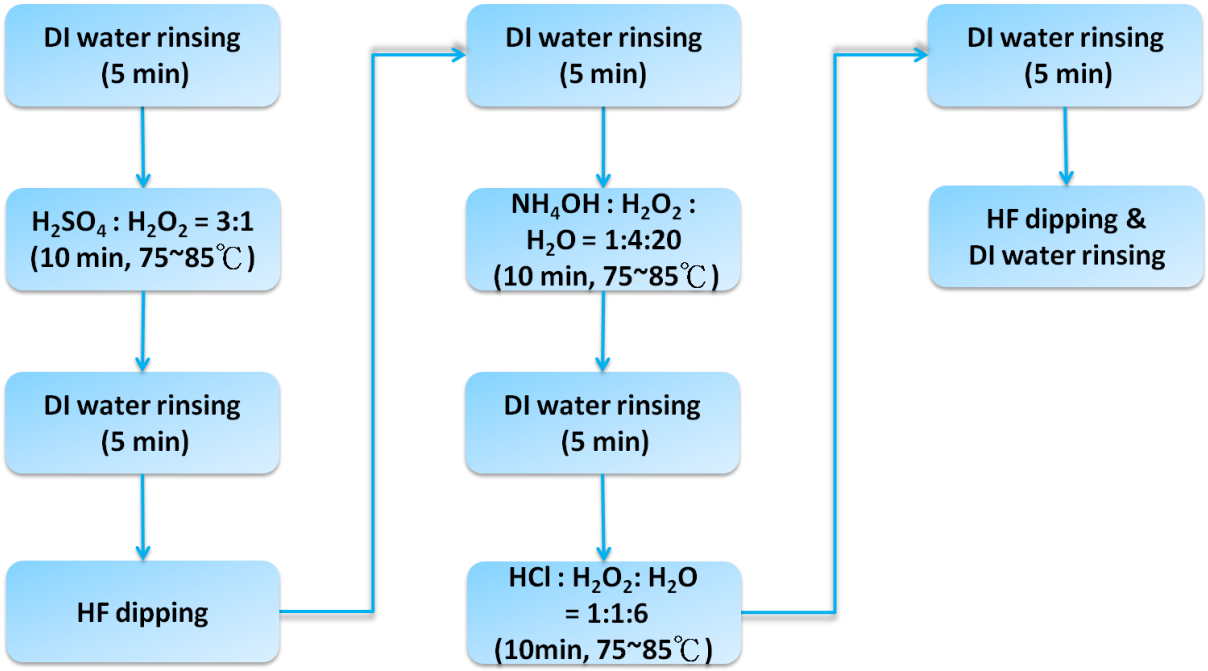

Fig. 2.3 The RCA cleaning process

deposition rates are controlled by setting the temperature of crucibles and are monitored by the quartz crystal microbalance. The corresponding setting temperature for each deposition rate is listed in Table 2.1.

2.2 The Fabrication of Organic Bistable Devices With Nanostructured Oxide Layers

The OBDs consist of an $Alq_3/MoO_x/Alq_3$ tri-layer structure interposed between top and bottom electrodes, as shown in Fig. 2.4, and fabrication procedures are illustrated in Fig. 2.5.

Table 2.1 The setting temperatures corresponding to the four deposition rates of Alq_3 thin films, and the properties of the Alq_3 thin films obtained from XPS measurements for the four deposition rates.

Deposition Rate (nm/s)	Setting Temperature (℃)	N (atom%)	N/C
0.05	251.7	6.8	0.075
0.15	267.5	6.2	0.068
0.2	274.1	6	0.066
0.3	281.3	5.9	0.065

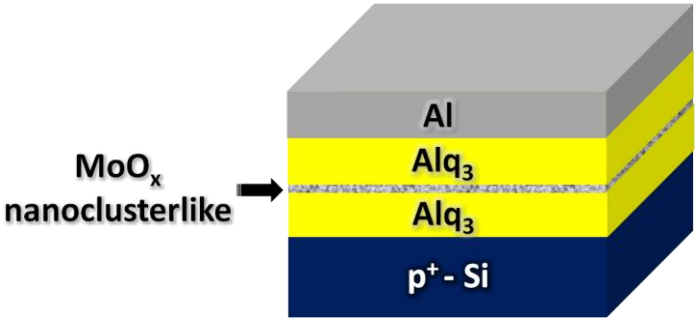

Fig. 2.4 The structure of OBDs with nanostructured MoO_x layers.

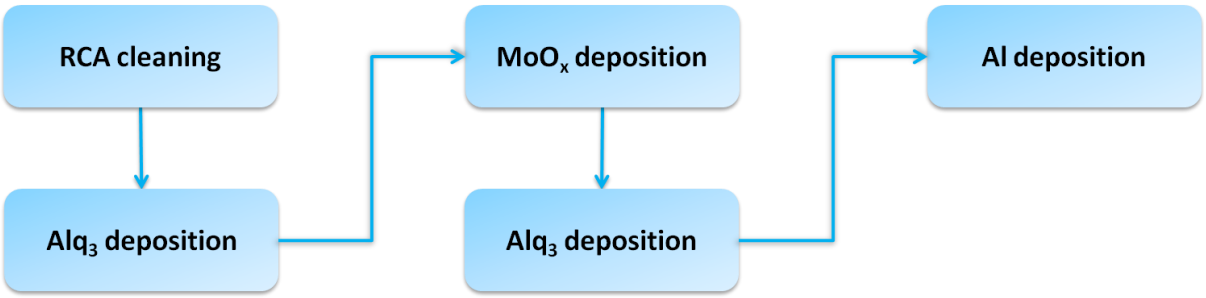

Fig. 2.5 The fabrication flow of OBDs with nanostructured MoO_x layers.

First, 50-nm-thick Alq_3, XX-nm-thick MoO_x, and 50-nm-thick Alq_3 thin films were evaporated in sequence onto cleaned p^+-type silicon substrates. The XX is equal to 3, 5, and 8. The average deposition rates of the Alq_3 thin films and that of the MoO_x layers are about 0.1 and 0.01 nm/s, which are monitored by the quartz crystal microbalance, respectively. Finally, 100-nm-thick Al thin films as the top electrodes were evaporated through metal masks with 2 mm x 2 mm square patterns. Note that all materials were evaporated at a vacuum bellow $3x10^{-6}$ Torr and the substrates were kept at room temperature during fabrication.

2.3 The Fabrication of Metal-Insulator-Semiconductor Solar Cells

The thickness of the insulating layers of MIS solar cells affects the blocking efficiency of their majority carriers and the tunneling probability of their excess minority carriers; hence, it influences their potency. Although thermal SiO_2, [151]-[157] chemical SiO_2, [158] evaporated SiO_x, [159] and SiO_2 using an anodization technique [160] have been used as their

ultrathin insulating layers, controlling the thickness of the insulating layers well is still difficult to achieve. To easily control the thickness and to produce the insulating layers at the low temperature, radio frequency (RF) magnetron sputtering is adopted to deposit the ultrathin SiO_2 layers.

The n/p-type MIS solar cells were fabricated using phosphor/boron-doped (100) silicon substrates with resistivity ranging from 1 to 10 Ω-cm. The fabrication procedures are shown step by step in Fig. 2.6. First, ultrathin SiO_2 layers were sputtered on n/p-type silicon substrates, which had cleaned through the standard RCA cleaning process, by RF magnetron sputtering under different working pressures. The thickness of the ultrathin SiO_2 layers is controlled by sputtering duration. The optimized thicknesses for the n-type and p-type silicon substrates are about 2 and 1 nm, which the ultrathin SiO_2 layers were sputtered at 20 mTorr, respectively. Thicker sputtering SiO_2 insulating layers are required for the n-type MIS solar cells to suppress the larger tunneling probability of the majority carriers.

Then, most samples were annealed in H_2 atmosphere at 500℃ for 1 hour, but the others are not for being reference samples. Finally, Al/Au(-Ni) films as the back electrodes, semi-transparent 20/10-nm-thick Au/Al thin film layers on the top of the ultrathin SiO_2 layers, and Au(-Ni)/Al front finger electrodes were introduced by thermal evaporation. The area of all MIS solar cells is 0.2 cm^2.

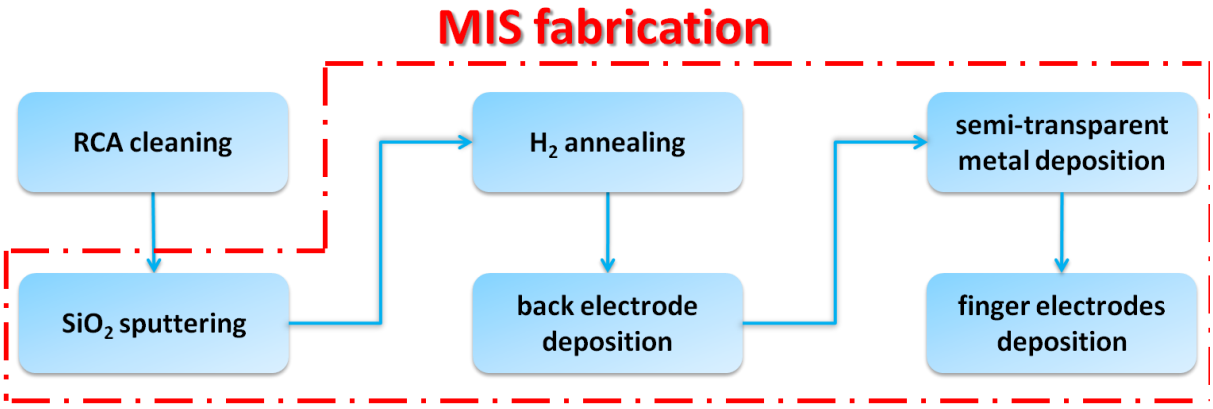

Fig. 2.6 The fabrication flow of MIS solar cells

2.4 The Fabrication of the Stacking Metal-Insulator-Semiconductor Solar Cell

The proposed stacking MIS solar cell is composed of an n-type MIS solar cell as the top cell and a p-type MIS solar cell as the bottom cell with a tunneling junction in between. The structure is shown in Fig. 2.7, and its fabrication procedures are illustrated in Fig. 2.8. First, an n-n^+ sample and a p-p^+ one were fabricated using ion implantation and rapid thermal annealing (Sec. 2.4.1). Then, an n-n^+-p^+-p sample was prepared by bonding the n-n^+ sample with the p-p^+ one (Sec. 2.4.2). After the bonding process, both sides of the n-n^+-p^+-p sample were thinned by wet etching (Sec. 2.4.3). Since the n-n^+-p^+-p sample is too fragile for thickness measurement, the thicknesses are first roughly estimated by reference Si substrates using scanning electron microscopy. The thickness of the n-type Si substrate is about 90 μm and that of the p-type Si substrate is around 400 μm. The thickness of the n-type Si is designed to be much thinner than that of the p-type Si for current matching consideration. The optimal thickness for the n-type Si is about 4 μm. Finally, the sample was processed based on the optimized conditions obtained from the individual n-type and p-type MIS solar cells. The area of the stacking MIS solar cell is 0.2 cm^2.

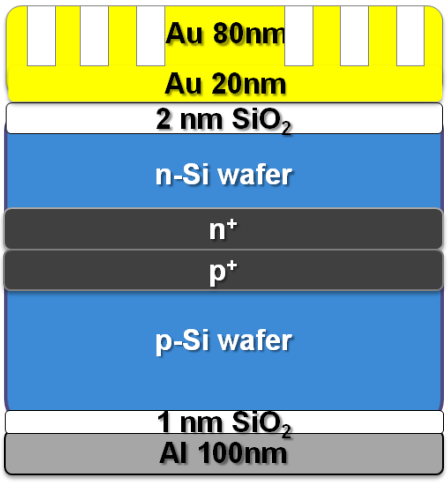

Fig. 2.7 The structure of the stacking MIS solar cell.

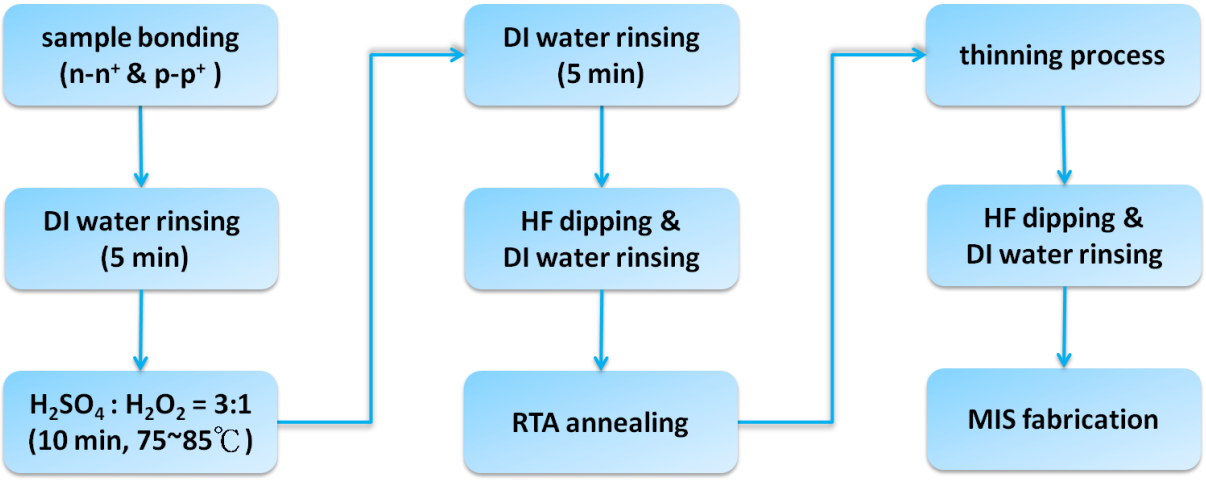

Fig. 2.8 The fabrication flow of the stacking MIS solar cell.

2.4.1 The Fabrication of the n-n$^+$ and p-p$^+$ Samples

The stacking MIS solar cell needs a tunneling junction which photoexcited majority carriers in the top cell can recombine with those in the bottom cell. Before forming the tunneling junction, an n-n$^+$ sample and a p-p$^+$ one are required. Following is the fabrication procedures of them, as shown in Fig. 2.9. First, n-type and p-type Si substrates were cleaned through the standard RCA process. Then the polished surface of the n-type Si substrate was doped with arsenic ions by ion implantation with doses of $5x10^{15}$ cm^{-2}. The energy of ion implantation is 80 KeV and 20 KeV in sequence. Similarly, the polished surface of the p-type Si substrate was implanted with 24 KeV boron ions with a dose of $5x10^{15}$ cm^{-2} and then with 10 KeV boron ions with a dose of $5x10^{15}$ cm^{-2}. The activation of the implanted ions, by rapid thermal annealing at 1050℃ for 10s, was executed after the bonding process.

2.4.2 The Bonding Process

After obtaining the implanted samples, the n-n$^+$-p$^+$-p sample with a tunneling junction can be generated through a bonding process. The bonding procedures are disclosed below, as shown in Fig. 2.10. First, the implanted samples were dipped with a diluted HF solution and

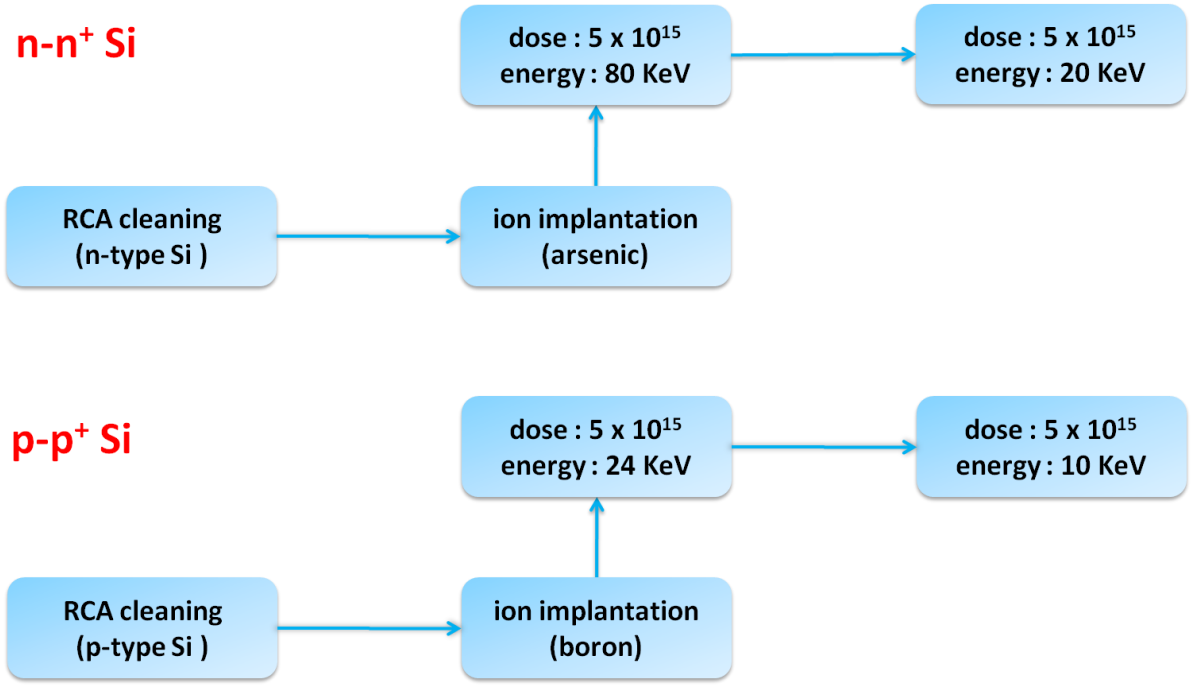

Fig. 2.9 The fabrication flows of the n-n^+ and p-p^+ samples.

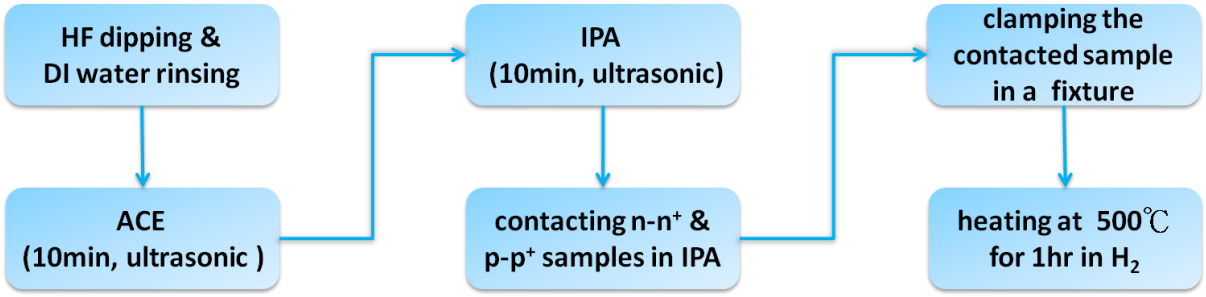

Fig. 2.10 The flow of the bonding process.

were rinsed with deionized (DI) water. Then, the samples were cleaned with aceton (ACE) and isopropanol (IPA) solutions in an ultrasonic cleaning tank in sequence. After the cleaning processes, the cleaned n-type sample was contacted directly with the cleaned p-type one in an IPA solution at room temperature, and then the contacted sample was fixed in the fixtures. Finally, the fixture was put into a heating chamber, and was heated at 500℃ for 1 hr in hydrogen atmosphere. The hydrogen can prevent the bonding interface from oxidation, which attributes to impurities in the chamber, during the heating process.

2.4.3 The Thinning Process

For balancing the photon fluxes of the top and bottom cells, the thickness of the top cell must be thinned toward the optimized thickness (4 μm). The thinning process, as illustrated in Fig. 2.11, is revealed as follows. First, the well bonded sample was immersed in a etchant ($HF : CH_3COOH : HNO_3 = 6 : 7 : 20$) for 12 to 13 minutes. Finally, the etched sample was rinsed using DI water.

2.5 Material And Interface Analyses

2.5.1 High Resolution X-Ray Photoelectron Spectrometer

High resolution X-ray photoelectron spectroscopy (HRXPS) can help deduce the chemical composition of materials on the surfaces. When monoenergetic soft X-rays with photon energy hv irradiated by solids in vacuum illuminate on the surface of a material, photoelectrons with kinetic energy E_{kin} will emit out of the surface and are collected by the analyzer, as shown in Fig. 2.12. The spectrum is a plot of the number of emitted photoelectrons per energy interval versus their binding energy E_b, as expressed by Eq. (2.1).

$$E_b = hv - E_{kin} \tag{2.1}$$

The composition of the Alq_3/Al interfaces and the atomic concentration of the Alq_3 thin films were analyzed by measuring the Al-2p, and N-1s and O-1s photoelectron spectra, respectively, using HRXPS (ULVAC-PHI Quantera SXM) after Ar^+ milling on the sample surfaces. The HRXPS equips with a monochromatic Al Kα radiation X-ray source and

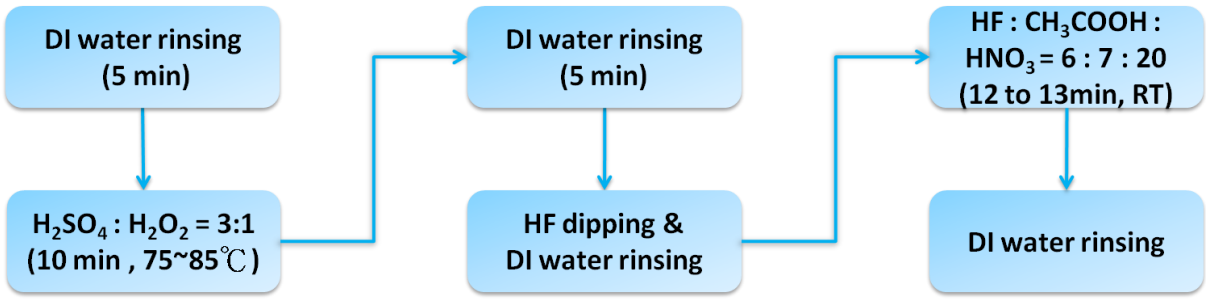

Fig. 2.11 The flow of the thinning process of the bonded n-n^+-p^+-p sample.

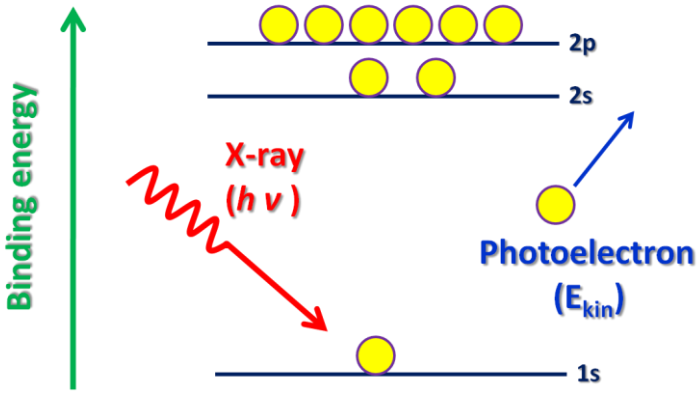

Fig. 2.12 The X-ray photoelectron process of HRXPS.

a hemispherical energy analyzer. The power of the X-ray source is 25 W at 15 kV accelerating voltage, and the analyzed area of the samples is about 100 μm^2.

2.5.2 Grazing Incident X-Ray Diffraction

X-ray diffraction is a nondestructive approach to identify the crystallization structures of solids. For a sample with regular arrays of atoms, the atoms will scatter the waves when X-ray waves illuminate into the sample, as shown in Fig. 2.13. Diffraction patterns can be obtained as long as the phases of not less than two scattering waves superposition to meet Bragg's law, as expressed by Eq. (2.2), where d is the spacing between diffracting planes, θ is the incident angle, *n* is any integer, and λ is the wavelength of the X- ray beam. According to a plot of diffraction intensity verse diffraction angles, the crystallization structures of the sample can be identified.

$$2d \sin\theta = n\lambda \tag{2.2}$$

The structural information of the Alq_3 thin films deposited at different deposition rates was analyzed via XRD (Rigaku, RU-H3R) using a grazing incident X-ray diffraction (GIXRD) mode. The incident X-ray was fixed at a tiny angle with respect to the surfaces of the Alq_3 thin films, and the detector did 2θ scan.

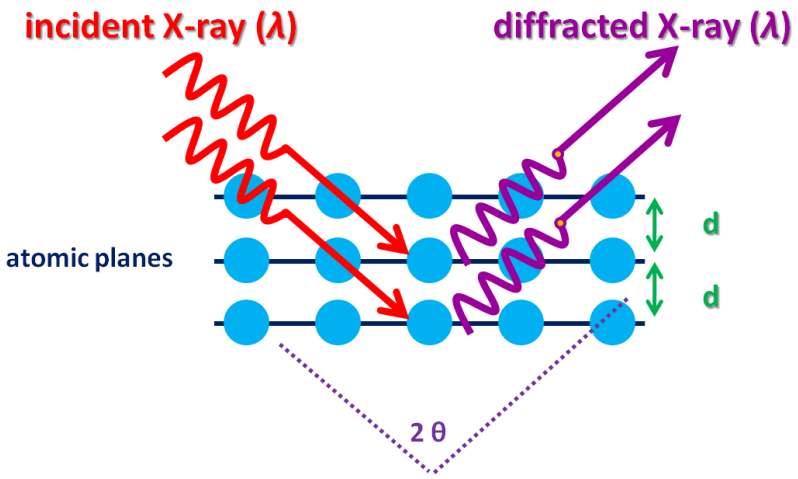

Fig. 2.13 The X-ray diffraction process.

2.5.3 Atomic Force Microscope

Atomic force microscope (AFM) is an apparatus whose primary component is an extremely sharp tip mounted or integrated on the end of an extreme small cantilever spring which is moved by a mechanical scanner over the surface of a sample, as shown in Fig. 2.14(a). AFM can provide the topography of bare and monolayer coated solids. When the tip is moved close to a sample surface, forces between the tip and the sample surface can result in a deflection of the cantilever owing to Hooke's law. According to the deflection detected by a laser beam, the morphology of the sample surface can be obtained. For conventional AFM, two operation modes are available, the contact mode (the tip onto the sample surface, repulsive force) and the tapping mode (the tip in close vicinity of the sample surface, attractive force), as shown in Fig. 2.14(b).

The surface morphology of the Alq_3 thin films on the Si substrates and that of the MoO_x layers on the Alq_3 thin films were obtained by using AFM (DI-Veeco Instruments, D3100). We chose the tapping mode to scan the sample surfaces because of the softness of organic thin films.

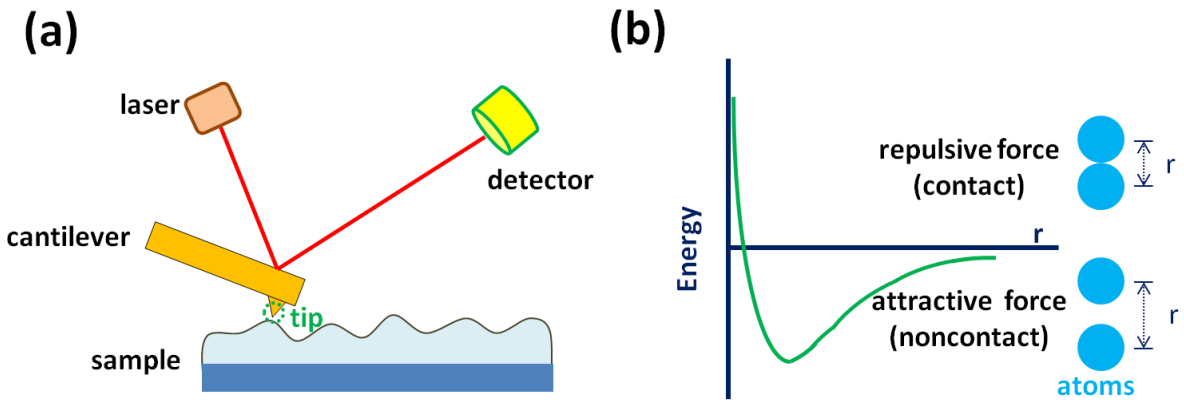

Fig. 2.14 (a) The operation of AFM. (b) The forces between the AFM tip and the sample surface.

2.5.4 Transmitted Infrared Imaging System

The bonding interface of the stacking MIS solar cell plays an important role in the performance of the stacking MIS solar cell because the interface is where the majority carriers of the top cell recombine with those of the bottom cell. If the interface cannot be a good tunneling junction and/or is not well bonded, the V_{oc} enhancement of the stacking MIS solar cell will be blocked. In order to observe the interface, a transmitted infrared (IR) imaging system, which consists of a light bulb, a sample stage, a focus lens, an IR charge coupled device (CCD), and a screen, as shown in Fig. 2.15, was established.

The operation of the system is presented as follows. When photon fluxes, emitted from the light bulb, are incident into the bonded sample, photons with energy larger the bandgap of Si (1.124 eV) are absorbed by the bonded sample. The rest photons, whose energy less than 1.124 eV, are detected by the IR CCD. If any unbonded area (interface bubbles or voids) generates in the interface, fringe patterns, which result from the interference of the passing IR photons, can be observed on the screen.

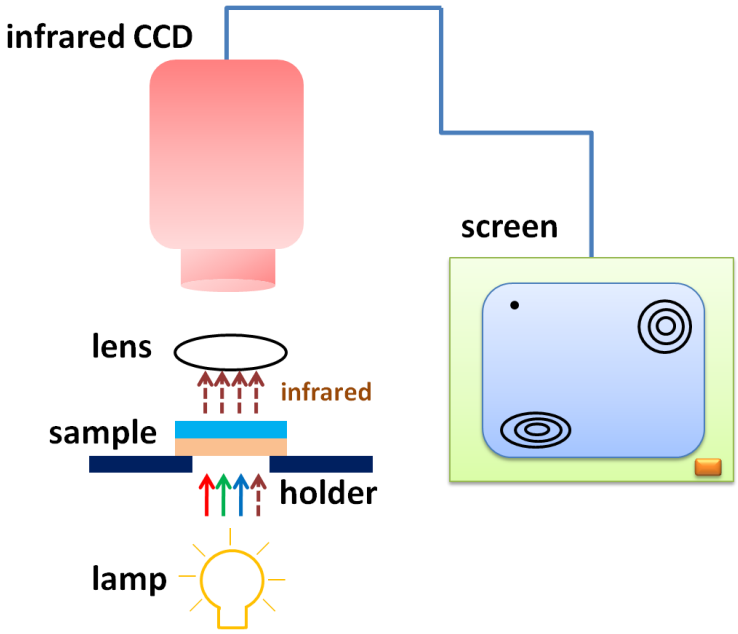

Fig. 2.15 The setup of the transmitted IR imaging system.

2.6 Device Characterization

2.6.1 Current-Voltage Measurement

The I–V curves of OBDs (the writing process, the erasing process, the reading process, the retention test, and the write-read-erase-read cycle) were measured in an ambient environment using a measurement system which is composed of a personal computer, a Hewlett Packard 4156A semiconductor parameter analyzer, a switching box, and a probe station. The writing bias, the erasing bias, and the reading bias are sweeping voltages and/or (quesi-)pulse voltages.

2.6.2 Capacitance-Voltage Measurement

A measurement system which includes a personal computer, an Agilent 4284A Precision LCR meter, a switching box, and a probe station was adopted to record the high frequency capacitance-voltage (C-V) curves of OBDs and MIS solar cells.

2.6.3 Photocurrent Measurement

The J-V curves of MIS solar cells were obtained using a solar simulator system which consists of a laptop, a Keithley 2400 source-measure unit, a probe station, and a solar simulator with an Air Mass 1.5 source with a power of 100 mW/cm^2 (Oriel Class A). The illuminated light intensity was calibrated by a polycrystalline silicon solar cell certified by the National Renewable Energy Laboratory (NREL).

Chapter 3

Organic Bistable Devices With Interfacial Oxide Layers

3.1 Organic Bistable Devices With Interfacial Layers

Interface layers between the (metal) electrodes and organic layers of OBDs play an important role in the characteristics of organic electronics. [161] For understanding the interface effects on OBDs, some have paid attention on the interface engineering of OBDs. [35], [161]-[166] Kondo et al. demonstrate that the ON/OFF ratio of OBDs is significantly enhanced by modifying the ITO electrodes (introducing Ag nanodots between the organic layer and the indium tin oxide surface). The Ag nanodots act as trapping sites, reducing the current of the OFF state. [162] Cho et al. form a self-assembled monolayer (4-nitrophenyl dichloride phosphate) on the hydroxyl-terminated Al electrode surface with native oxide to enhance switching reproducibility with an improved current level distribution. [163] Moreover, when an aluminum electrode is deliberately oxidized or unintentionally is passivated with native oxide, some organic devices display written, reproducible resistance switching. [35], [164]-[166] Cölle et al. show that the switching mechanism of OBDs with a (metal) electrode/organic/(metal) electrode structure (at least one electrode using Al) is due to the oxide layer on the Al electrode, and carriers transport through filaments, whereas the organic materials have only minor influences on it. [35] Verbakel et al. realize reproducible OBDs by deliberately adding thin sputtering Al_2O_3 layers to the surfaces of the bottom electrodes of nominal electron-only, hole-only, and bipolar organic diodes. They attribute the operation of the OBDs to the soft breakdown of the sputtering Al_2O_3 layers. In addition, the

OBDs exhibit negative differential resistance (NDR) and local maximum currents in the I-V curves, which are dependent on the thickness of the sputtering Al_2O_3 layers. In their case, the polymers play a role as a current limiting series resistance. [165] Cho et al. study OBDs with a interfacial AlO_x layer, using an O_2 plasma treatment method, formed on the surface of the bottom Al electrode. The OBDs give higher ON/OFF ratios than those without the interfacial AlO_x layer because of the relatively small resistance at the OFF states. Nevertheless, the duration of the O_2 plasma treatment makes a great influence on the threshold voltage distribution and the switching reproducibility. [166]

In this chapter, an OBD with Alq_3/Al deposited on an n-type Si substrate, as shown in Fig. 2.1, is fabricated and investigated. The OBD shows distinct bistability with an ON/OFF current ratio over 10^6 and a wide reading voltage range for differentiating between ‘‘ON” and ‘‘OFF” states. The formation of electrically bistable states is the result of electrons being trapped in the defects at the Alq_3/Al interface during electrical field stressing. This study also provides a simple approach, varying the deposition rate of the Alq_3 thin film, using which the electrical characteristics of the OBD, e.g., threshold voltage, can be tuned or controlled. HRXPS, AFM, and GIXRD measurements are performed to help us understand the properties of Alq_3 thin films and the Alq_3/Al interface and explain the experimental results obtained. Besides, the simple structure of the OBD indicates that the OBD can be easily embedded into the well-developed semiconductor fabrication processes.

3.2 Results And Discussions

Figure 3.1 shows typical I-V curves of the fabricated n-type Si/Alq_3/Al structure. As can be seen, this device exhibits two different conductance states at an identical applied voltage. The silicon electrode is kept at 0 V, and all bias conditions are applied on the aluminum electrode. At the first bias (the black square curve in Fig. 3.1), the voltage sweeps from 0 V to 10 V. Initially, the device exhibits a low conductance state (OFF state). However,

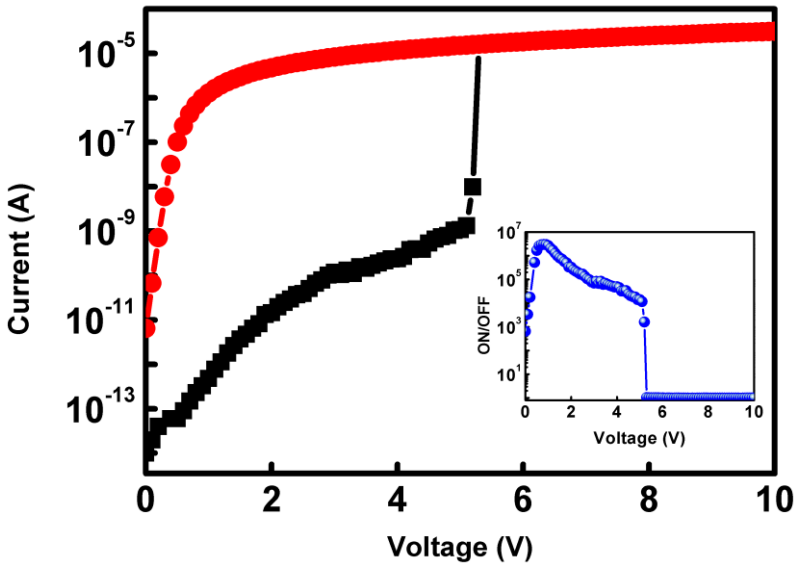

Fig. 3.1 The I-V curves of the OBD with the n-type Si/Alq_3/Al structure. The black square and red circle curves represent writing and reading biases, respectively. The inset shows the voltage-dependent ON/OFF current ratio curve.

with an increased bias, a transition from the low conductance state to a high conductance state (ON state) occurs at a threshold voltage of about 5 V, and then the device is maintained at the high conductance state. At the next bias (the red circle curve in Fig. 3.1), the device still holds at the high conductance state. Therefore, this device possesses the nature of bistablity. Furthermore, by applying a negative bias form 0 V to -10 V, the device can be switched from the high conductance state back to the low conductance state. The plot of ON/OFF current ratios as a function of reading bias is shown in the inset of Fig. 3.1. It is obvious that the device has a very wide reading voltage range with large ON/OFF current ratios which may reduce reading errors and increase the reliability of the device. For this reason, the tolerance of this device is large enough for external surrounding circuitry to adopt. The corresponding reading currents after ‘‘writing” and ‘‘erasing” for the first four cycles are shown in Fig. 3.2.

At the low voltage of the first bias, the current is very small because electrons are obstructed by a barrier formed between the Si substrate and Alq_3. Thus, only a few electrons are injected into the Alq_3 thin film. Then most of them are further trapped by the defects in the

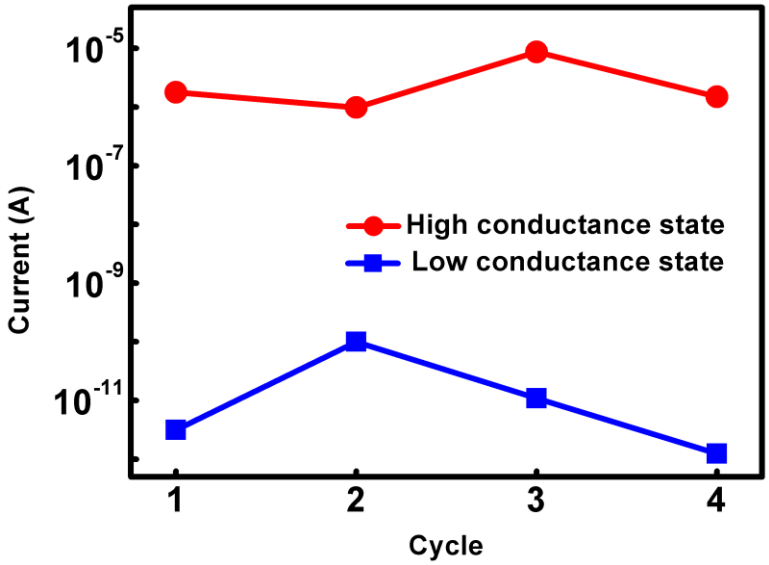

Fig. 3.2 The reading currents after "writing" and "erasing" of the OBD with the n-type Si/Alq_3/Al structure for the first four cycles.

Alq_3 thin film and at the Alq_3/Al interface. As a result, the device stays at the low conductance state. By applying a bias above the threshold, the barrier can be overcame, and this enables numerous electrons to be injected into the Alq_3 layer and the defects can be filled. Accordingly, electrons are transported easily into the Alq_3 thin film and drift unobstructedly towards the other end of the device. At the next bias, the device exhibits a resistance-like characteristic when the reading voltage is larger than the energy barrier between Si and Alq_3. That is, the ON state can be obtained for any reading voltage larger than the iso-type hetero-junction barrier between n-type silicon and Alq_3, which is about 0.65 eV estimated from Fig. 3.3.

Fig. 3.4 shows the C-V curve of the device. It can be seen from the curve that the device keeps at some capacitance value while the applied voltage is below the threshold. Then, the value changes into another lower capacitance value when the voltage exceeds its threshold. The variation of capacitance could be ascribed to the defects in the Alq_3 thin film and at the Alq_3/Al interface. At the initial stage of the applied voltage, few electrons are trapped by the defects in the low electrical field. Then, more and more electrons are trapped by the defects as

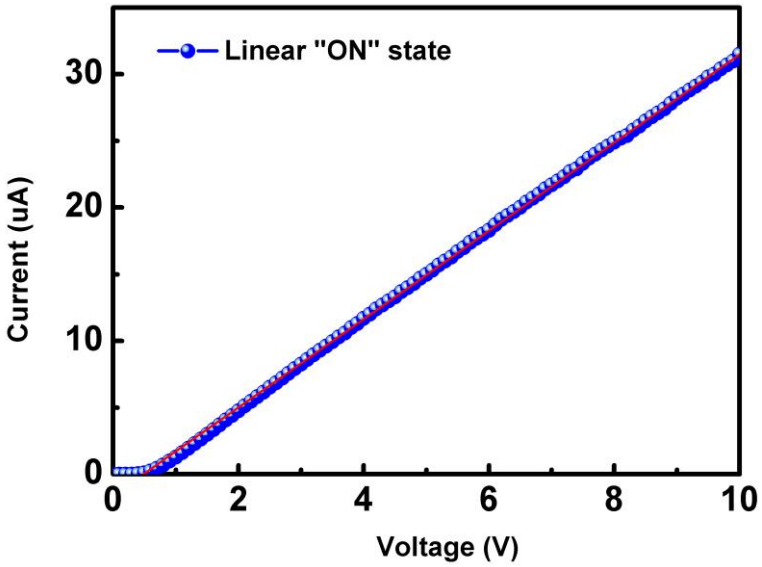

Fig. 3.3 The linear I-V curve of the OBD with the n-type Si/Alq_3/Al structure at the high conductance.

the voltage increases. While the applied voltage is near the threshold, the defects are filled sufficiently to make the device possess a metallike property; consequently, the capacitance is converted into a lower value. In addition, the I-V curve of the n-type Si/Alq_3 structure with one small Al drop as the top electrode does not exhibit bistability but rather diode behavior. This indicates that the interface property between the Al electrode and the Alq_3 thin film plays an important role in bistability.

Mason et. al. report that a significant chemical reaction occurs at the Alq_3/Al interface when Al is thermally deposited on the Alq_3 thin film [167]. The resulting product, supportively consisting of Al-O interactions, serves as interface traps and makes carriers be poorly injected through the Alq_3/Al interface. Fig. 3.5 shows the XPS curves of the Al electrode and the Alq_3/Al interface of the reported device, which clearly confirm the existence of an Al-O compound at the Alq_3/Al interface of the device. Therefore, we can conclude that trapping charges at the interface between Alq_3 and Al primarily controls the switching mechanism.

The electrical behavior of the device can be modified by varying the deposition rate of

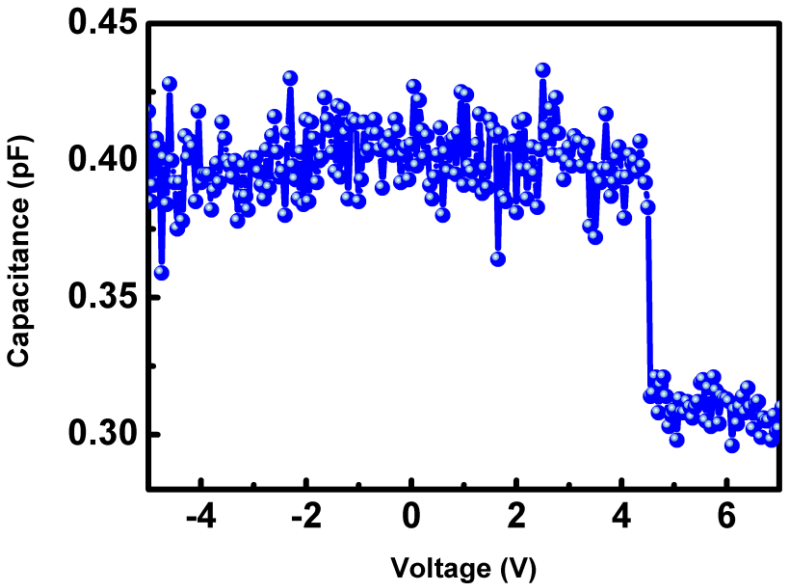

Fig. 3.4 The C-V curve of the OBD with the n-type Si/Alq_3/Al structure at a frequency of 1 MHz. The Si electrode is kept at 0 V, and the bias on the Al electrode is swept form -5 V to 7 V.

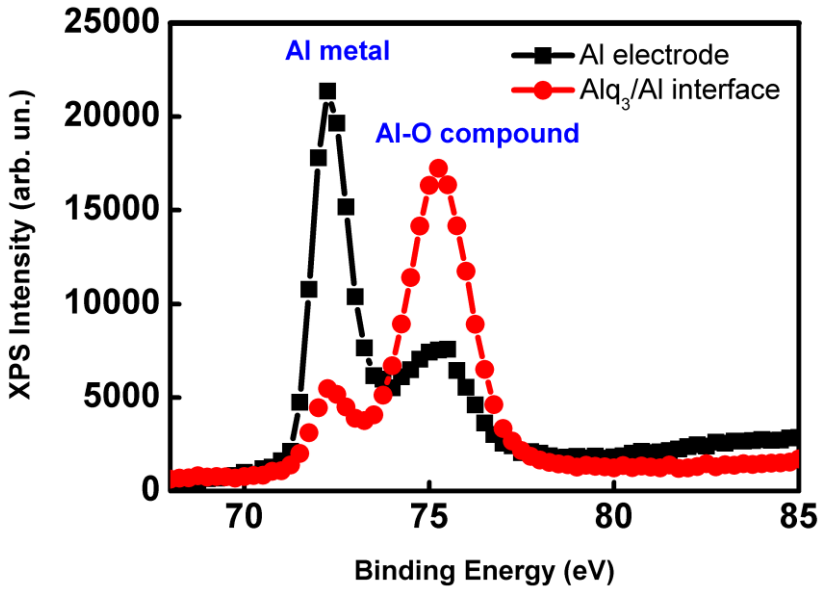

Fig. 3.5 The XPS curves of the Al electrode and Alq_3/Al interface of the OBD with the n-type Si/Alq_3/Al structure.

the Alq_3 thin film. Fig. 3.6(a) show the threshold voltages (the black square curve) and ON/OFF current ratios of OBDs (the red circle curve) using the same structure whose Alq_3 thin films were deposited at different deposition rates: both parameters decrease with an

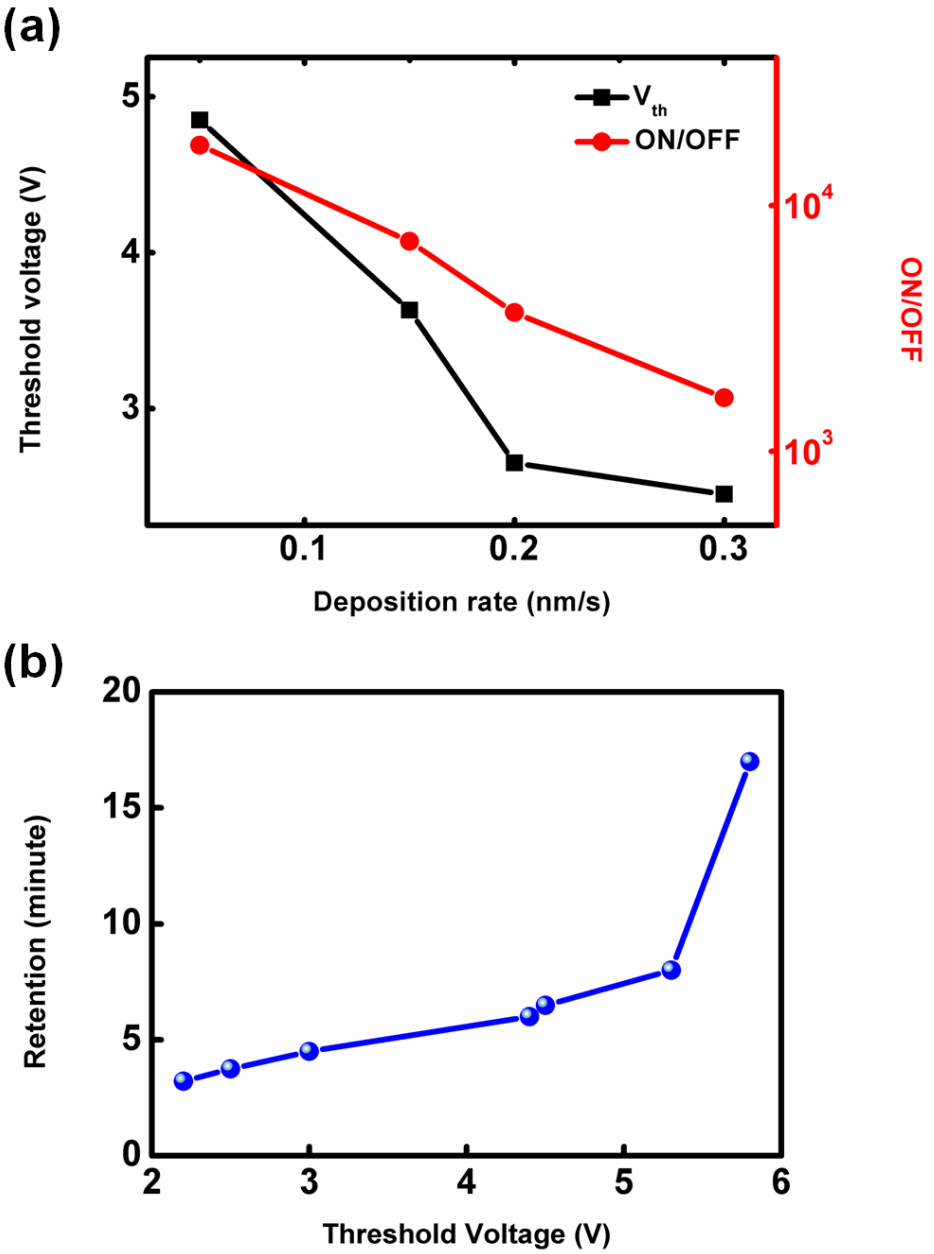

Fig. 3.6 The electrical properties of OBDs with the n-type Si/Alq_3/Al structure whose Alq_3 thin films are deposited at different deposition rates: (a) the black square and red circle curves represent deposition-rate dependent threshold voltage, and deposition-rate dependent ON/OFF current ratios, respectively, and (b) threshold-voltage dependent retention time. Data points shown in (a) are average values measured from the OBDs.

increase in the deposition rate. In addition, as can be seen in Fig. 3.6(b), the retention time is dependent on the threshold voltages of the OBDs. Since the threshold voltages can be tuned by adjusting the deposition rates of the Alq_3 thin films, the retention time can be extended by

reducing the deposition rates of the Alq_3 thin films.

Previous reports on the morphology of the Alq_3 thin films indicate that roughness decreases with the deposition rate [168], [169]. That is to say, the effective contact surface area between Alq_3 and Al can be adjusted by regulating the deposition rate of Alq_3. For that reason, a higher deposition rate introduces a relatively small effective contact area at the Alq_3/Al interface. Fig. 3.7 shows the AFM images of the Alq_3 thin films deposited at 0.05 nm/s, 0.15 nm/s, 0.2 nm/s, and 0.3 nm/s. The corresponding surface roughness means are 0.38 nm, 0.35 nm, 0.31 nm, and 0.17 nm. These confirm that the deposition rates of the Alq_3 thin films are a major factor in the adjustment of the effective contact surface areas between Alq_3 and Al, which may affect the amount of the interface defects of the corresponding OBDs. It suggests that the relative amount of the defects at the Alq_3/Al interfaces can be modified by controlling the deposition rates of the Alq_3 thin films. Furthermore, measuring the

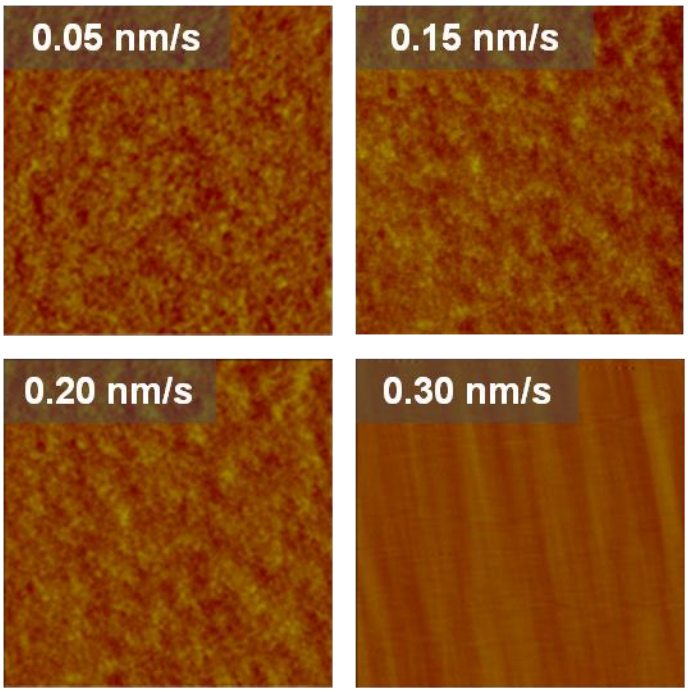

Fig. 3.7 The AFM images of the Alq_3 thin films deposited on n-type Si substrates at the four different deposition rates. Surface roughness means are 0.38 nm, 0.35 nm, 0.31 nm, and 0.17 nm for deposition rates at 0.05 nm/s, 0.15 nm/s, 0.2 nm/s, and 0.3 nm/s, respectively.

GIXRD curves of the Alq_3 thin films deposited at the four deposition rates, as shown in Fig. 3.8, we find that crystallization does not occur in all Alq_3 thin films. Consequently, the threshold voltages, ON/OFF current ratios, and retention time are not related to the crystallization quality of the Alq_3 thin films. They are closely related to the film roughness, as shown by the AFM images in Fig. 3.7.

It has been demonstrated that the atomic N/C ratios of the Alq_3 thin films changes with the deposition rates of the Alq_3 thin films. [168], [169] At a higher deposition rate (a higher temperature condition), the Alq_3 molecule structure disintegrates to release N-containing species due to the decomposition energy of Alq_3 being smaller than its sublimation energy. It has been also shown that the Alq_3 thin film deposited at a lower deposition rate contains a greater atomic concentration of nitrogen and a higher atomic N/C ratio. From XPS measurements, the corresponding concentrations of N and the atomic N/C ratios of the four Alq_3 thin films in this study are given in Table 2.1, which clearly indicates the same trend discussed above.

When electrons are injected into an Alq_3 thin film, they undergo a repulsive force generated by the negatively charged nitrogen atoms which is the result of the

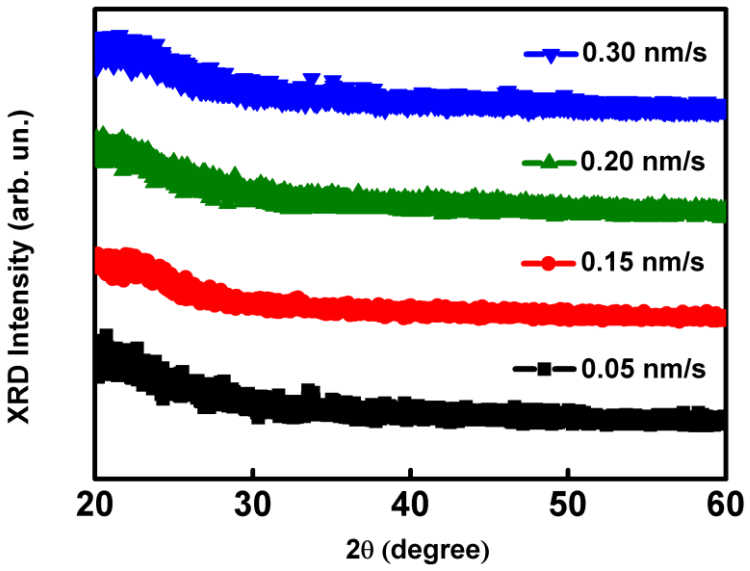

Fig. 3.8 The GIXRD curves of the Alq_3 thin films deposited at the four deposition rates.

electronegativity of a nitrogen atom being larger than that of a carbon or oxygen atom for a neutral Alq_3 molecule [170]. Hence, electrons in an Alq_3 thin film with a smaller N/C ratio experience less repulsive force [169]. In other words, an increase in the deposition rate of the Alq_3 thin film can extend the hopping distance of the electrons in the Alq_3 thin film and can raise the hopping frequency.

From above discussions, two findings can be made to explain the results obtained in Fig. 3.6(a). First, it is obvious that the threshold voltages decrease with the increasing deposition rates because of a smaller amount of defects at the Alq_3/Al interface at a higher deposition rate. Second, the same relationship for the ON/OFF current ratios is because a smaller amount of nitrogen atoms are available to prevent the electrons from hopping in the Alq_3 thin film, hence increase the low conductance state current and decrease the ON/OFF current ratio at a higher deposition rate.

Because the distribution of the defects at the interface corresponds to the trapping energy [171], we may simply classify the defects at the Alq_3/Al interface into two groups: low trapping energy defects (E_{low}) and high trapping energy defects (E_{high}), as shown in Fig. 3.9.

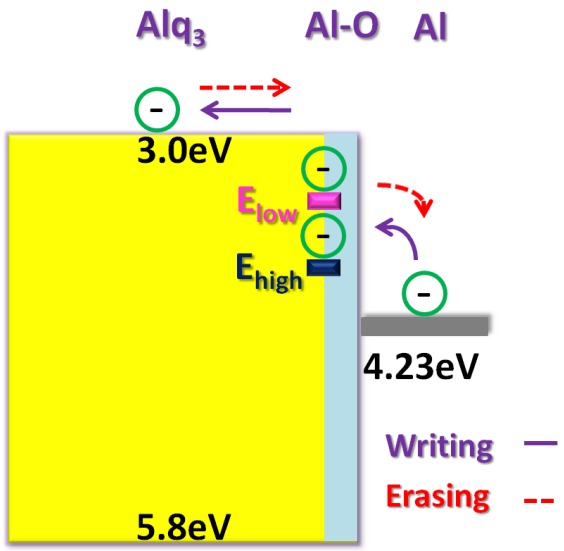

Fig. 3.9 The illustration of the defect states in the Al-O compound layer: E_{low} and E_{high}.

In order to address those two groups, the I-V curves of the OBD, whose Alq_3 thin film deposited at 0.05nm/s, are measured at three different temperatures (room temperature, 50℃, and 90℃), as shown in Fig. 3.10. At room temperature and 50℃, the device is operated normally, but its electrical characteristic changes, e.g. the smaller threshold voltage, at 50℃. This indicates that E_{low} are compensated effectively at 50℃. As a result, lower threshold is observed. As the temperature increases to 90℃, the device reveals a diode property instead of bistable behavior. This means that E_{low} and E_{high} are both compensated. The measured temperature-dependent results can be evidence that there are two types of defects and that the bistability of the reported device arises from these defect states.

A higher deposition rate introduces a smoother Alq_3 surface, and may produce less E_{high} at the Alq_3/Al interface. Also, the corresponding OBD, which has low threshold voltage and the smoother Alq_3 surface, exhibits shorter retention time probably because of less E_{high}. In other words, after the corresponding OBD being switched into the high conductance state, most trapped charges are in the E_{low}, and they are easily released at the Alq_3/Al interface due to the lower confinement barrier. As a result, the trapped charges cannot be kept longer in

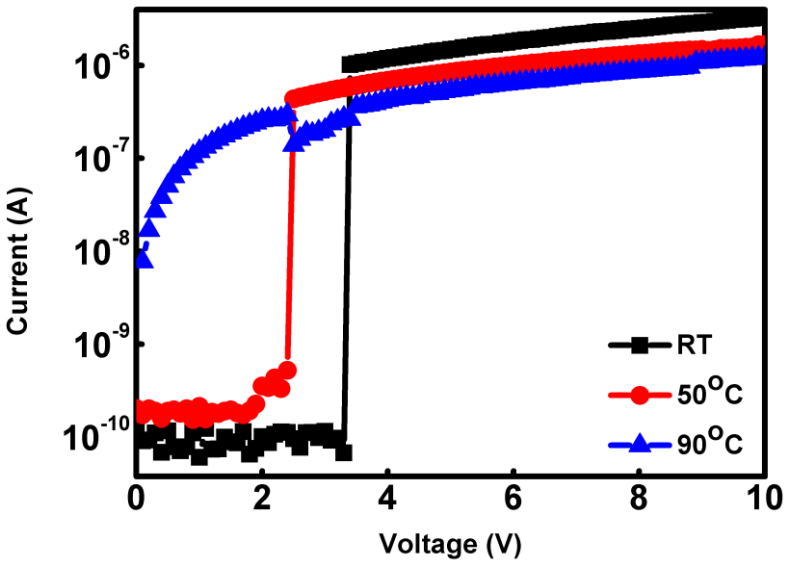

Fig. 3.10 The temperature-dependent I-V curves of the OBD whose Alq_3 thin film deposited at 0.05nm/s.

the corresponding OBD so it has shorter retention time, as shown in Fig. 3.6(b).

3.3 Summary

The I-V characteristics of the OBD, n-type Si/Alq_3/Al, are investigated. The bistability results from the defects of the Al-O compound layer at the Alq_3/Al interface. The electrical characteristics of the OBD can be optimized and tuned according to our needs for different situations based on the trends obtained in these experiments. Of course some tradeoffs must be made. Owing to its simple structure, the OBD can be embedded into the conventional silicon-based fabrication processes. Furthermore, the OBD has great potential for high-density data storage, low-cost memory applications in future nanoelectronics.

Chapter 4

Organic Bistable Devices Using Metal Oxide Nanocluster Layers

4.1 Organic Bistable Devices Using Nanostructured Materials

In organic memory, many published results have focused on ORM with nanostructured materials. [7], [26], [62]-[64], [67], [74], [172]-[178] Because of the distinct properties of the nanostructured materials, ORM with high density, large ON/OFF ratios, and other superior performances will be obtained in the near future. The nanostructured materials can consist of a nanocluster/organic-metal composite layer fabricated by a thermal evaporation method [26], [62], [63], [70] (e.g., Al cores covered with Al oxide shells, [26] and Ag islands in TPD, [70]). The nanostructured materials can also be composed of a nanocomposite of polymer-Au NPs fabricated by chemical synthesis. [7], [64]-[67] (e.g., Au NPs capped with 2-naphthalenthiol, [67] Au NPs capped with dodecanethiol [64]-[67]). In addition, metal NPs, [62], [175] oxide NPs, [74], [172], [117], [178] C_{60} NPs, [173], [174] and core/shell type CdSe/ZnS NPs [176] have been introduced to be the nanostructured materials.

MoO_x has been extensively applied in organic electronics (e.g., as a doping layer to raise conductivity, [179] as a buffer layer to increase carrier injection [180] or carrier collection, [181] as an intermediate layer to protect underlayers, [182] and as a capping layer to enhance light coupling [181]). Such wide applications attribute to the characteristics of the MoO_x thin films: high work function, high conductivity for holes, and high transparency.

In this chapter, we use a nanostructured MoO_x layer as the charge storage layer of an OBD. The OBD consists of a p^+-Si/Alq_3/nanostructured MoO_x/Alq_3/Al structure, as shown in Fig.

2.4. The OBD exhibits a high ON/OFF ratio up to 10^5, long retention time over 4000 s, and a rewritable/reerasable feature. The formation of the bistable switching of the OBD is ascribed to the charge trapping effect of the nanostructured MoO_x layer. Moreover, the I-V characteristics of the OBD are quite different from those of an OBD using a MoO_x NPs layer. [74] No NDR is observed in the I-V curves of our OBD. This phenomenon probably results from the dissimilar surface morphology of the MoO_x layer deposited on the Alq_3 thin film. Because of both the simple structure of our OBD and the merits of Alq_3 (e.g., low cost, easiness of preparation, and high stability), the complexity of fabrication and the production cost have potential to greatly reduce. Furthermore, our OBD can be easily embedded into the well developed semiconductor fabrication processes.

4.2 Results And Discussions

The I-V curves of the OBD with the p^+-Si/Alq_3/nanostructured MoO_x/Alq_3/Al structure are shown in Fig. 4.1(a). At first sweeping bias (the olive open square curve), a sweeping bias from 0 to 10 V is applied to the OBD with 100 mA current compliance. Initially, the OBD is in a low conductance state which has a current level of 10^{-10}-10^{-5} A. An abrupt increase in the current level is observed when the applied voltage is about 3.5 V. Then, the OBD holds at a high conductance state when the applied bias sweeps to higher voltage. It is clear that the OBD undergoes an electrical transition from an OFF state to an ON state. At next sweeping bias, the OBD still maintains at the high conductance state (the red open circle curve). Obviously, the OBD clearly exhibits two different conductance states with an ON/OFF current ratio up to 10^5. That is to say, the OBD possesses the nature of bistability. In addition, by applying a reversed sweeping bias form 0 to -10 V (the blue open triangle curve), there is a striking decrease in the current level when the applied voltage is about -5 V. In other words, the OBD is switched from the high conductance state to the low conductance state. The OBD can be switched to the high conductance state again when a following sweeping bias from 0 to

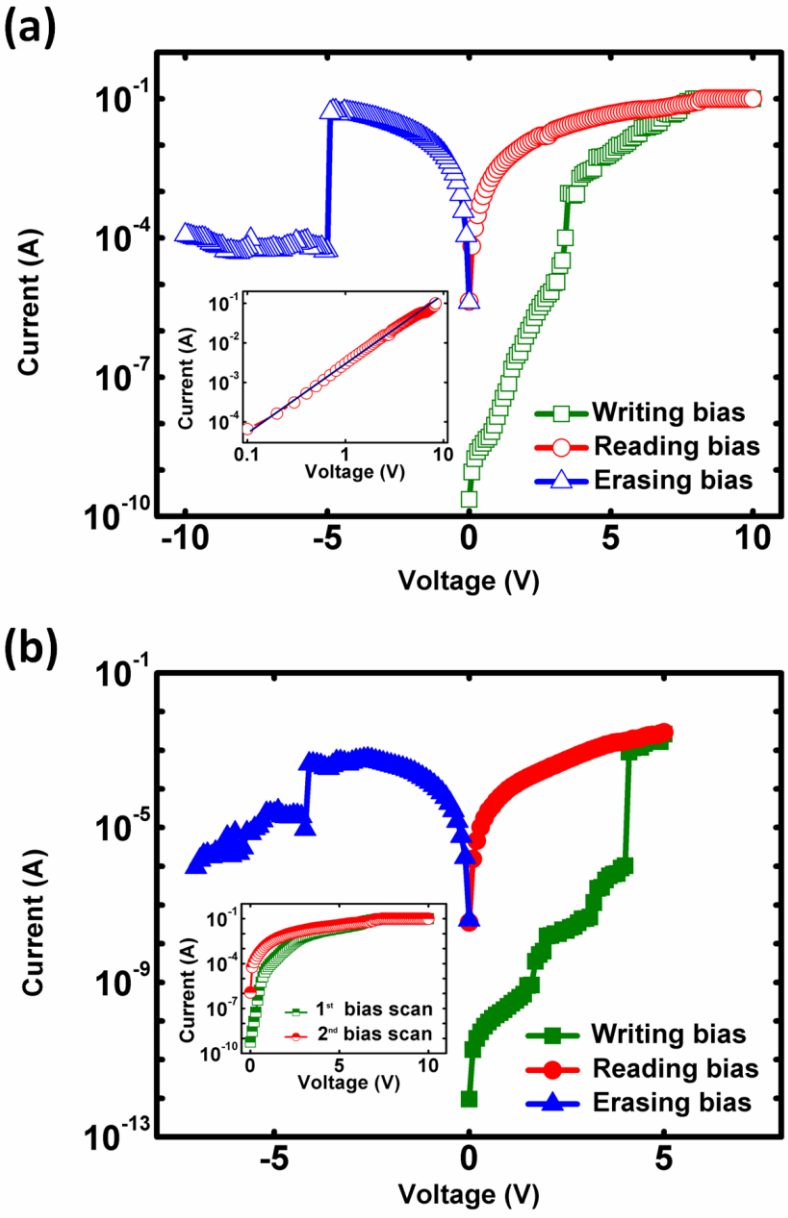

Fig. 4.1 (a) The I-V curves of the OBD with the p^+-Si/Alq_3/nanostructured MoO_x /Alq_3/Al structure. The olive open squares, the red open circles, and the blue open triangles represent the writing, reading, and erasing sweeping biases, respectively. Inset: fitting of the I-V curve of the high conductance state in a log-log scale. (b) The I-V curves of an OBD with a p^+-Si/Alq_3/nanostructured MoO_x/Alq_3/Ag structure. The olive solid squares, the red solid circles, and the blue solid triangles represent the writing, reading, and erasing sweeping biases, respectively. Inset: The I-V curves of an OBD with a p^+-Si/Alq_3/Ag structure. The green half solid squares and magenta half solid circles are the first and second bias scans, respectively.

10 V is applied. These results suggests that a sweeping bias form 0 to 10 V and a reversed polarity sweeping bias form 0 to -10 V serve as "writing" and "erasing" processes, respectively. Thus, the OBD holds the essences of a memory: bistability and rewritability.

The bistable switching of the OBD is referred to the nanostructured MoO_x layer sandwiched between the Alq_3 thin films. But some published results suggested that an Al-O compound near an Al electrode(s) is responsible for the resistance switching of OBDs with an Al electrode(s). [35], [165], [183] As can be seen in Fig. 4.2, an Al-O compound is generated at the interface between the Al and Alq_3 thin films. Namely, the bistable switching of the OBD could be relative to the Al-O compound. To verify this, we use Ag to replace Al as the top electrode. The bistability is again recognized from the I-V curves of an OBD with a p^+-Si/Alq_3/nanostructured MoO_x/Alq_3/Ag structure, as shown in Fig. 4.1(b). For comparison, the I-V curves of an OBD composed of a p^+-Si/100 nm Alq_3/Ag structure are shown in the inset of Fig. 4.1(b). No hysteresis as obtained in the I-V curves of the OBDs with the nanostructured MoO_x layer is observed. Therefore, we can conclude that the nanostructured MoO_x layer dominates the bistability of the OBD with the p^+-Si/Alq_3/nanostructured

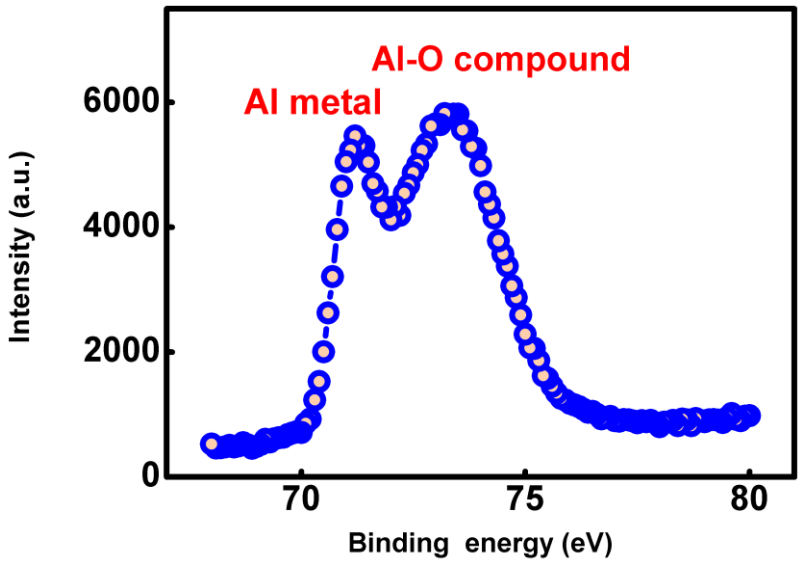

Fig. 4.2 The Al (2p) XPS curve of the Alq_3/Al interface of the OBD with the p^+-Si/Alq_3/nanostructured MoO_x/Alq_3/Al structure

$MoO_x/Alq_3/Al$ structure.

Figure 4.3(a) and (b) show the I-V curves of the p^+-Si/Alq_3/nanostructured $MoO_x/Alq_3/Al$ structures with 3-nm-thick and 8-nm-thick MoO_x, respectively. Both of them exhibit resistive switching behavior as the OBD with 5 nm-thick MoO_x. Nevertheless, the device with 3-nm-thick MoO_x displays a large current in low conductance state because of less trap sites. For the device with 8-nm-thick MoO_x, both the currents of the ON state and OFF state are

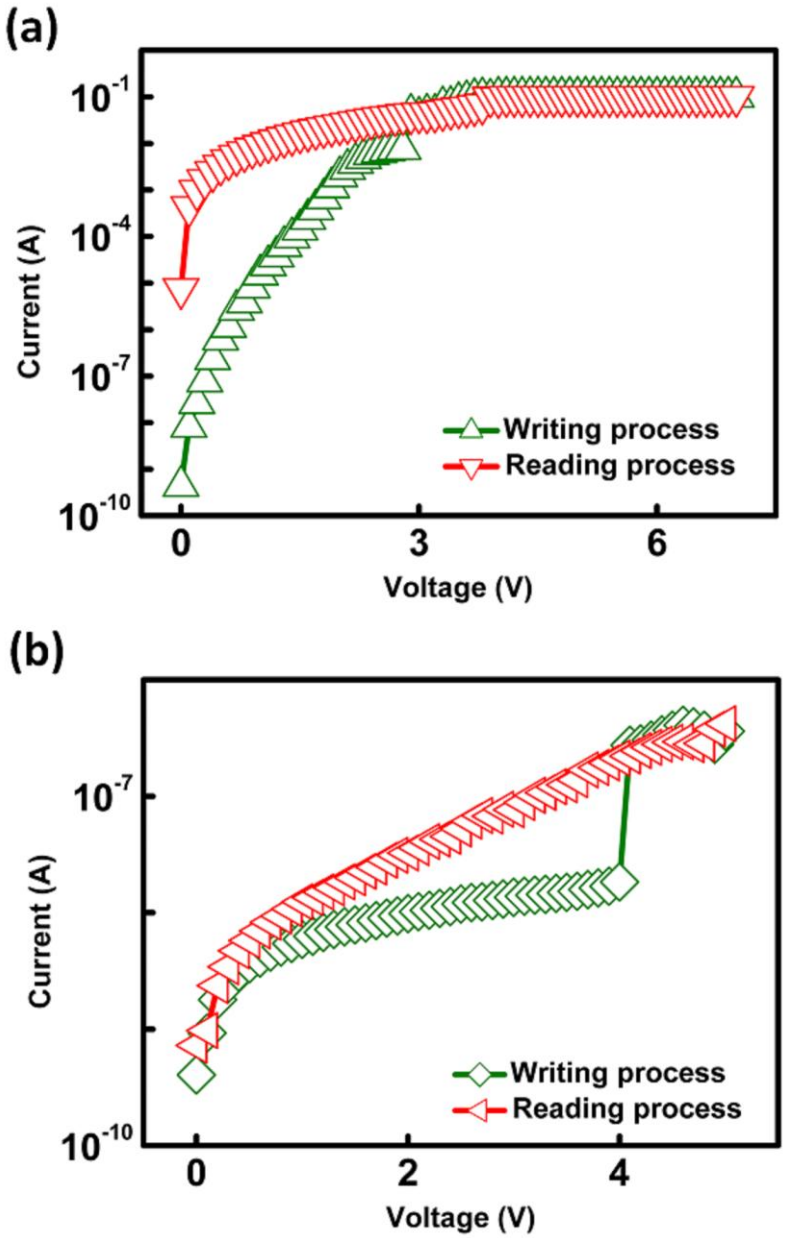

Fig. 4.3 The I-V curves of the p^+-Si/Alq_3/nanostructured $MoO_x/Alq_3/Al$ structure. (a) With 3-nm-thick MoO_x (b) With 8-nm-thick MoO_x.

suppressed as a result of much more trap sites. Note that both OBDs cannot reveal rewritibility as the device with 5 nm-thick MoO_x. Even though the actual cause is still unknown, we can deduce that the thickness of the nanostructured MoO_x layer influences the electrical identities of the p^+-Si /Alq_3/nanostructured MoO_x/Alq_3/Al structures, and that the optimized thickness is 5 nm in our case.

The ON/OFF state switching of the OBD shown in Fig. 4.1 primarily results from hole trapping/de-trapping provided by the nanostructured MoO_x layer, as shown in Fig. 4.4. At the low applied voltage of the first sweeping bias in Fig. 4.1(a), the current is very small. Most of holes injected from the p^+-Si into the OBD are trapped by charge trapping centers given by the nanostructured MoO_x layer. As a result, the OBD stays at the low conductance state. By applying a voltage above the threshold, numerous holes are injected into the OBD, and the charge trapping centers are filled sufficiently. Then, the nanostructured MoO_x layer is polarized, and the interfacial resistance of the nanostructured MoO_x layer is decreased. The OBD is switched to the high conductance state. On the contrary, while an adequate

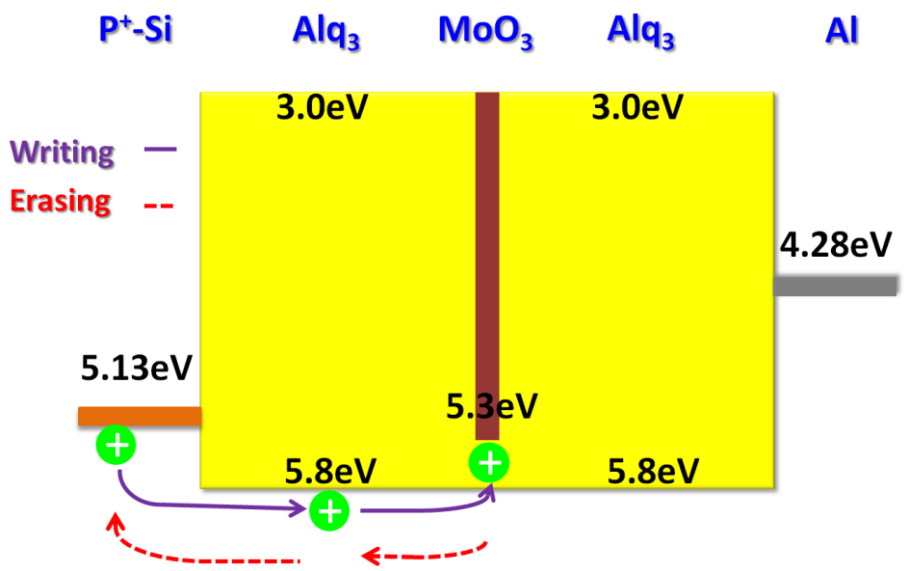

Fig. 4.4 The iIllustration of the writing and erasing processes of the OBD using a MoO_x nanoclusterlike layer.

reversed bias is applied on the OBD, the trapped holes in the charge trapping centers are released. The OBD is restored to the low conductance state.

By fitting the I-V curve of the high conductance state of the OBD in a log-log scale, linear relation between current and voltage is found, as shown in the inset of Fig. 4.1(a). Such relation indicates that carrier transportation at the high conductance state is influenced by space charges. In addition, NDR observed in the I-V curves of an OBD using a MoO_x nanoparticles layer [74] is not obtained in Fig. 4.1(a). Such dissimilarity probably originates from the surface morphology of the MoO_x layer. As shown in Fig. 4.5(a), the surface morphology of a 5-nm-thick MoO_x layer grown on the p^+-Si/Alq_3 is not a nanoparticle feature, but a nanoclusterlike feature. Polarization resulted from the charge trapping of the MoO_x nanoclusterlike layer is more random than that of the MoO_x nanoparticles layer. This means that the effective polarization effect on the carrier transportation of the MoO_x nanoclusterlike layer is weaker than that of the MoO_x nanoparticles layer, as shown in Fig. 4.5(b). Therefore, after switched from the low conductance state to the high conductance state, our OBD maintained at the high conductance state without NDR. These results also suggest that the

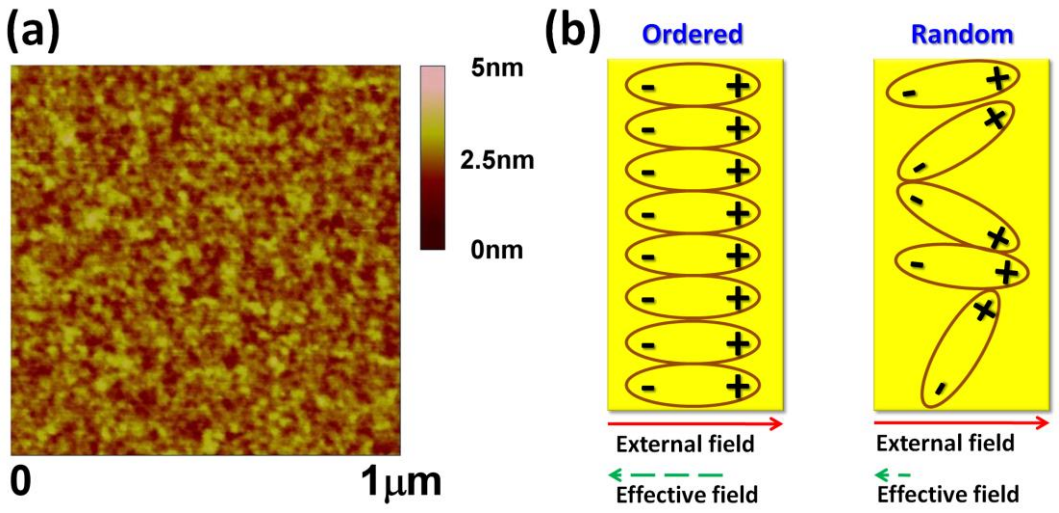

Fig. 4.5 (a) The surface morphology of the 5-nm-thick MoO_x layer deposited on the p^+-Si/Alq_3. (b) The illustration of the effective fields of ordered and random dipoles.

surface morphology of a nanostructured MoO_x layer plays an important role in the electrical characteristics of OBDs using nanostructured MoO_x.

Two important properties of our OBD are shown in Fig. 4.6, retention time and rewritable/re-erasable ability. The retention measurement of our OBD was carried out by

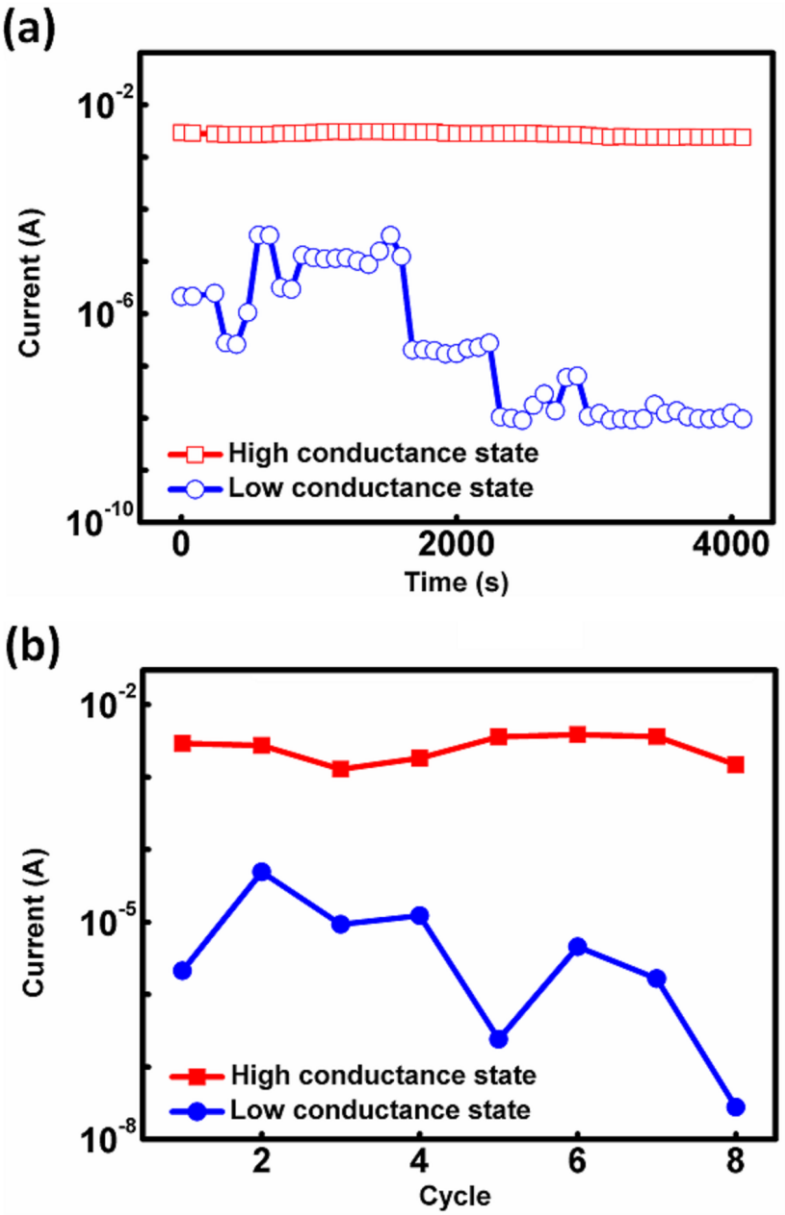

Fig. 4.6 (a) The retention measurement of the OBD with the p^+-Si/Alq_3/nanostructured MoO_x/Alq_3/Al structure. The red open squares and blue open circles correspond to the high and low conductance states. (b) The reading currents after writing and erasing of the OBD with the p^+-Si/Alq_3/nanostructured MoO_x/Alq_3/Al structure for the first eight cycles. The red solid squares and blue solid circles correspond to the high and low conductance states.

applying a bias at 1 V, as shown in Fig. 4.6(a). There is no appreciable change in the current of the high conductance state. Oppositely, current fluctuation occurs in the low conductance state. The current fluctuation of the low conductance state is because of the incomplete erasing of trapped charges after an erasing process. Nevertheless, the current of the low conductance state is getting smaller and more stable with time, and the ON/OFF current ratio becomes larger. Overall, a clear conductance difference between ON/OFF states can be recognized, and our device possesses long retention time over 4000 s. Fig. 4.6(b) shows the currents of the OBD at reading voltage after writing (high conductance state) and erasing (low conductance state). The reading voltage, writing sweeping bias, and erasing sweeping bias are 1 V, from 0 to 10 V, and from 0 to -10 V, respectively. The current of the high conductance state of each cycle is quite stable. However, the current fluctuation of the low conductance state of each cycle is again observed because of the incomplete erasing of trapped charges. In spite of the current fluctuation of the low conductance state, the ON/OFF current ratio of each cycle can still be easily distinguished.

4.3 Summary

The electrical properties of an OBD with a p^+-Si/Alq_3/nanostructured MoO_x/Alq_3/Al structure are studied. We show that the bistability of the OBD mainly attribute to the charge trapping effect of the MoO_x nanoclusterlike layer interposed between the Alq_3 thin films. The resistance switching without NDR is observed in the I-V curves of the OBD, which differs from those of an OBD with a MoO_x nanoparticles layer. According to the results in this chapter, we can figure out that the electrical characteristics of OBDs using nanostructured MoO_x layers are largely affected by the surface morphology of the nanostructured MoO_x layers.

Chapter 5

High Open Circuit Voltage Metal-Insulator-Semiconductor Solar Cells

5.1 A Stacking Metal-Insulator-Semiconductor Solar Cell

Extending photovoltaic applications plays a prominent role in the following evolution of photovoltaics. Using solar cells to convert solar energy for hydrogen production (solar hydrogen) [184]-[186] can be considered a promising application (a perfect renewable energy source), as shown in Fig. 5.1(a). Generated hydrogen can convert into not only thermal energy but also electricity and mechanical energy, and return to water finally (a clean, renewable energy cycle), as shown in Fig. 5.2(b).

One of essential factors in solar hydrogen is that the V_{oc}'s of solar cells have to be larger than the dissociating voltage of water (1.23V). [184]-[186] However, the V_{oc}'s of conventional single junction solar cells are not compatible with the dissociating voltage. For matching the requirement, we can probably adopt following four strategies.

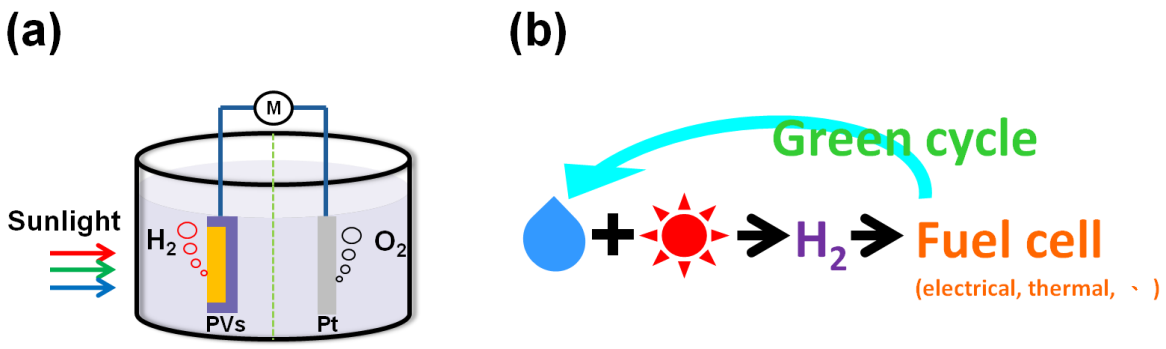

Fig. 5.1 (a) The illustration of converting solar energy for hydrogen production using photovoltaics. (b) The clean, renewable energy cycle of solar hydrogen.

(a) Increasing the n of solar cells

According to Eq. (1.2), increasing n can make V_{oc} larger, but it degrades the FF as well. [159]

(b) Reducing the surface defects of solar cells

Surface defects enlarge the surface recombination rates of solar cells, and thus lower V_{oc}. For reducing surface recombination rates, many surface passivation methods (such as SiN_x passivation [155], and AlO_x passivation [187]) are demonstrated to decrease surface defects, and therefore, enhance V_{oc}. Unfortunately, the augment is limited. Take crystalline silicon solar cells with excellent surface passivation for example. The measured V_{oc}'s are unable to be larger than the built-in voltages of pn junctions (~0.7 V).

(c) Enlarging the bandgaps of the active layers of solar cells

For single junction solar cells, the upper limits of V_{oc}'s are the bandgaps of active layers. It suggests that we can use active materials with larger bandgaps to get higher V_{oc}'s. Nevertheless, using the active materials will make less incident photons be absorbed by solar cells. [188]

(d) Integrating solar cells with different bandgaps (tandem solar cells)

It is an effective way to raise V_{oc}, and incident photons can be efficiently absorbed by solar cells. [103]

Based on the concept of tandem solar cells, we propose a stacking MIS (crystalline silicon) solar cell, which integrates an n-type MIS (crystalline silicon) solar cell with a p-type MIS one, to effectively increase V_{oc}, as shown in Fig. 2.7. There are two advantages using MIS (crystalline silicon) solar cells. First, the fabrication of MIS (crystalline silicon) solar cells is low-cost, low-temperature, simple processes. Second, the V_{oc}'s of MIS (crystalline silicon) solar cells are comparable with those of pn junction (crystalline silicon) solar cells. This is because the ultrathin oxide layers can block the majority carriers from transporting to

the metal electrodes, and are easy for minority carriers to tunnel through, so the effect of carrier recombination at the MS junctions is vastly decreased. [151], [152], [159], [190], [191]

Our experimental results show that by comparing with other MIS solar cells with the same output power, this stacking structure has potential to give high V_{oc} and low J_{sc}, which can reduce the electrical loss in MIS solar cell applications. Furthermore, this stacking structure shows an effective way to enlarge V_{oc} and has potential to achieve a V_{oc} larger than 1.23 V, although the V_{oc}'s of conventional MIS solar cells are not high enough to match the requirement for dissociating water (1.23 V) [184]–[186]. Based on the stacking structure, we believe that MIS solar cells are very promising for photoelectrochemical (PEC) water splitting and that monolithic MIS photovoltaic-PEC devices can be realized in the future for both solar photovoltaics and solar hydrogen.

5.2 Results And Discussions

For obtaining the optimized process conditions of the top and bottom cells of the stacking MIS solar cell, we fabricated n-type and p-type MIS solar cells under different process conditions, and analyzed their characteristics.

The red square curves of Fig. 5.2(a) show the J-V curves of the n-type and p-type MIS solar cells with as-deposited ultrathin SiO_2 layers deposited at 20 mTorr under light illumination, and the measured parameters are listed in Table 5.1. The MIS solar cells exhibit poor photovoltaic characteristics probably because of not good interface properties between the ultrathin SiO_2 layers and Si. To analyze the interface properties of the n-type and p-type MIS solar cells, high-frequency C-V curves were recorded, as shown by the red square curves in Fig. 5.2(b). Large capacitance leakage is observed in both C-V curves. It indicates that there are a great number of trap states at the interfaces, such as silicon dangling bonds and silanol groups. [192], [193] Charge carriers can flow via the trap states to cause current leakage, and the capacitance is reduced. To passivate these trap states, H_2 annealing was

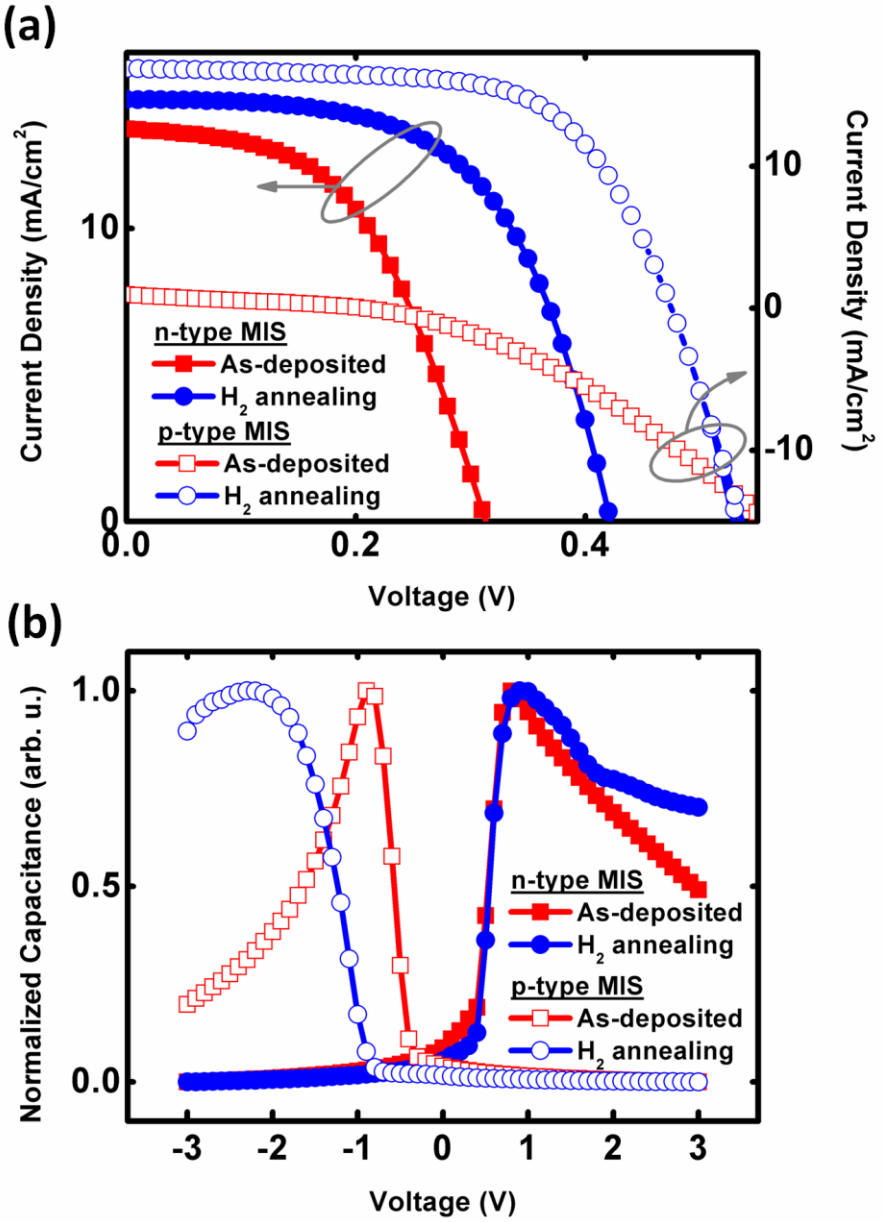

Fig. 5.2 (a) The J-V curves of MIS solar cells with and without H_2 annealing under light illumination. (b) Corresponding C-V curves. All capacitance values are normalized by the largest value of each curve.

introduced. The blue circle curves in Figs. 5.2(a) and (b) show the J-V and C-V curves of MIS solar cells with additional H_2 annealing, respectively. The MIS solar cells with additional H_2 annealing exhibit better photovoltaic properties, and their C-V curves display smaller drops at the accumulation regions. These attribute to the formation of Si-H bonds at the interfaces, and then the trap states are diminished and the leakage currents are decreased. Therefore, H_2

Table 5.1 The measured parameters of MIS solar cells with and without H_2 annealing.

Substrate	H_2 annealing	V_{oc}(mV)	J_{sc} (mA/cm^2)	FF(%)	η (%)
n-type	No	313	13.4	50.7	2.13
	Yes	422	14.4	58.4	3.55
p-type	No	207	0.96	28.8	0.06
	Yes	475	16.9	64.3	5.15

annealing can improve the performance of MIS solar cells with ultrathin SiO_2 layers deposited by RF sputtering because of the passivation of trap states.

The working pressure of depositing the ultrathin SiO_2 layers plays an important role in the V_{oc} of the MIS solar cells with ultrathin SiO_2 layers. The J-V curves of n-type and p-type MIS solar cells with fixed ultrathin sputtering SiO_2 layer thicknesses (n-type with about 2 nm and p-type with about 1 nm) deposited under different working pressures with H_2 annealing are shown in Fig. 5.3 and measured parameters are listed in Table 5.2. For the p-type MIS solar cells, 475 mV, 386 mV, and 350 mV open-circuit voltages, corresponding to working pressures at 20 mTorr, 30 mTorr, and 40 mTorr, respectively, are obtained. The V_{oc}'s of the n-type MIS solar cells are 422 mV, 339 mV, and 313 mV corresponding to working pressures at 20 mTorr, 30 mTorr, and 40 mTorr, respectively. The relationships between the V_{oc}'s and the working pressures during deposition are shown in Fig. 5.4(a). For both MIS solar cells, lower working pressures results in larger V_{oc}'s.

The corresponding C-V measurements are shown in Fig. 5.4(b). The C-V curves of the n-type/p-type MIS solar cells shift toward positive/negative bias with decreasing working pressure. At a lower working pressure, Ar^+ ions get more energy to sputter a SiO_2 target due to a larger mean free path. As a result, more surface charges are introduced in the ultrathin sputtering SiO_2 layers on the Si substrates because of oxygen vacancies. Moreover, the

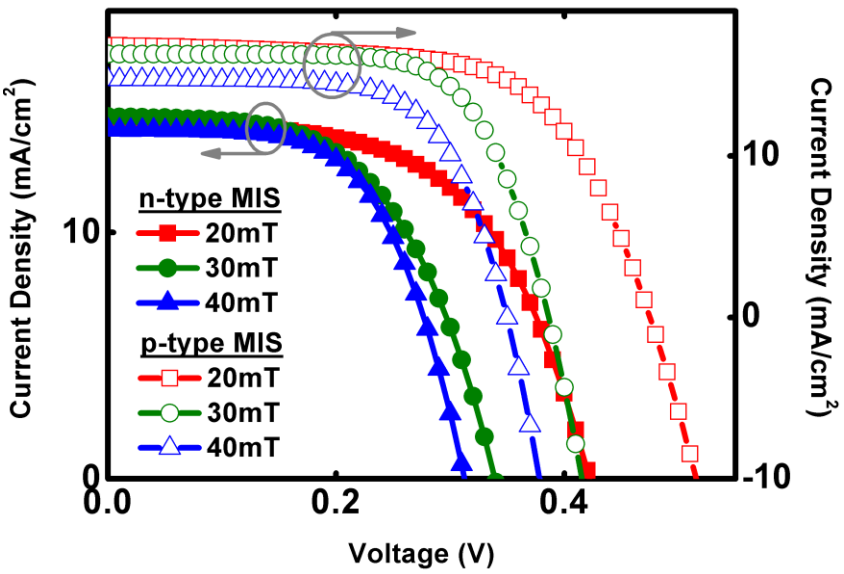

Fig. 5.3 The J-V curves of MIS solar cells with the fixed thicknesses of ultrathin sputtering SiO_2 layers (n-type ~ 2 nm, p-type ~ 1 nm) deposited under different working pressures with H_2 annealing under light illumination.

Table 5.2 The measured parameters of MIS solar cells with the fixed thicknesses of ultrathin sputtering SiO_2 layers (n-type ~ 2 nm, p-type ~ 1 nm) deposited under different working pressures with H_2 annealing under light illumination.

Substrate	Pressure(mTorr)	V_{oc}(mV)	J_{sc} (mA/cm^2)	FF(%)	η (%)
n-type	20	422	14.4	58.4	3.55
	30	339	14.7	55.5	2.77
	40	313	14.2	59.9	2.66
p-type	20	475	16.9	64.3	5.15
	30	386	16.3	68.3	4.31
	40	350	14.8	66.8	3.45

deposition rates of the ultrathin sputtering SiO_2 layers increase with decreasing working pressure in our case. A higher deposition rate reduces the ion bombardment duration at the interfaces. As a result, less trap states are produced, and consequently, V_{oc} is enlarged. According to these two factors, the C-V curves of the p-type MIS solar cells shift toward a

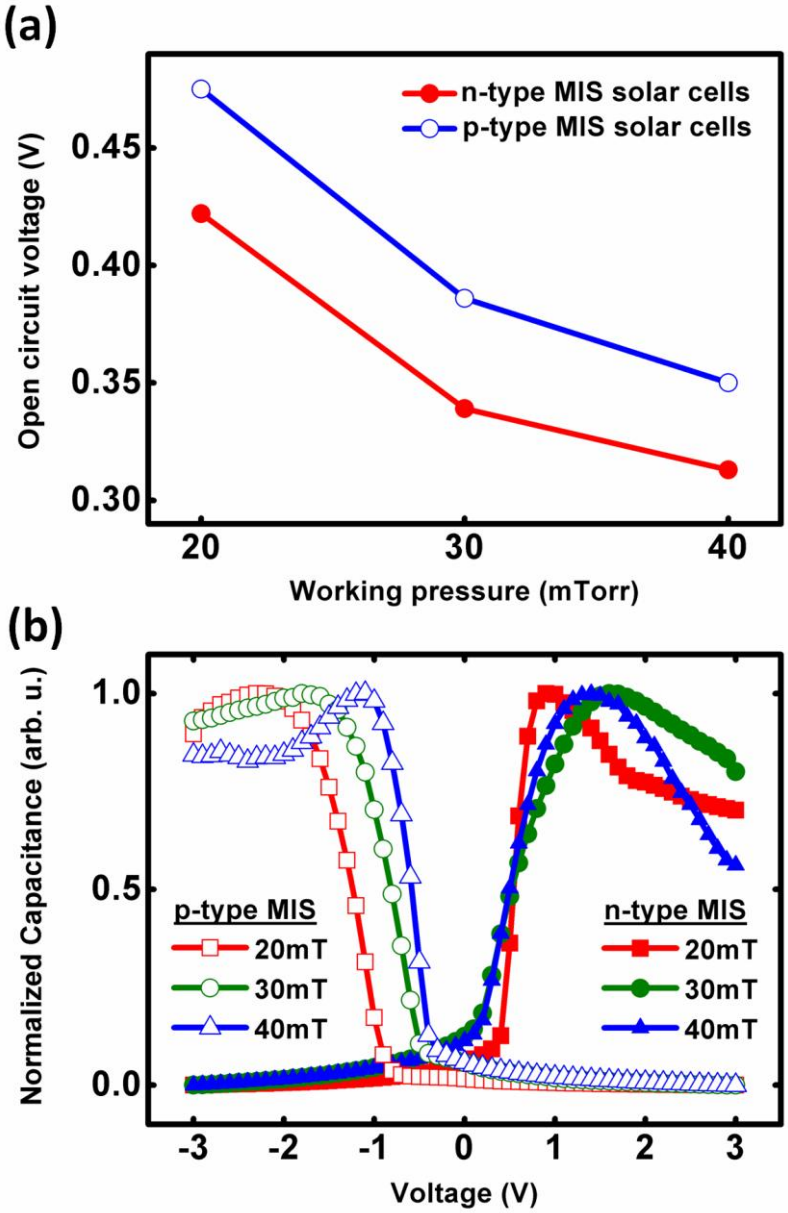

Fig. 5.4 (a) V_{oc} and (b) C-V curves of n-type and p-type MIS solar cells with the fixed thicknesses of ultrathin sputtering SiO_2 layers (n-type ~ 2 nm, p-type ~ 1 nm) deposited under different working pressures with H_2 annealing. All capacitance values are normalized by the largest value of each curve.

more negative voltage with a lower working pressure. However, the voltage shift toward a more positive voltage is not so significant in the C-V curves of the n-type MIS solar cells because of the presence of oxygen vacancies and the requirement of a thicker sputtering SiO_2 insulating layer. This requirement causes much longer ion bombardment duration than

that of the p-type MIS solar cells, and then, more trap states are generated to decrease V_{oc}.

From these results, we chose the best process conditions of the n-type and p-type MIS solar cells to manufacture the top and bottom cells of the stacking MIS solar cell. The fabrication details are introduced in Chapter 2.

The operation of the proposed stacking MIS solar cell is illustrated in Fig. 5.5. The photons incident into the stacking MIS solar cell are absorbed by the top and bottom cells, and electron-hole pairs are generated. The holes in the top cell and the electrons in the bottom cell can transport to and tunnel through the ultrathin SiO_2 layer of each cell and then are collected by the electrodes. In addition, the electrons in the top cell and the holes in the bottom cell can diffuse to and tunnel through the n^+-p^+ junction to recombine. The resulted V_{oc} of the stacking MIS solar cell is given by the sum of the top and bottom cells. For this reason, the proposed stacking MIS solar cell can give a higher V_{oc} than an individual n-type or p-type MIS solar cell, and consequently has much more promising MIS solar cell applications.

The J-V curves of the proposed stacking MIS solar cell with and without

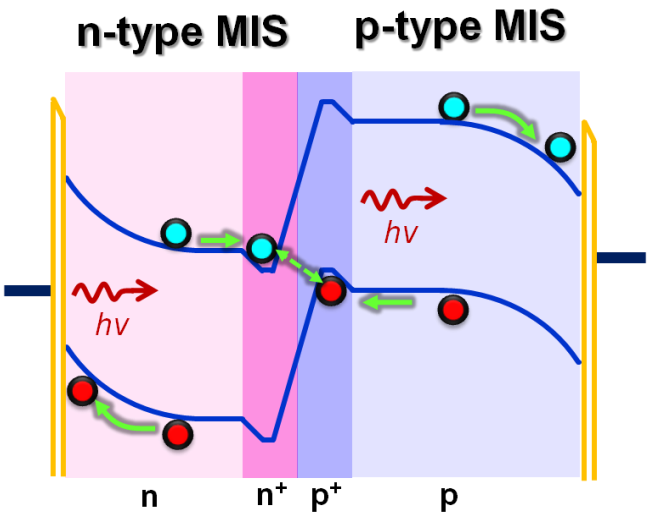

Fig. 5.5 Energy band diagram and operation of the stacking MIS solar cell.

light illumination are shown in Fig. 5.6. In the dark, it provides the nature of a diode. Under illumination, V_{oc} = 0.71 V, J_{sc} = 5.94 mA/cm^2, FF = 58%, and η = 2.47% are obtained. In addition, the J-V curves under illumination of an n-type MIS solar cell and a p-type one after optimization are shown in the inset of Fig. 5.6. The V_{oc}'s are 0.42 and 0.47 V for the n-type and p-type MIS solar cells, respectively. It is obvious that the measured V_{oc} of the stacking MIS solar cell is larger than that of either an n-type or a p-type MIS solar cell. For comparison, the V_{oc}'s of various MIS solar cells using different processes for insulating layers [151]-[153], [157]-[159], [160] are listed in Table 5.3. Note that the V_{oc} of our stacking MIS solar cell is superior to those of the n-type or p-type MIS solar cells with or without surface passivation.

The V_{oc} enhancement has been achieved by the proposed structure. However, the measured V_{oc} is not as expected, and other relative parameters such as η are not comparable with those of conventional MIS solar cells. These attribute to non-optimized processes (such as the bonding process), current mismatching, and optical losses (such as metal reflection).

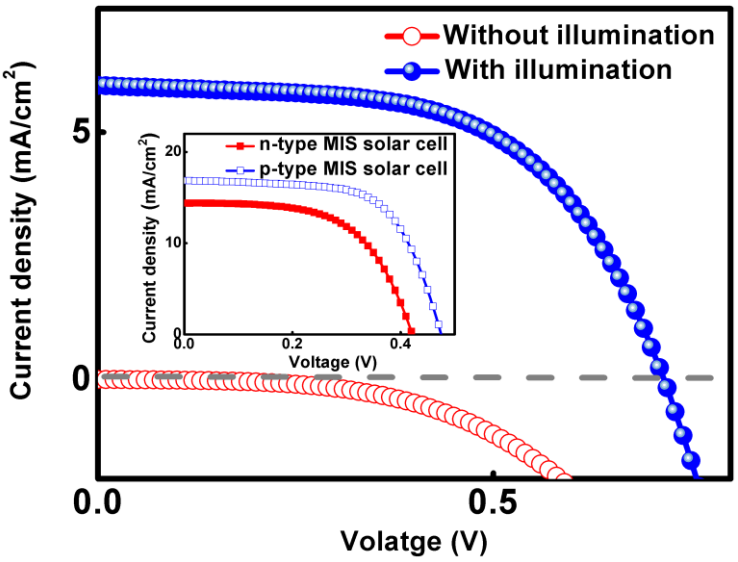

Fig. 5.6 The J-V curves of the stacking MIS solar cell with and without light illumination. Inset: The J-V curves of the optimized n-type and p-type MIS solar cells under light illumination.

Table 5.3 V_{oc} comparison between the proposed stacking MIS solar cell and other MIS and MIS-IL solar cells.

SiO_2 process	Sputtering this work	Chemical [158]	Evaporation [159]	Anodization [160]	Thermal [151]	Thermal [152]	Thermal [153]	Thermal [157]
V_{oc} (V)	0.71	~0.4	0.55	~0.41	~0.41	0.47	0.6	~0.64
Wafer process	Czochralski	-	-	-	-	-	Czochralski	Float-zone
Type	stacking	p	n	p	n	p	p	p
Resistivity (Ω-cm)	1~10	1	1~10	2.8	4.9	2-8	1	0.6
Orientation	<100>	<100>	<111>	<100>	<111>	<100>	-	<100>
Surface passivation or antireflection layer	-	-	-	-	-	-	SiO	SiN_x + Cs^+ ions + textured surfaces
Cell area (cm^2)	0.2	0.019	0.18	0.25	0.33	0.06	3	4.06
Illumination	AM 1.5	AM 1.0	tungsten lamp (with DI water)	AM 1.5	tungsten lamp	tungsten lamp	AM 1.0	AM 1.5

Figure 5.7 shows the IR images of the bonding interface of the stacking MIS solar cell after different fabrication processes. From the IR images, we know that the bonding interface is getting poor during the fabrication of the stacking MIS solar cell. This kind of bonding interface results in a damaged tunneling junction, and thus lowers the V_{oc} of the stacking MIS solar cell.

Current matching between subcells is a critical factor for tandem solar cells and stacking ones to obtain high efficiency. In our case, the thickness tuning is an easy approach to matching the photocurrents of the top and bottom cells. Considering silicon absorption, a rough calculation shows that the thickness of the top cell is about 4 μm, if 50% of photons in the range of 280-1100nm of AM1.5G spectrum reaches the bottom cell. The 400-μm-thick bottom cell with a perfect back reflector can absorb up to 92% of the remaining photons from the top cell. That is, the optimized thickness of the top cell is about 4 μm for the 400-μm-thick bottom cell.

The actual thickness of the top cell of the stacking MIS solar cell is hard to measure directly. We can estimate this thickness by the measured J_{sc}'s of the stacking MIS solar cell and the p-type MIS solar cell shown in the inset of Fig. 5.6. The estimated thickness of the top cell is around 10 μm. This value is thinner than the one obtained from the reference n-type

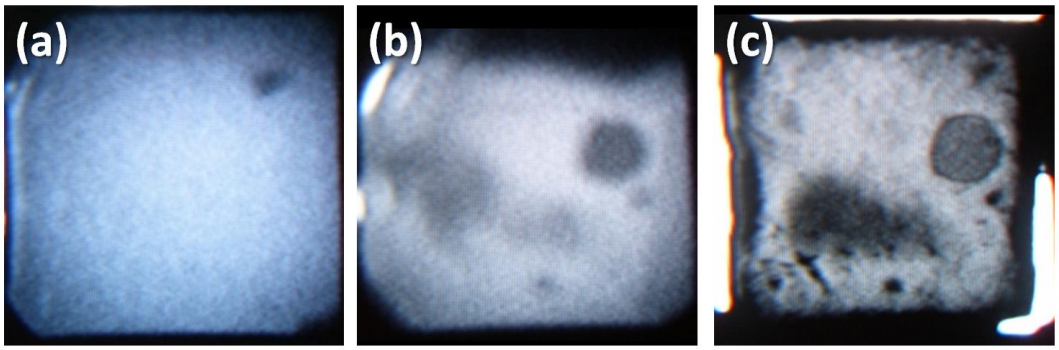

Fig. 5.7 The IR images of the bonding interface of the stacking MIS solar cell (a) as-bonded stacking MIS solar cell. (b) RTA annealed stacking MIS solar cell. (c) Thinned stacking MIS solar cell.

Si substrate, mentioned in Chapter 2, probably because of the inappropriate thickness estimation method and the effect of nonuniform etching during the thinning process. However, the estimated thickness is thicker than 4 μm. That is, current mismatching between the top and bottom cells occurs, and accordingly, degrades the potency of the stacking MIS solar cell.

Optical loss is another major energy loss of the stacking MIS solar cell. The top electrode and the semitransparent metal layer can induce an inversion layer close to the Si/SiO_2 interface to form a MIS junction, and can reduce R_s, but they also obstruct incident photons into the stacking MIS solar cell because of the characteristics of metal, and then cut down the amount of photoexcited carriers.

Substituting the semitransparent metal layer by a surface passivation layer is an effective method for increasing the photon fluxes into the stacking MIS solar cell. [194] The passivation layer can make much more photons inject into the stacking MIS solar cell because of superior transparency. In addition, the passivation layer, which can act as a metal electrode, can induce a similar inversion layer close to the Si/SiO_2 interface to form a MIS junction, to increase the diffusion length of carriers, and to improve the collection efficiency of carriers. [194]

5.3 Summary

It is demonstrated that an MIS solar cell using a stacking structure without surface passivation exhibits a high V_{oc}. The obtained V_{oc} is up to 0.71 V, greater than those of other reported MIS solar cells. We successfully show that the proposed stacking structure is feasible to enhance V_{oc}. It is expected that the performance of the proposed stacking MIS solar cell can be improved by process optimization (such as interface quality after bonding), current matching (such as decreasing the thickness of the top cell), and surface passivation (such as AlO_x for the top cell). Therefore, the proposed stacking MIS solar cell has great potential in the future development of solar cells and PEC water splitting.

Chapter 6

Conclusions And Future Works

6.1 Conclusions

With the dimension(s) of materials shrinking to 1 to 100 nm, especially close to their Bohr radii, they can exhibit special identities. We can employ them in our thin films or devices to accomplish specific purposes. In this dissertation, we utilize three kinds of ultrathin oxide layers to realize three green devices: an OBD with an interfacial Al-O compound layer, an OBD with a MoO_x nanoclusterlike layer, and a high V_{oc} MIS solar cell using a stacking structure.

In the beginning, an OBD with an n-Si/Alq_3/Al structure is fabricated and its characteristics are also analyzed. We find that the bistability of the OBD results from the charge trapping in the Al-O compound layer, which is formed at the Alq_3/Al interface. We can also tune the electrical features of the OBD, which are affected by the surface roughness of the Alq_3 thin film, by controlling the deposition rate of the Alq_3 thin film.

After that, we pay attention to another OBD, p^+-Si/Alq_3/nanostructured MoO_x/Alq_3/Al. The MoO_x nanoclusterlike layer (the nanostructured MoO_x layer) behaves as trap sites in the OBD, and the resistance switching of the OBD can be observed in the I-V curves as charges occupy or leave the trap sites. After the OBD is switched into the high conductance state, the current keeps increasing with voltage, and no NDR exhibits in the I-V curves. This is because the effective polarized field generated by the MoO_x nanoclusterlike layer is not large enough to repel the injected carriers.

In addition, a high V_{oc} MIS solar cell using a stacking structure is reported. We stack an n-type MIS solar cell and a p-type one to form a stacking MIS solar cell. The stacking cell

provides 0.71 V V_{oc}, greater than those of other reported MIS solar cells. It is worthy to mention that the stacking structure has great potential to carry out converting solar energy for hydrogen generation.

Finally, we deeply believe that the reported green devices will make a great influence on the future green technology.

6.2 Future Works

In the near future, we will/can focus on further promoting the performance of the three green devices.

In the case of the OBDs, the retention time of the OBDs is a key identity of memory. However, the retention time of both OBDs has not fitted the requirements of the next generation nonvolatile memory yet. We can introduce deeper trap states in the OBDs (e.g., changing the shape of the MoO_x layer) or barriers adjacent to the original tap sites to prevent trapped charges from escaping, and thus their retention time is raised.

In addition, we find that the failure of the OBDs occurs after several write-read-erase-read cycle tests. The failure probably attributes to many factors, such as device degradation due to the measurement environment, and leakage paths which result from particles introduced during fabrication. However, the failures of organic memory have not caused much attention. If we can recognize the failure mechanisms, we can figure out how to tackle the causes of the failure and then can uplift the stability and endurance of the OBDs, and even perhaps can understand the mechanisms responsible for the resistance switching.

With regard to the stacking MIS solar cell, it is evident that the stacking MIS solar cell offers higher V_{oc} than other published MIS solar cells. But the stacking MIS solar cell can donate more superior performance as long as we can cut down its power losses. For example, we can modify (or change) our fabrication processes and then can optimize the processes for

the requirement of current matching and for obtaining the excellent bonding interface and high quality MIS junctions. After that, we can use a surface passivation layer (such as AlO_x) instead of the semitransparent metal layer to raise the amount of photons incident into the cell, and to induce an inversion layer for arguing the diffusion length and collection efficiency of carriers. Furthermore, from the point of view of energy collection, the performance of the stacking solar cell (such as conversion efficiency) can be further upgraded using two MIS solar cells with different bandgaps (such as Si/Ge, and Si/III-V).

References

[1] G. A. Meeh, W. M. Washington, W. D. Collins, J. M. Arblaster, A. Hu, L. E. Buja, W. G. Strand, and H. Teng, "How much more global warming and sea level rise?," *Science*, vol. 307, no. 5716, pp. 1769-1772, Mar. 2005.

[2] T. L. Root, J. T. Price, K. R. Hall, S. H. Schneider, C. Rosenzweig, and J. A. Pounds, "Fingerprints of global warming on wild animals and plants," *Nature*, vol. 421, no. 6918, pp. 57-60, Jan. 2002.

[3] B. Eitan, P. Pavan, I. Bloom, E. Aloni, A. Frommer, and D. Finzi, "NROM: A novel localized trapping, 2-bit nonvolatile memory cell," *IEEE Electron. Dev. Lett.*, vol. 21, no. 11, pp. 543-545, Nov. 2000.

[4] D. Zhao, Y. Zhu, R. Li, and J. Liu, "Simulation of a cobalt silicide/Si hetero-nanocrystal memory," *Solid-State Electron.*, vol. 49, no. 12, pp. 1974-1977, Dec. 2005.

[5] C. J. Amsinck, N. H. D. Spigna, D. P. Nackashi, and P. D. Franzon, "Scaling constraints in nanoelectronic random-access memories," *Nanotechnol.*, vol. 16, no. 10, pp. 2251-2260, Aug. 2005.

[6] S. Lai, "Current status of the phase change memory and its future," *Proc. IEEE Int. Electron Devices Meeting*, 2003, pp. 10.1.1-4.

[7] R. J. Tseng, J. Huang, J. Ouyang, R. B. Kaner, and Y. Yang, "Polyaniline nanofiber/gold nanoparticle nonvolatile memory," *Nano Lett.*, vol. 5, no.6, pp. 1077-1080, May 2005.

[8] D. Prime and S. Paul, "Overview of organic memory devices," *Phil. Trans. R. Soc. A*, vol. 367, no. 1095, pp. 4141-4157, Oct. 2009.

[9] T. W. Hickmott, "Low-frequency negative resistance in thin anodic oxide films," *J. Appl. Phys.*, vol. 33, no. 9, pp. 2669-2682, Sept. 1962.

[10] J. G. Simmons and R. R. Verderber, "New conduction and reversible memory phenomena in thin insulating films," *Proc. R. Soc. Lond. A*, vol. 301, no. 1464, pp. 77-102, Oct. 1967.

[11] R. R. Sutherland, "Theory for negative resistance and memory effects in thin insulating films and its application to Au-ZnS-Au devices," *J. Phys. D Appl. Phys.*, vol. 4, no. 3, pp. 468-479, Mar. 1971.

[12] A. Ansari and A. Qadeer, "Memory switching in thermally grown titanium-oxide films," *J. Phys. D Appl. Phys.*, vol. 18, no. 5, pp. 911-917, May 1985.

[13] C. A. Hogarth and M. Zor, "Some observations of voltage-induced conductance changes in thin films of evaporated polyethylene." *Thin Solid Films*, vol. 27, no. 1, pp. L5-L7, May 1975.

[14] C. Barriac, P. Pinard, and F. Davoine, "Study of the electrical properties of

Al-Al_2O_3-metal Structures," *Phys. Status Sol.*, vol. 34, no. 2, pp. 621-633, Aug. 1969.

[15] G. Dearnaley, D. V. Morgan, and A. M. Stoneham, "A model for filament growth and switching in amorphous oxide films," *J. Non-Cryst. Solids*, vol. 4, pp. 593-612, Apr. 1970.

[16] R. Blessing, K. H. Gurtler, and H. Pagnia, "Switching of point-contact diodes consisting of discontinuous gold films," *Phys. Lett. A*, vol. 84, no. 6, pp. 341-344, Aug.1981.

[17] R. E. Thurstans and D. P. Oxley, "The electroformed metal-insulator-metal structure: a comprehensive model," *J. Phys. D Appl. Phys.*, vol. 35, no. 8, pp. 802-809, Apr. 2002.

[18] L. V. Gregor, "Electrical conductivity of polydivinylbenzene films," *Thin Solid Films*, vol. 2, no. 3, pp. 235-246, Sept. 1968.

[19] L. V. Gregor, "Polymer dielectric films," *IBM J. Res. Dev.*, vol. 12, no. 2, pp. 140-162, Mar. 1968.

[20] H. Carchano, R. Lacoste, and Y. Segui, "Bistable electrical switching in polymer thin films," *Appl. Phys. Lett.*, vol. 19, no. 10, pp. 414-415, Nov. 1971.

[21] L. F. Pender and R. J. Fleming, "Memory switching in glow discharge polymerized thin films," *J. Appl. Phys.*, vol. 46, no. 8, pp. 3426-3431, Aug. 1975.

[22] A. Szymanski, D. C. Larson, and M. M. Labes, "A temperature-independent conducting state in tetracene thin film," *Appl. Phys. Lett.*, vol. 14, no. 3, pp. 88-90, Feb. 1969.

[23] J. Kevorkian, M. M. Labes, D. C. Larson, and D. C. Wu, "Bistable switching in organic thin films," *Discuss. Faraday Soc.*, vol. 51, pp. 139-143, Apr. 1971.

[24] L. P. Ma, J. Liu, S. Pyo, Q. Xu, and Y. Yang, "Organic bistable devices," *Mol. Cryst. Liq. Cryst.*, vol. 378, no. 1, pp.185-192, Jan. 2002.

[25] L. P. Ma, J. Liu, S. Pyo, Q. Xu, and Y. Yang, "Organic bistable light-emitting devices," *Appl. Phys. Lett.*, vol. 80, no. 3, pp. 362-364, Jan. 2002.

[26] L. P. Ma, J. Liu, Q. Xu, and Y. Yang, "Organic electrical bistable devices and rewritable memory cells," *Appl. Phys. Lett.*, vol. 80, no. 16, pp. 2997-2999, 2002.

[27] L. Ma, S. Pyo, J. Ouyang, Q. Xu, and Y. Yang, "Nonvolatile electrical bistability of organic/metal-nanocluster/organic system," *Appl. Phys. Lett.*, vol. 82, no. 9, pp. 1419-1421, Mar. 2003.

[28] J. C. Scott and L. D. Bozano, "Nonvolatile Memory Elements Based on Organic Materials," *Adv. Mater.*, vol. 19, no. 11, pp. 1452-1463, Jun. 2007.

[29] A. R. Elsharkawi and K. C. Kao, "Switching and memory phenomena in anthracene thin films," *J. Phys. & Chem. of Solids*, vol. 38, no. 1, pp 95-96, Jan. 1977.

[30] J. Chen, L. Xu, J. Lin, Y. Geng, L. Wang, and D. Ma, "Negative differential

resistance effect in organic devices based on an anthracene derivative," *Appl. Phys. Lett.*, vol. 89, no. 8, p. 083 514, Aug. 2006.

[31] D. Tondelier, K. Lmimouni, D. Vuillaume, C. Fery, and G. Haas, "Metal⁄organic⁄metal bistable memory devices," *Appl. Phys. Lett.*, vol. 85, no. 23 , pp. 5763-5765, Oct. 2004.

[32] A. K. Mahapatro, R. Agrawal, and S. Ghosh, "Electric-field-induced conductance transition in 8-hydroxyquinoline aluminum (Alq_3)," *J. Appl. Phys.*, vol. 96, no. 6, pp. 3583-3585, Sept. 2004.

[33] C. -H. Tu, Y. -S. Lai, and D. -L. Kwong, "Memory effect in the current-voltage characteristic of 8-hydroquinoline aluminum salt films," *IEEE Elec. Dev. Lett.*, vol. 27, no. 5, pp. 354-356, May 2006.

[34] W. Tang, H. Z. Shi, G. Xu, B. S. Ong, Z. D. Popovic, J. C. Deng, J. Zhao, and G. H. Rao, "Memory effect and negative differential resistance by electrode-induced two-dimensional single-electron tunneling in molecular and organic electronic devices," *Adv. Mater.*, vol.17, no. 19, pp. 2307-2311, Oct. 2005.

[35] M. Cölle, M. Büchel, and D. M. de Leeuw, **"**Switching and filamentary conduction in non-volatile organic memories**,"** *Org. Electron.*, vol. 7, no. 5, pp. 305-312, Oct. 2006.

[36] M. Terai, K. Fujita, and T. Tsutsui, "Electrical bistability of organic thin-film device using Ag electrode," *Jpn. J. Appl. Phys.*, vol. 45, no. 4B, pp. 3754-3757, Apr. 2006.

[37] A. Bandyopadhyay and A. J. Pal, **"**Key to design functional organic molecules for binary operation with large conductance switching **,"** *Chem. Phys. Lett.*, vol. 371, no. 1-2, pp. 86-90, Mar. 2003.

[38] A. Bandhopadhyay and A. J. Pal, "Large conductance switching and binary operation in organic devices: Role of functional groups," *J. Phys. Chem. B*, vol. 107, no. 11, pp 2531-2536, Feb. 2003.

[39] M. Kushida, Y. Imaizumi, K. Harada, and K. Sugita, **"**Organic bistable memory switching phenomena and H-like aggregates in squarylium dye Langmuir-Blodgett films**,"** *Thin Solid Films*, vol. 509, no. 1-2, pp. 149-153, Jun. 2006.

[40] H. K. Henisch and W. R. Smith, "Switching in organic polymer films," *Appl. Phys. Lett.*, vol. 24, no. 12, pp. 589-591, Jun. 1974.

[41] Y. Segui, B. Ai, and H. Carchano, "Switching in polystyrene films: Transition from on to off state," *J. Appl. Phys.*, vol. 47, no. 1, pp. 140-143, Jan. 1976.

[42] Y. -S. Lai, C. -H. Tu, D. -L. Kwong, and J. S. Chen, "Bistable resistance switching of poly(N-vinylcarbazole) films for nonvolatile memory applications," *Appl. Phys. Lett.*, vol. 87, no. 12, p. 122 101, Sept. 2005,

[43] H. S. Majumdar, A. Bandyopadhyay, A. Bolognesi, and A. J. Pal, "Memory device

applications of a conjugated polymer: Role of space charges," *J. Appl. Phys.*, vol. 91, no. 4, pp. 2433-2437, Nov. 2002.

[44] H. S. Majumdar, A. Bolognesi, and A. J. Pal, **"**Switching and memory devices based on a polythiophene derivative for data-storage applications **,"** *Synth. Met.*, vol. 140, no. 2-3, pp. 203-206, Feb. 2004.

[45] M. Lauters, B. McCarthy, D. Sarid, and G. E. Jabbour, "Multilevel conductance switching in polymer films," *Appl. Phys. Lett.*, vol. 89, no. 1, p. 013 507, Jul. 2006.

[46] D. Ma, M. Aguiar, J. A. Freire, and I. A. Hümmelgen, "Organic reversible switching devices for memory applications," *Adv. Mater.*, vol. 12, no. 14, pp. 1063-1066, Jul. 2000.

[47] H. S. Majumdar, A. Bandyopadhyay, and A. J. Pal, **"**Data-storage devices based on layer-by-layer self-assembled films of a phthalocyanine derivative**,"** *Org. Electron.*, vol. 4, no. 1, pp. 39-44, Jun. 2003.

[48] A. Bandyopadhyay and A. J. Pal, "Large conductance switching and memory effects in organic molecules for data-storage applications," *Appl. Phys. Lett.*, vol. 82, no. 8, pp. 1215-1217, Feb. 2003.

[49] J. Chen, L. Xu, J. Lin, Y. Geng, L. Wang, and D. Ma, "Negative differential resistance effect in organic devices based on an anthracene derivative," *Appl. Phys. Lett.*, vol. 89, no. 8**,** p. 083 514, Aug. 2006.

[50] R. S. Potember, T. O. Poehler, and D. O. Cowan, "Electrical switching and memory phenomena in Cu-TCNQ thin films," *Appl. Phys. Lett.*, vol. 34, no. 6, pp. 405-407, Mar. 1979.

[51] M. Ouyang, S. M. Hou, H. F. Chen, K. Z. Wang, and Z. Q. Xue, "A new organic-organic complex thin film with reproducible electrical bistability properties," *Phys. Lett. A*, vol. 235, no. 4, pp. 413-417, Nov. 1997.

[52] J. Fang, H. You, J. Chen, J. Lin, and D. Ma, "Memory devices based on lanthanide (Sm^{3+}, Eu^{3+}, Gd^{3+}) complexes," *Inorg. Chem.*, vol. 45, no. 9, pp. 3701-3704, Apr. 2006.

[53] B. Pradhan, S. K. Batabyal, and A. J. Pal, "Electrical bistability and memory phenomenon in carbon nanotube-conjugated polymer matrixes," *J. Phys. Chem. B*, vol.110, no. 16, pp. 8274-8277, Apr. 2006.

[54] C. W. Chu, J. Ouyang, J. -H. Tseng, and Y. Yang, "Organic donor-acceptor system exhibiting electrical bistability for use in memory devices," *Adv. Mater.*, vol. 17, no. 11, pp. 1440-1443, Jun. 2005.

[55] Q. Ling, Y. Song, S. J. Ding, C. Zhu, D. S. H. Chan, D. -L. Kwong, E. -T. Kang, and K. -G. Neoh, "Non-volatile polymer memory device based on a novel copolymer of *N*-vinylcarbazole and Eu-complexed vinylbenzoate," *Adv. Mater.*, vol. 17, no. 4, pp. 455-459, Feb. 2005.

[56] Q. -D. Ling, Y. Song, S. -L. Lim, E. Y. -H. Teo, Y. -P. Tan, C. Zhu, D. S. H. Chan, D. -L. Kwong, E. -T. Kang, and K.- G. Neoh, "A dynamic random access memory based on a conjugated copolymer containing electron-donor and -acceptor moieties," *Angew. Chem. Int. Ed.*, vol. 45, no. 18, pp. 2947-2951, Apr. 2006.

[57] Y. Song, Q. D. Ling, C. Zhu, E. T. Kang, D. S. H. Chan, Y. H. Wang, and D. -L. Kwong, "Memory performance of a thin-film device based on a conjugated copolymer containing fluorene and chelated europium complex," *IEEE Electron Device Lett.*, vol. 27, no. 3, pp. 154-156, Mar. 2006.

[58] L. Ma, Q. Xu, and Y. Yang, "Organic nonvolatile memory by controlling the dynamic copper-ion concentration within organic layer," *Appl. Phys. Lett.*, vol. 84, no. 24, pp. 4908-4910 , May 2004.

[59] J. H. Krieger, S. V. Trubin, S. B. Vaschenko, and N. F. Yudanov, "Molecular analogue memory cell based on electrical switching and memory in molecular thin films," *Synth. Met.*, vol. 122, no. 1, pp. 199-202, May 2001.

[60] F. Verbakel, S. C. J. Meskers, and R. A. J. Janssen, "Electronic memory effects in a sexithiophene-poly(ethylene oxide) block copolymer doped with NaCl. combined diode and resistive switching behavior," *Chem. Mater.*, vol. 18, no. 11, pp 2707-2712, May 2006.

[61] Q. Lai, Z. Zhu, Y. Chen, S. Patil, and F. Wudl, "Organic nonvolatile memory by dopant-configurable polymer," *Appl. Phys. Lett.*, vol. 88, no. 13, p.133 515, Mar. 2006.

[62] L. D. Bozano, B. W. Kean, M. Beinhoff, K. R. Carter, P. M. Rice, and J. C. Scott, "Organic materials and thin-film structures for cross-point memory cells based on trapping in metallic nanoparticles," *Adv. Funct. Mater.*, vol. 15, no. 12, pp. 1933-1939, Dec. 2005.

[63] L. D. Bozano, B. W. Kean, V. R. Deline, J. R. Salem, and J. C. Scott, "Mechanism for bistability in organic memory elements," *Appl. Phys. Lett.*, vol. 84, no.4, pp. 607-609, Jan. 2004.

[64] J. Ouyang, C. -W. Chu, C. R. Szmanda, L. Ma, and Y. Yang, "Programmable polymer thin film and non-volatile memory device," *Nat. Mater.*, vol. 3, no. 12, pp. 918-922, Nov. 2004.

[65] A. Prakash, J. Ouyang, J. -L. Lin, and Y. Yang, "Polymer memory device based on conjugated polymer and gold nanoparticles," *J. Appl. Phys.*, vol.100, no. 5, pp. 054309-054314, Sept. 2006.

[66] H. -T. Lin, Z. Pei, and Y. –J. Chan, "Carrier transport mechanism in a nanoparticle-incorporated organic bistable memory device," *IEEE Electron Device Lett.*, vol. EDL-28, no. 7, pp. 569-571, Jul. 2007.

[67] J. Ouyang, C. -W. Chu, D. Sieves, and Y. Yang, "Electric-field-induced charge

transfer between gold nanoparticle and capping 2-naphthalenethiol and organic memory cells," *Appl. Phys. Lett.*, vol. 86, no. 12, p. 123 507, Mar. 2005.

[68] H. J. Gao, Z. Q. Xue, Q. D. Wu, and S. J. Pang, "Structure and electrical properties of Ag-ultrafine-particle–polymer thin films," *J. Vac. Sci. Technol. B*, vol. 13, no. 3, pp. 1242-1246, May-Jun. 1995.

[69] A. Kiesow, J. E. Morris, C. Radehaus, and A. Heilmann, "Switching behavior of plasma polymer films containing silver nanoparticles," *J. Appl. Phys.*, vol. 94, no. 10, pp. 6988-6990, Nov. 2003.

[70] S. H. Kang, T. Crisp, I. Kymissis, and V. Bulović, "Memory effect from charge trapping in layered organic structures," *Appl. Phys. Lett.*, vol. 85, no. 20, pp. 4666-4668, 2004.

[71] T. Ouisse and O. Stéphan, "Electrical bistability of polyfluorene device," *Org. Electron.*, vol. 5, no. 5, pp. 251-256, Sept 2004.

[72] R. J. Tseng, C. Tsai, L. Ma, J. Ouyang, C. S. Ozkan, and Y. Yang, "Digital memory device based on tobacco mosaic virus conjugated with nanoparticles," *Nat. Nanotechnol.*, vol. 1, no.1, pp. 72-77, Oct. 2006.

[73] F. Verbakel, S. C. J. Meskers, and R. A. J. Janssen, "Electronic memory effects in diodes from a zinc oxide nanoparticle-polystyrene hybrid material," *Appl. Phys. Lett.*, vol. 89, no. 10, p. 102 103, Sept. 2006.

[74] S. Yook, S. O. Jeon, C. W. Joo, J. Y. Lee, S. H. Kim, and J. Jang, **"**Organic bistable memory device using MoO_3 nanocrystal as a charge trapping center**,**" *Org. Electron.*, vol. 10, no. 1, pp. 48-52, Feb. 2009.

[75] T. -Y. Chang, Y. -W. Cheng, and P. -T. Lee, "Electrical characteristics of an organic bistable device using an Al/Alq_3/nanostructured MoO_3/Alq_3/p^+-Si structure," *Appl. Phys. Lett.*, vol. 96, no. 4, p. 043 309, Jan. 2010.

[76] C. P. Collier, G. Mattersteig, E. W. Wong, Y. Luo, K. Beverly, J. Sampaio, F. M. Raymo, J. F. Stoddart, and J. R. Heath, "A [2]catenane-based solid state electronically reconfigurable switch," *Science*, vol. 289. no. 5482, pp. 1172-1175, Aug. 2000.

[77] Y. Liu, N. Li, X. Xia, Q. Xu, J. Ge, and J. Lu, "WORM memory devices based on conformation change of a PVK derivative with a rigid spacer in side chain," *Mater. Chem. and Phys.*, vol.123, no. 2-3, pp. 685-689, Oct. 2010.

[78] P. Mark and W. Helfrich, "Space-charge-limited currents in organic crystals," *J. Appl. Phys.*, vol. 33, no. 1, pp. 205-215, Jun. 1962.

[79] J. G. Simmons, "Generalized formula for the electric tunnel effect between similar electrodes separated by a thin insulating film," *J. Appl. Phys.*, vol. 34, no. 6, pp. 1793-1803, Jun. 1963.

[80] M. Lenzlinger and E. H. Snow, "Fowler-Nordheim tunneling into thermally grown

SiO_2," *J. Appl. Phys.*, vol. 40, no. 1, pp. 278-283, Jan. 1969.

[81] A. Schenk and G. Heiser, **"**Modeling and simulation of tunneling through ultra-thin gate dielectrics**,"** *J. Appl. Phys.*, vol. 81, no. 12, pp. 7900-7908, Jun. 1997.

[82] D. M. Chapin, C. S. Fuller, and G. L. Pearsonv, "A new silicon *p-n* junction photocell for converting solar radiation into electrical power," *J. Appl. Phys.*, vol. 25, no. 5, pp. 676-677, May 1954.

[83] J. -L. Desplat, "Near-uv photon efficiency in a TiO_2 electrode: Application to hydrogen production from solar energy," *J. Appl. Phys.*, vol. 47, no. 11, pp. 5102-5104, Nov. 1976.

[84] W. A. Anderson, A. E. Delahoy, J. K. Kim, S. H. Hyland, and S. K. Dey, "High-efficiency Cr-MIS solar cells on single and polycrystalline silicon," *Appl. Phys. Lett.*, vol. 33, no. 7, pp. 588-590, Oct. 1978.

[85] W. E. Spear, P. G. Le Comber, S. Kinmond, and M. H. Brodsky, "Amorphous silicon p-n junction," *Appl. Phys. Lett.*, vol. 28, no. 2, pp. 105-107, Jan. 1976.

[86] S. M. Bedair, M. F. Lamorte, and J. R. Hauser, "A two-junction cascade solar-cell structure," *Appl. Phys. Lett.*, vol. 34, no. 1, pp. 38-39, Jan. 1979.

[87] I. Hagemann, **"**PV in buildings - The influence of PV on the design and planning process of a building**,"** *Renew. Energ.*, vol. 8, no. 1-4, pp. 467-470, May-Aug. 1996.

[88] A. Metz and R. Hezel, "Record efficiencies above 21% for MIS-contacted diffused junction silicon solar cells," *Proc. IEEE 26th Photovolt. Specialist Conf.*, 1997, pp. 283-286.

[89] J. Zhao, A. Wang, and M. A. Green, "24.5% efficiency silicon PERT cells on MCZ substrates and 24.7% efficiency PERL cells on FZ substrates" *Prog. Photovol. : Res. Appl.*, vol. 7, no. 6, pp. 471-474, Nov.-Dec. 1999.

[90] R. Hezel, "High-efficiency OECO Czochralski-silicon solar cells for mass production," *Sol. Energy Mater. Sol. Cells*, vol. 74, no. 1-4, pp. 25-33, Oct. 2002.

[91] J. Zhao, A. Wang, M. A. Green, and F. Ferrazza, "19.8% efficient "honeycomb" textured multicrystalline and 24.4% monocrystalline silicon solar cells," *Appl. Phys. Lett.*, vol. 73, no. 14, pp. 1991-1993, Oct. 1998.

[92] R. Lüdemann, "Hydrogen passivation of multicrystalline silicon solar cells," *Mater. Sci. Eng. B*, vol. 58, no. 1-2, pp. 86-90, Feb. 1999.

[93] O. Schultz, S. W. Glunz, and G. P. Willeke, "Multicrystalline silicon solar cells exceeding 20% efficiency," *Prog. Photovol. : Res. Appl.*, vol. 12, no. 7, pp. 553-558, Nov. 2004.

[94] H. J. Möller, C. Funke, M. Rinio, and S. Scholz, "Multicrystalline silicon for solar cells," *Thin Solid Films*, vol. 487, no.1-2, pp. 179-187, Sept. 2005.

[95] M. A. Green, "Crystalline and thin-film silicon solar cells: state of the art and future

potential," *Sol. Energy*, vol. 74, no. 3, pp. 181-192, Mar. 2003.

[96] M. Taguchi, H. Sakata, Y. Yoshimine, E. Maruyama, A. Terakawa, M. Tanaka, and S. Kiyama, "An approach for the higher efficiency in the HIT cells," *Proc. IEEE 31th Photovolt. Specialist Conf.*, 2005, pp. 866 - 871.

[97] R. B. Bergmann, T. J. Rinke, T. A. Wagner, and J. H. Werner, "Thin film solar cells on glass based on the transfer of monocrystalline Si films," *Sol. Energy Mater. Sol. Cells*, vol. 65, no.1-4, pp. 355-361, Jan. 2001.

[98] M. A. Green, P. A. Basore, N. Chang, D. Clugston, R. Egan, R. Evans, D. Hogg, S. Jarnason, M. Keevers, P. Lasswell, J. O. Sullivan, U. Schubert, A. Turner, S. R. Wenham, and T. Young, "Crystalline silicon on glass (CSG) thin-film solar cell modules," *Sol. Energy*, vol. 77, no. 6, pp. 857-863, Dec. 2004.

[99] K. Yamamoto, A. Nakajima, T. Suzuki, M. Yoshimi, H. Nishio, and M. Izumina, "Thin-film polycrystalline Si solar cell on glass substrate fabricated by a novel low temperature process," *Proc. IEEE 24th Photovolt. Specialist Conf.*, 1994, pp. 1575-1578.

[100] K. Yamamoto, "Very thin film crystalline silicon solar cells on glass substrate fabricated at low temperature," *IEEE Trans. on Electron Devices*, vol. 46, no. 10 pp. 2041-2047, Oct. 1999.

[101] R. R. Arya, A. Catalano, and R. S. Oswald, "Amorphous silicon p-i-n solar cells with graded interface," *Appl. Phys. Lett.*, vol. 49, no. 17, pp.1089-1091, Oct. 1986.

[102] J. Meier, R. Flückiger, H. Keppner, and A. Shah, "Complete microcrystalline p-i-n solar cell-Crystalline or amorphous cell behavior?," *Appl. Phys. Lett.*, vol. 65, no. 7, pp. 860-862, Aug. 1994.

[103] J. Yang, A. Banerjee, and S. Guha, "Triple-junction amorphous silicon alloy solar cell with 14.6% initial and 13.0% stable conversion efficiencies," *Appl. Phys. Lett.*, vol. 70, no. 22, pp. 2975-2977, Jun. 1997.

[104] K. Yamamoto, M. Yoshimi, Y. Tawada, S. Fukuda, T. Sawada, T. Meguro, H. Takata, T. Suezaki, Y. Koi, K. Hayashi, T. Suzuki, M. Ichikawa, and A. Nakajima, "Large area thin film Si module," *Sol. Energy Mater. Sol. Cells*, vol. 74, no. 1-4, pp. 449-455, Oct. 2002.

[105] D. A. Jenny, J. J. Loferski, and P. Rappaport, "Photovoltaic effect in GaAs p-n junctions and solar energy conversion," *Phys. Rev.*, vol. 101, no. 3, pp. 1208-1209, Feb. 1956.

[106] R. R. King, P. C. Colter, D. E. Joslin, K. M. Edmondson, D. D. Krut, N. H. Karam, and S. Kurtz, "High-voltage, low-current GaInP/GaInP/GaAs/GaInNAs/Ge solar cells," *Proc. EEE 29th Photovolt. Specialist Conf.*, 2002, pp. 852-855.

[107] R. R. King, D. C. Law, K. M. Edmondson, C. M. Fetzer, G. S. Kinsey, H. Yoon, R. A. Sherif, and N. H. Karam, "40% efficient metamorphic GaInP/GaInAs/Ge

multijunction solar cells," *Appl. Phys. Lett.*, vol. 90, vol. 5, p.183 516, May 2007.

[108] W. Guter, J. Schöne, S. P. Philipps, M. Steiner, G. Siefer, A. Wekkeli, E. Welser, E. Oliva, A. W. Bett, and F. Dimroth, "Current-matched triple-junction solar cell reaching 41.1% conversion efficiency under concentrated sunlight," *Appl. Phys. Lett.*, vol. 94, no. 22, p. 223 504, Jun. 2009.

[109] R. Venkatasubramanian, B. C. O'Quinn, J. S. Hills, P. R. Sharps, M. L. Timmons, J. A. Hutchby, H. Field, R. Ahrenkiel, and B. Keyes, "18.2% (AM1.5) efficient GaAs solar cell on optical-grade polycrystalline Ge substrate" *Proc.IEEE 25th Photovolt. Specialist Conf.*, 1996, pp. 31-36.

[110] G. J. Bauhuis, P. Mulder, E. J. H. Kamp, J. C. C. M. Huijben, and J. J. Schermer, "26.1% thin-film GaAs solar cell using epitaxial lift-off," *Sol. Energy Mater. Sol. Cells*, vol. 93, no. 9, pp. 1488-1491, Sept. 2009.

[111] T. Aramoto, S. Kumazawa, H. Higuchi, T. Arita, S. Shibutani, T. Nishio, J. Nakajima, M. Tsuji, A. Hanafusa, T. Hibino, K. Omura, H. Ohyama, and M. Murozono, "16.0% efficient thin-film CdS/CdTe solar cells," *Jpn. J. Appl. Phys.*, vol. 36, no. 10, pp. 6304-6305, Oct. 1997.

[112] D. H. Rose, F. S. Hasoon, R. G. Dhere, D. S. Albin, R. M. Ribelin, X. S. Li, Y. Mahathongdy, T. A. Gessert, and P. Sheldon, "Fabrication procedures and process sensitivities for CdS/CdTe solar cells," *Prog. Photovol. : Res. Appl.*, vol.7, no. 5, pp. 331-340, Sept.-Oct. 1999.

[113] X. Wu, "High-efficiency polycrystalline CdTe thin-film solar cells," *Sol. Energy*, vol. 77, no. 6, pp. 803-814, Dec. 2004.

[114] X. Mathew, J. P. Enriquez, A. Romeo, and A. N. Tiwari, "CdTe/CdS solar cells on flexible substrates," *Sol. Energy*, vol. 77, no. 6, pp. 831-838, Dec. 2004.

[115] M. A. Contreras, B. Egaas, K. Ramanathan, J. Hiltner, A. Swartzlander, F. Hasoon, and R. Noufi, "Progress toward 20% efficiency in Cu(In,Ga)Se_2 polycrystalline thin-film solar cells," *Prog. Photovol. : Res. Appl.*, vol. 7, no. 4, pp. 311-316, Jul.-Aug. 1999.

[116] J. Wennerberg, , J. Kessler, and L. Stolt, "Cu(In,Ga)Se_2-based thin-film photovoltaic modules optimized for long-term performance," *Sol. Energy Mater. Sol. Cells*, vol. 75, no. 1-2, pp. 47-55, Jan. 2003.

[117] M. Bär, I. Repins, M. A. Contreras, L. Weinhardt, R. Noufi, and C. Heske, "Chemical and electronic surface structure of 20%-efficient Cu(In,Ga)Se_2 thin film solar cell absorbers," *Appl. Phys. Lett.*, vol. 95, no. 5, p. 052 106, Aug. 2009.

[118] I. Repins, M. Contreras, Y. Romero, Y. Yan, W. Metzger, J. Li, S. Johnston, B. Egaas, C. DeHart, J. Scharf, B. E. McCandless, and R. Noufi, "Characterization of 19.9%- efficienct CIGS absorbers," *Proc. IEEE 33th Photovolt. Specialist Conf.*, 2008, pp. 1-6.

[119] B. O'Regan and M. Grätzel. "A low-cost, high-efficiency solar cell based on dye-sensitized colloidal TiO_2 films," *Nature*, vol. 353, no. 6346, pp. 737-740, Oct. 1991.

[120] U. Bach, D. Lupo, P. Comte, J. E. Moser, F. Weissörtel, J. Salbeck, H. Spreitzer, and M. Grätzel, "Solid-state dye-sensitized mesoporous TiO_2 solar cells with high photon-to-electron conversion efficiencies," *Nature*, vol. 395, no. 6702, pp. 583-585, Oct. 1998.

[121] M. Grätzel, "Perspectives for dye-sensitized nanocrystalline solar cells," *Prog. Photovol. : Res. Appl.*, vol. 8, no. 8, pp. 171-185, Jan.-Feb. 2000.

[122] K. -M. Lee, C. -Y. Hsu, W. -H. Chiu, M. -C. Tsui, Y. -L. Tung, S. -Y. Tsai, and K. -C. Ho, "Dye-sensitized solar cells with a micro-porous TiO_2 electrode and gel polymer electrolytes prepared by in situ cross-link reaction," *Sol. Energy Mater. Sol. Cells*, vol. 93, no. 11, pp. 2003-2007, Nov 2009.

[123] G. Yu, J. Gao, J. C. Hummelen, F. Wudl, and A. J. Heeger, "Polymer photovoltaic cells: enhanced efficiencies via a network of internal donor-acceptor heterojunctions," *Science*, vol. 270, no. 5243, pp. 1789-1791, Dec. 1995.

[124] M. Granström, K. Petritsch, A. C. Arias, A. Lux, M. R. Andersson, and R. H. Friend, "Laminated fabrication of polymeric photovoltaic diodes," *Nature*, vol. 395, no. 6699, pp.257-260, Sept. 1998.

[125] C, J. Brabec, "Organic photovoltaics: technology and market," *Sol. Energy Mater. Sol. Cells*, vol. 83, no. 2-3, pp. 273-292, Jun. 2004.

[126] S. R. Forrest, "The limits to organic photovoltaic cell efficiency," *MRS Bulletin*, vol. 30, no. 1, pp. 28-32, Jan. 2005.

[127] J. Huang, G. Li, and Y. Yang, "Influence of composition and heat-treatment on the charge transport properties of poly(3-hexylthiophene) and [6,6]-phenyl C_{61}-butyric acid methyl ester blends," *Appl. Phys. Lett.*, vol. 87, no. 11, p. 112 105, Sept. 2005.

[128] G. Conibeer, M. Green, E. -C. Cho, D. König, Y. -H. Cho, T. Fangsuwannarak, G. Scardera, E. Pink, Y. Huang, T. Puzzer, S. Huang, D. Song, C. Flynn, S. Park, X. Hao, and D. Mansfield, "Silicon quantum dot nanostructures for tandem photovoltaic cells," *Thin Solid Films*, vol. 516, no. 20, pp. 6748-6756, Aug. 2008.

[129] P. Würfel, A. S. Brown, T. E. Humphrey, and M. A. Green, "Particle conservation in the hot-carrier solar cell," *Prog. Photovol. : Res. Appl.*, vol. 13, no. 2, pp. 277-285, Jun. 2005.

[130] A. Martí, G. L. Araújo, "Limiting efficiencies for photovoltaic energy conversion in multigap systems," *Sol. Energy Mater. Sol. Cells*, vol. 43, no. 2, pp. 203-222, Sept. 1996.

[131] A. Luque, A. Martí, and A. J. Nozik "Solar cells based on quantum dots: multiple exciton generation and intermediate bands," *MRS Bulletin*, vol. 32, no. 3, pp.

236-241, Mar. 2007.

[132] M. A. Green, "Third generation photovoltaics: ultra-high conversion efficiency at low cost," *Prog. Photovol. : Res. Appl.*, vol. 9, no. 2, pp. 123-135, Mar.-Apr. 2001.

[133] W. Shockley and H. J. Queisser, "Detailed balance limit of efficiency of p-n junction solar cells," *J. Appl. Phys.*, vol. 32, no. 3, pp. 510-519, Mar. 1961.

[134] S. Hirono, S. Umemura, M. Tomita, and R. Kaneko "Superhard conductive carbon nanocrystallite films," *Appl. Phys. Lett.*, vol. 80 , no. 3, pp .425-427, Jan 2002.

[135] G. -R. Lin, C. -J. Lin, and C. -K. Lin, "Enhanced Fowler-Nordheim tunneling effect in nanocrystallite Si based LED with interfacial Si nano-pyramids," *Opt. Express*, vol. 15, no. 5, pp. 2555-2563, Mar. 2007.

[136] F. Fuchs, U. Weimer, W. Pletschen, J. Schmitz, E. Ahlswede, M. Walther, J. Wagner, and P. Koidl, "High performance InAs/$Ga_{1-x}In_xSb$ superlattice infrared photodiodes," *Appl. Phys. Lett.*, vol. 71, no. 22, pp. 3251-3253, Dec. 1997.

[137] M. Zacharias, J. Heitmann, R. Scholz, U. Kahler, M. Schmidt, and J. Bläsing, "Size-controlled highly luminescent silicon nanocrystals: A SiO/SiO_2 superlattice approach," *Appl. Phys. Lett.*, vol. 80 , no. 4, pp . 661-663, Jan 2002.

[138] C. J. Kim and Y. K. Lee, "Characteristics of nano-thickness lead zirconate titanate thin film for high-density storage applications," *Mater. Sci. Eng. B*, vol. 122, no. 1, pp. 12-19, Aug. 2005.

[139] S. Palzer, E. Moretton, F. H. Ramirez, A. Romano-Rodriguez, and J. Wöllenstein, "Nano- and microsized metal oxide thin film gas sensors," *Microsyst. Technol.*, vol. 14, no. 4-5, pp. 645-651, Apr. 2008.

[140] S. -K. Sung, I. -H. Park, C. J. Lee, Y. K. Lee, J. D. Lee, B. -G. Park, S. D. Chae, and C. W. Kim, "Fabrication and program/erase characteristics of 30-nm SONOS nonvolatile memory devices," *IEEE Trans. Nanotech.*, vol. 2, no. 4, pp. 258-264, Dec. 2003.

[141] K. Yamamoto, H. Ito, and S. Kujime, "Nano-multilayered CrN/BCN coating for anti-wear and low friction applications," *Surf. Coat. Tech.*, vol. 201, no. 9-11, pp. 5244-5248, Feb. 2007.

[142] M. N. Baibich, J. M. Broto, A. Fert, F. N. van Dau, F. Petroff, P. Etienne, G. Creuzet, A. Friederich, and J. Chazelas, "Giant magnetoresistance of (001)Fe/(001)Cr magnetic superlattices," *Phys. Rev. Lett.*, vol. 61, no. 21, pp. 2472-2475, Nov. 1988.

[143] A. B. Pakhomov, X. Yan, and B. Zhao, "Giant hall effect in percolating ferromagnetic granular metal-insulator films," *Appl. Phys. Lett.*, vol. 67, no. 23, pp. 3497-3499, Dec. 1995.

[144] E. Kapetanakis, P. Normand, D. Tsoukalas, K. Beltsios, J. Stoemenos, S. Zhang, and J. van den Berg, "Charge storage and interface states effects in Si-nanocrystal

memory obtained using low-energy Si^+ implantation and annealing," *Appl. Phys. Lett.*, vol. 77, no. 21, pp. 3450-3452, Nov. 2000.

[145] Y. T. Hou, M. F. Li, Y. Jin, and W. H Lai, "Direct tunneling hole currents through ultrathin gate oxides in metal-oxide-semiconductor devices," *J. Appl. Phys.*, vol. 91, no. 1, pp. 258-264, Jan 2002.

[146] A. T. Tilke, F. C. Simmel, R. H. Blick, H. Lorenz, and J. P. Kotthaus, "Coulomb blockade in silicon nanostructures," *Prog, Quan. Electron.*, vol. 25, no. 3, pp. 97-138, May 2001.

[147] R. Nuryadi, H. Ikeda, Y. Ishikawa, and M. Tabe, "Ambipolar Coulomb blockade characteristics in a two-dimensional Si multidot device," *IEEE Trans. Nanotech.*, vol. 2, no. 4, pp. 231-235, Dec. 2003.

[148] H. Han, Y. Fang, Z. Li, and H. Xu, "Tunable surface plasma resonance frequency in Ag core/Au shell nanoparticles system prepared by laser ablation," *Appl. Phys. Lett.*, vol. 92, no. 2, p. 023 116, Jan. 2008.

[149] P. Ferguson, R. F. Wallis, M. Belakhovskyc, J. P. Jadota, and J. Tomkinsond, "Surface plasma waves in silver and gold," *Surf. Sci.*, vol. 76, no. 2, pp. 483-498, Sept. 1978.

[150] D. Barba, F. Martin, C. Dahmoune, and G. G. Ross, "Effects of oxide layer thickness on Si-nanocrystal photoluminescence intensity in Si^+-implanted SiO_2/Si systems," *Appl. Phys. Lett.*, vol. 89, no. 3, p. 034 107, Jul. 2006.

[151] D. R. Lillington and W. G. Townsend, "Effects of interfacial oxide layers on the performance of silicon Schottky-barrier solar cells," *Appl. Phys. Lett.*, vol. 28, no. 2, pp. 97-98, Jan. 1976.

[152] D. L. Pulfrey, "A minority carrier MIS solar cell," *Solid State Electron.*, vol. 20, no. 5, pp. 455-457, May 1977.

[153] R. B. Godfrey and M. A. Green, "655 mV open-circuit voltage, 17.6% efficient silicon MIS solar cells," *Appl. Phys. Lett.*, vol. 34, no. 11, pp. 790-793, Jun. 1979.

[154] R. E. Thomas, R. B. North, and C. E. Norman, "Low-cost high-efficiency MIS/inversion layer solar cells," *IEEE Electron Device Lett.*, vol. EDL-1, no. 5, pp. 79-80, May 1980.

[155] R. Hezel and R. Schörner, "Plasma Si nitride-A promising dielectric to achieve high-quality silicon MIS/IL solar cells," *J. Appl. Phys.*, vol. 52, no. 4, pp. 3076-3079, Apr. 1981.

[156] W. A. Anderson, G. Rajeswaran, V. J. Rao, and M. Thayer, "Cr-MIS solar cells using thin epitaxial silicon grown on poly-silicon substrates," *IEEE Electron Device Lett.*, vol. EDL-2, no. 10, pp. 271-274, Oct. 1981.

[157] M. Grauvogl, A. G. Aberle, and R. Hezel, "17.1% efficient metal-insulator-semi-conductor inversion layer silicon solar cells using truncated pyramids," *Appl. Phys.*

Lett., vol. 69, no. 10, pp. 1462-1464, Sep. 1996.

[158] A. H. M. Kipperman and M. H. Omar, "Improved efficiency of MIS silicon solar cells by HF treatment of the oxide layer," *Appl. Phys. Lett.*, vol. 28, no. 10, pp. 620-621, May 1976.

[159] J. P. Ponpon and P. Siffert, "Open-circuit voltage of MIS silicon solar cells," *J. Appl. Phys.*, vol. 47, no. 7, pp. 3248-3251, Jul. 1976.

[160] C. -Y. Wang and J. -G. Hwu, "Metal-oxide-semiconductor structure solar cell prepared by low-temperature (< 400 ◦C) anodization technique," *J. Electrochem. Soc.*, vol. 156, no. 3, pp. H181-H183, Jan. 2009.

[161] H. Ma, H. -L. Yip, F. Huang, and A. K. -Y. Jen, "Interface engineering for organic electronics," *Adv. Func. Mater.*, vol. 20, no. 9, pp. 1371-1388, Apr. 2010.

[162] T. Kondo, S. M. Lee, M. Malicki, B. Domercq, S. R. Marder, and B. Kippelen, "A nonvolatile organic memory device using ITO surfaces modified by Ag-nanodots," *Adv. Func. Mater.*, vol. 18, no. 7, pp. 1112-1118, Apr. 2008.

[163] B. -O. Cho, T. Yasue, H. Yoon, M. -S. Lee, I. -S. Yeo, U. I. Chung, J. -T. Moon, and B. -I. Ryu, "Thermally robust multi-layer non-volatile polymer resistive memory," *Dig. Int. Electron Device Meet., 2006*, pp.781-784.

[164] K. S. Yook, J. Y. Lee, S. H. Kim, and J. Jang. "Transparent organic bistable memory device with pure organic active material and Al/indium tin oxide electrode," *Appl. Phys. Lett.*, vol. 92, no. 22, p. 223 305, Jun. 2008.

[165] F. Verbakel, S. C. J. Meskers, R. A. J. Janssen, H. L. Gomes, M. Cölle, M. Büchel, and D. M. de Leeuw, "Reproducible resistive switching in nonvolatile organic memories," *Appl. Phys. Lett.*, vol. 91, no. 19, p. 192 103, Nov. 2007.

[166] B. Cho, S. Song, Y. Ji, and T. Lee, "Electrical characterization of organic resistive memory with interfacial oxide layers formed by O_2 plasma treatment," *Appl. Phys. Lett.*, vol. 97, no. 6, p. 063 305, Aug. 2007.

[167] M. G. Mason, C. W. Tang, L. -S. Hung, P. Raychaudhuri, J. Madathil, D. J. Giesen, L. Yan, Q. T. Le, Y. Gao, S. -T. Lee, L. S. Liao, L. F. Cheng, W. R. Salaneck, D. A. dos Santos, and J. L. Brédas, "Interfacial chemistry of Alq_3 and LiF with reactive metals," *J. Appl. Phys.*, vol. 89, no. 5, pp. 2756-2765, Mar. 2001.

[168] L. F. Cheng, L. S. Liao, W. Y. Lai, X. H. Sun, N. B. Wong, C. S. Lee, and S. T. Lee, "Effect of deposition rate on the morphology, chemistry and electroluminescence of tris-(8-hydroxyqiunoline) aluminum films," *Chem. Phys. Lett.*, vol. 319 , no. 3-4, pp. 418-422, Mar. 2000.

[169] C. B. Lee, A. Uddin, X. Hu, and T. G. Anderson, "Study of Alq_3 thermal evaporation rate effects on the OLED," *Mater. Sci. Eng. B*, vol. 112, no. 1, pp. 14-18, Sept. 2004.

[170] R. Treusch, F. J. Himpsel, S. Kakar, L. J. Terminello, C. Heske, T. van Buuren, V. V.

Dinh, H. W. Lee, K. Pakbaz, G. Fox, and I. Jiménez, "X-ray photoemission and photoabsorption of organic electroluminescent materials," *J. Appl. Phys.*, vol. 86, no. 1, pp. 88-93, Jul. 1999.

[171] S. M. Sze, Physics of Semiconductor Devices, second ed., Wiley, New York, 1981. Chapter 7, p. 380.

[172] J. H. Jung, J. -H. Kim, T. W. Kim, M. S. Song, Y. -H. Kim, and S. Jin, "Nonvolatile organic bistable devices fabricated utilizing Cu_2O nanocrystals embedded in a polyimide layer," *Appl. Phys. Lett.*, vol. 89, no. 12, p. 122 110, Sept. 2006.

[173] S. Paul, A. Kanwal, and M. Chhowalla, "Memory effect in thin films of insulating polymer and C_{60} nanocomposites," *Nanotechnology*, vol. 17, no. 1, pp. 145-151, Jan. 2006.

[174] A. Kanwal and M. Chhowalla, "Stable, three layered organic memory devices from C_{60} molecules and insulating polymers," *Appl. Phys. Lett.*, vol. 89, no. 20, p. 203 103, Nov. 2006.

[175] C. -H. Tu, D. -L. Kwong, and Y. -S. Lai, "Negative differential resistance and electrical bistability in nanocrystal organic memory devices," *Appl. Phys. Lett.*, vol. 89, no. 25, p. 252 107, Dec. 2006.

[176] F. Li, D. -I. Son, J. -H. Ham, B. -J. Kim, J. H. Jung, and T. W. Kim, "Memory effect of nonvolatile bistable devices based on CdSe/ZnS nanoparticles sandwiched between C_{60} layers," *Appl. Phys. Lett.*, vol. 91, no. 16, p. 162 109, Oct. 2007.

[177] S. H. Kim, K. S. Yook, J. Y. Lee, and J. Jang, "Organic light emitting bistable memory device with high on/off ratio and low driving voltage," *Appl. Phys. Lett.*, vol. 93, no. 5, p. 053 306, Aug. 2008.

[178] D. I. Son, C. H. You, W. T. Kim, J. H. Jung, and T. W. Kim, "Electrical bistabilities and memory mechanisms of organic bistable devices based on colloidal ZnO quantum dot-polymethylmethacrylate polymer nanocomposites," *Appl. Phys. Lett.*, vol. 94, no. 13, p. 132 103, Apr. 2009.

[179] G. Xie, Y. Meng, F. Wu, C. Tao, D. Zhang, M. Liu, Q. Xue, W. Chen, and Y. Zhao, "Very low turn-on voltage and high brightness tris-(8-hydroxyquinoline) aluminum-based organic light-emitting diodes with a MoO_x p-doping layer," *Appl. Phys. Lett.*, vol. 92, no. 9, p. 093 305, Mar. 2008.

[180] H. You, Y. Dai, Z. Zhang, and D. Ma, "Improved performances of organic light-emitting diodes with metal oxide as anode buffer," *J. Appl. Phys.*, vol. 101, no. 2, p. 026 105, Jan.2007.

[181] C. Tao, G. Xie, C. Liu, X. Zhang, W. Dong, F. Meng, X. Kong, L. Shen, S. Ruan, and W. Chen, "Semitransparent inverted polymer solar cells with MoO_3/Ag/MoO_3 as transparent electrode," *Appl. Phys. Lett.*, vol. 95, no. 5, p. 053 303, Aug. 2009.

[182] D. W. Zhao, X. W. Sun, C. Y. Jiang, A. K. K. Kyaw, G. Q. Lo, and D. L. Kwong, "Efficient tandem organic solar cells with an Al/MoO_3 intermediate layer," *Appl. Phys. Lett.*, vol. 93, no. 8, p. 083 305, Aug. 2008.

[183] P. -T. Lee, T. -Y. Chang, and S. -Y. Chen, "Tuning of the electrical characteristics of organic bistable devices by varying the deposition rate of Alq_3 thin film," *Org. Electron.*, vol. 9, no. 5, pp. 916-920, Oct. 2008.

[184] A. J. Nozik, "p-n photoelectrolysis cells," *Appl. Phys. Lett.*, vol. 29, no. 3, pp. 150-153, Aug. 1976.

[185] O. Khaselev and J. A. Turner, "A monolithic, photovoltaic-photoelectrochemical device for hydrogen production via water splitting," *Science*, vol. 280, no. 5362, pp. 425-427, Apr. 1998.

[186] U. S. Avachat, A. H. Jahagirdar, and N. G. Dhere, "Multiple bandgap combination of thin film photovoltaic cells and a photoanode for efficient hydrogen and oxygen generation by water splitting," *Sol. Energy Mater. Sol. Cell*, vol. 90, no. 15, pp. 2464-2470, Sep. 2006.

[187] B. Hoex, J. Schmidt, R. Bock, P. P. Altermatt, M. C. M. van de Sanden, and W. M. M. Kessels, "Excellent passivation of highly doped p-type Si surfaces by the negative-charge-dielectric Al_2O_3," *Appl. Phys. Lett.*, vol. 91, no. 11, p. 112 107, Sept. 2007.

[188] B. Vet and M. Zeman, "Relation between the open-circuit voltage and the band gap of absorber and buffer layers in a-Si:H solar cells," *Thin Solid Films*, vol. 516, no. 20, pp. 6873-6876, Aug. 2008.

[189] A. G. Aberle, "Surface passivation of crystalline silicon solar cells: a review," *Prog. Photovolt.: Res. Appl.*, vol. 8, no. 5, pp. 473-487, Sept.-Oct. 2000.

[190] H. C. Carda, "Photovoltaic properties of MIS-Schottky barriers," *Solid State Electron.*, vol. 20, no. 12, pp. 971-976, Dec. 1977.

[191] O. M. Nielsen, "On the surface recombination current of metal-insulator semiconductor inversion layer solar cells," *J. Appl. Phys.*, vol. 52, no. 9, pp. 5870-5872 , Sept. 1981.

[192] A. Hartstein and D. R. Young, "Identification of electron traps in thermal silicon dioxide films," *Appl. Phys. Lett.*, vol. 38, no. 8, pp. 631-633, Apr. 1981.

[193] Asuha, Y.-L. Liu, O. Maida, M. Takahashi, and H. Kobayashi, "Postoxidation annealing treatments to improve Si/ultrathin SiO_2 characteristics formed by nitric acid oxidation," *J. Electrochem. Soc.*, vol. 151**,** no. 12, pp. G824-G828, Oct. 2004.

[194] A. Metz, R. Meyer, B. Kuhlmann, M. Grauvogl, and R. Hezel, "18.5% efficiency first-generation MIS inversion-layer silicon solar cells," *Proc. 26th IEEE Photovoltaic Specialists Conf.*, 1997, pp.31-34.

Vita

Tzu-Yueh Chang: He received his B.S. degree in the Department of Electrical Engineering, Feng Chia University, Taichung, Taiwan in 2004. He received his M.S. degree in the Department of Photonics and Display Institute, National Chiao Tung University, Hsinchu, Taiwan in 2005. He received his Ph.D. degree in the Department of Photonics and Institute of Electro-Optical Engineering, National Chiao Tung University, Hsinchu, Taiwan in 2010. His research interests include organic resistance memory, oxide based inorganic resistance memory, $Cu(In_xGa_{1-x})Se_2$ thin film solar cells, metal-insulator-semiconductor solar cells, and silicon quantum dot thin film solar cells.

Publications

International Journals

[1] **Tzu-Yueh Chang***, Chun-Lung Chang, Hsin-Yu Lee, and Po-Tsung Lee, "A metal-insulator-semiconductor solar cell with high open-circuit voltage using a stacking structure," *IEEE Electron Device Lett.*, vol. 31, no. 12., pp. 1419-1421, Dec. 2010. (SCI IF: 2.605)

[2] **Tzu-Yueh Chang***, You-Wei Cheng, and Po-Tsung Lee, "Electrical characteristics of an organic bistable device using an Al/Alq_3/nanostructured MoO_3/Alq_3/p^+-Si structure," *Appl. Phys. Lett.*, vol. 96, no. 4, p. 043 309, Jan. 2010. (SCI IF: 3.554)

[3] Po-Tsung Lee, **Tzu-Yueh Chang***, and Szu-Yuan Chen, "Tuning of the electrical characteristics of organic bistable devices by varying the deposition rate of Alq_3 thin film," *Org. Electron.*, vol. 9, no. 5, pp. 916-920, Oct. 2008. (SCI IF: 3.262)

International Conferences

[1] **Tzu-Yueh Chang***, Chun-Lung Chang, Hsin-Yu Lee, and Po-Tsung Lee, "Characteristics of MIS solar cells using a sputtering SiO_2 insulating layer," 302-I15, *IEEE 35th PVSC*, Honolulu, Hawaii, USA (2010)

[2] You-Wei Cheng, **Tzu-Yueh Chang***, and Po-Tsung Lee, "Characteristics of organic memory using metal oxide nano-clusters," G17.3, *2010 MRS Spring Meeting*, San Francisco, California, USA (2010).

[3] Hsin-Yu Lee, Yi-Shian Max Lin, Kuang-Yang Kuo, **Tzu-Yueh Chang***, and Po-Tsung Lee, "Post-annealing temperature effect on the optical and electrical properties of the nano-structured Si/SiO_2 multilayer," Sat-P2-042, *ISSCT'08*, Taipei, Taiwan (2008)

[4] P. T. Lee, **T. Y. Chang***, and S. Y. Chen, "Investigation of electrical pulse erasing method effect on current-voltage characteristics of organic bistable device," Thu-P6-04, *IDMC'07*, Taipei, Taiwan, 2007

[5] **T. Y. Chang***, S. Y. Chen, and P. T. Lee, "Investigation of deposition rate effect on the current-voltage characteristics of organic dynamic random access bistable devices," p.19, *SID'07*, Long Bench, CA, USA (2007) (SID Travel Grant Award)

[6] S. Y. Chen, **T. Y. Chang***, and P. T. Lee, "Bistable characteristics of the organic device with heterojunction," O3.11, *MRS'07 Spring Meeting*, San Francisco (2007)

Domestic Conferences

[1] Yu-Wei Cheng, **Tzu-Yueh Chang***, and Po-Tsung Lee, "Memory characteristics of Al/AlO_x/Alq_3/n^+-Si structure," AO118, *OPT'09*, Taipei, Taiwan (2009).

[2] Kung-Yang Kuo, **Tzu-Yueh Chang***, and Po-Tsung Lee, "Study of co-sputtering Si-doped ZnO thin films," IO107, *OPT'09*, Taipei, Taiwan (2009).

[3] Yi-Heng Tsai, Yi-Shian Lin, **Tzu-Yueh Chang***, and Po-Tsung Lee, "SRO thickness dependence room temperature PL of Si NCs thin films," IO108, *OPT'09*, Taipei, Taiwan (2009).

[4] Chung-Long Chang, Hsin-Yu Lee, **Tzu-Yueh Chang***, and Po-Tsung Lee, "MIS solar cell using sputtering silicon dioxide," IO121, *OPT'09*, Taipei, Taiwan (2009).